Understanding the Ecohydrological Role of Seasonal Ground Ice in a Boreal Peatland

by

Brandon Scott Van Huizen

A thesis
presented to the University of Waterloo
in fulfillment of the
thesis requirement for the degree of
Doctor of Philosophy
in
Geography

Waterloo, Ontario, Canada, 2022

Examining Committee Membership

The following individuals served on the Examining Committee for this thesis. The decision of the Examining Committee is by majority vote.

External Examiner	Dr. Sylvain Jutras
	Full Professor, Université Laval
Supervisor	Dr. Richard Petrone
	Professor, University of Waterloo
Internal Member	Dr. Jonathan Price
	Professor, University of Waterloo
Internal-external Member	Dr. William Quinton
	Professor, Wilfrid Laurier University
Other Member(s)	Dr. Johnathan Pomeroy
	Distinguished Professor, University of Saskatchewan

Author's Declaration

This thesis consists of material all of which I authored or co-authored: see Statement of Contributions included in the thesis. This is a true copy of the thesis, including any required final revisions, as accepted by my examiners.

I understand that my thesis may be made electronically available to the public.

Statement of Contributions

This thesis has been structured in accordance with the manuscript option. Chapters two, three and four have been published. Chapter five is in preparation and will be submitted for review; consequently, should the Chapter 5 manuscript be accepted for publication, it may differ from what is presented in this thesis due to comments and feedback following peer-review.

Chapter two is published as:

Van Huizen, B., Petrone, R. M., Price, J. S., Quinton, W. L., & Pomeroy, J. W. (2019). Seasonal Ground Ice Impacts on Spring Ecohydrological Conditions in a Western Boreal Plains Peatland. *Hydrological Processes*. https://doi.org/10.1002/hyp.13626

Brandon Van Huizen completed the study design, data analysis, generated the original ideas of the role of seasonal ground ice in the Western Boreal Plains, and wrote the first draft of the manuscript. Dr. Richard M. Petrone contributed to the study design and provided feedback on the analysis and writing of the manuscript. Dr. Jonathan S. Price, Dr. William L. Quinton, and Dr. Johnathan W. Pomeroy also provided feedback on the analysis and interpretation.

Chapter three is published as:

Van Huizen, B., & Petrone, R. M. (2020). Quantifying the spatial variability of melting seasonal ground ice and its influence on potential evapotranspiration spatial variability in a boreal peatland. *Hydrological Processes*, *34*(17), 3683–3701. https://doi.org/10.1002/hyp.13840

Brandon Van Huizen completed the study design, data analysis, generated the original ideas of how seasonal ground ice spatial variability may impact potential evapotranspiration, and wrote the first draft of the manuscript. Dr. Richard M. Petrone contributed to the study design and provided feedback on the analysis and writing of the manuscript.

Chapter four is published as:

Van Huizen, B., Sutton, O. F., Price, J. S., & Petrone, R. M. (2021). Assessing the importance of bi-directional melting when modeling boreal peatland freeze/thaw dynamics. *Journal of Hydrology*, 127236. https://doi.org/10.1016/j.jhydrol.2021.127236

Brandon Van Huizen was responsible for the study conceptualization, formal analysis, writing the original and subsequent drafts and visualization for this project. Dr. Owen F. Sutton designed the bi-directional freeze-thaw algorithm and provided feedback on the analysis and writing of the manuscript. Dr. Jonathan S. Price provided feedback and insight into the analysis and writing of the manuscript. Dr. Richard M. Petrone contributed to the study design, provided the funding, and feedback on the analysis and writing of the manuscript, and supervision of the project.

Chapter five is prepared as:

Van Huizen, B., Fang, X.., Pomeroy, J.W., & Petrone, R.M. Integrating the effects of seasonal ground ice and moss evaporation into the Cold Regions Hydrological Model.

Brandon Van Huizen performed the modelling, data analysis, and integration of each peatland process into CRHM, as well as writing the first draft. Logan Fang provided valuable assistance in the integration of peatland processes into CRHM. Dr. Johnathan Pomeroy provided valuable feedback in modelling design and feedback on the manuscript. Dr. Richard Petrone provided funding for the project and valuable feedback on analysis and the manuscript. The manuscript has not yet been submitted for review.

By signing below, I indicate that I agree with the evaluation of the roles and contributions of the various authors expressed above.

R. Petrone   J. Price   J. Pomeroy   W. Quinton   O. Sutton   X. Fang

Abstract

Seasonal Ground Ice (SGI) in peatlands forms in late fall when air temperatures begin to cool, and water in peat pores freeze. It differs from permafrost peatlands in that the SGI freezes and completely melts away every fall and subsequent winter. Despite its presence in many boreal peatlands, the ecohydrological impact it has on peatland processes has been largely understudied. Large amounts of SGI require significant energy inputs every spring to melt completely, potentially reducing available energy for evapotranspiration. This is of particular importance in the Western Boreal Plains (WBP), where precipitation is often exceeded by potential evapotranspiration annually, creating a sub-humid climate. Despite this dry climate, peatlands comprise a large proportion of the landscape. Their persistence is attributed to various negative feedbacks that help reduce water losses. The melting of SGI may be one such negative feedback. Furthermore, the presence of SGI can have a profound impact on the spring freshet, influencing the peatland's role as a source or sink of water within the landscape. Despite the potential for SGI influence on peatland ecohydrological processes, it is not well represented in SVAT models. However, properly parameterizing these effects is complicated by the apparent small scale spatial heterogeneity in SGI melting as well as the presence of bi-directional melting during the spring thaw. Finally, incorporating these processes into a model are further complicated by the poor representation of moss evaporation in such models. Therefore, the purpose of this thesis is to establish a conceptual understanding of the ecohydrological role of SGI in peatlands within the WBP and begin to incorporate some of these processes into the Cold Regions Hydrological Model (CRHM). This study took place at a Boreal fen peatland (named Pauciflora), approximately 40 km south of Fort McMurray on the Stoney Mountain complex.

The conceptual role of SGI was assessed through in-situ measurements of SGI both directly by probing with a steel rod, and by proxy via ground temperature probes, and comparing trends in SGI melting with near surface soil moisture (0-5cm), water table position, and site scale potential and actual evapotranspiration (PET & AET respectively). The findings from this study indicated that the melting of SGI can reduce available energy for evapotranspiration, lowering the maximum PET for a given set of meterological conditions, reducing PET by 10 mm over the melt period. As SGI melts, it re-releases a substantial amount of liquid water (139 mm), suggesting that as it melts, it can help contribute to their role as water sources for downstream systems, as it

forms a concrete ice layer at the surface, reducing the infiltrability of the soil. However, it was found that the melting of SGI was highly spatially variable, and to properly be represented in a model, the spatial variability of melting SGI impact on PET needed to be evaluated. This was completed by conducting extensive SGI surveys during the spring, at both small (around individual trees, <0.5 m) and large scale (5 m). The spatial variability was assessed using cluster analysis, and it was found that the spatial variability was not a function of melt rates, but rather ice thickness, which in turn was controlled by proximity to individual trees, and basin morphology. Furthermore, the spatial variability of PET was determined to be a function of net radiation, and not SGI, which helps to simplify modelling approaches. Another facet of SGI that was looked at was the importance of bi-directional melt in SGI. Using the Stefan's Equation, a bi-directional melting modelling exercise was run, and found that incorporating this process, improved model prediction and the estimation of the timing of ice-free conditions, which is important when modelling the spring freshet. In addition to this role, the potential impact of a warming climate was assessed, and found that the SGI role in peatlands may shift, as thinning layers of SGI formation, and more frequent freeze/thaw cycles, may lead to less water leaving the peatland. This has implications for downstream systems, that rely on head water catchments for water sources. Finally, evapotranspiration methods used in peatlands often assume that moisture is not a limiting factor. The final portion of this study evaluated that assumption and found that while using Priestley Taylor provided similar results to the Penman Monteith equation in calculating evapotranspiration, it required expensive onsite instrumentation to properly parameterize it to achieve such results. Conversely, the Penman-Monteith equation does not require such instrumentation, however the resistance term used in it, is difficult to parameterize for moss. A first attempt at incorporating a physical representation of moss resistance into the model was attempted. However, validation proved difficult due to a lack of conditions where moss resistance might be present at Pauciflora. The findings also indicated that there is a high degree of uncertainty around estimating moss resistance and that future work should continue to focus on its inclusion into models.

Acknowledgements

Where to begin. I truly believe that nothing is ever accomplished in isolation, and although completing my PhD feels good, and has provided me with a great sense of personal accomplishment, none of it could have been completed without the help, support, and love of so many people in my life, past and present. It truly takes a village.

First, I want to thank my supervisor Dr. Richard Petrone. I came in not knowing much about peatlands or hydrology, so thank you not only for giving me this amazing opportunity to start working in peatlands but then to jump to a PhD in it. Your steady, calm, and practical guidance has been helpful throughout my time as your student and in navigating academic and normal life. Thank you.

To my friends, thank you for all the that you have done whether you knew it or not, to keep me sane, and enjoy the roller coaster ride that is the graduate student experience. My colleagues in the Hydrometerology lab, I thank you for the time and advice you have given, and for putting up with my ramblings about ice for 5ish years. I want to thank Dylan, for roping me into biking and soccer, providing a great outlet to not think about school for a bit, and being a good friend. I look forward to the many more hills we will ride. To Owen, for your sage advice and chats over beers, rock climbing, and teams. To Omar, thank you for reminding me of the importance of taking breaks, especially if they involve coffee during the afternoon lull. To Scott Davidson, thank you for being a sounding board to talk not just about work, but all the movies that are out there. To the rest of my sky-dungeon friends; Nicole, Nataša and Tasha-Leigh, thank you for your guidance and support through all of this.

This thesis could not have been completed without the love and support of my family; specifically, my parents, Ted and Lydia Van Huizen, thank you for encouraging me to take the opportunities that come my way, and supporting me through all the ups and downs since moving to Waterloo. To my brothers, you can now call me Dr. BS, you're welcome. I love you all, and I couldn't have done any of this without you.

Thank you to my loving partner in crime, my wife, Tasha-Leigh Gauthier. My accomplishments are just as much yours as they are mine. Thank you for showing me that there is more to life than school; I look forward to the many life adventures that await us. I love you.

Dedication

To my grandparents Arelus and Gebbina Van Egmond. You are the inspiration for so many adventures and the excitement to seek the world around me. Thank you.

Table of Contents

List of Figures

xiv

List of Tables

Chapter 1 : Introduction

Peatlands are wetlands with an organic soil layer >40cm (National Wetlands Working Group, 1997), where the thick organic layers, comprised of vegetation litter from the surface, formed due to anoxic conditions and slow decomposition rates (Hayward & Clymo, 1982). Vegetation varies depending on the type of peatland, but often includes *Sphagnum* mosses, considered a primary peat forming material (Hayward & Clymo, 1982). Despite the relatively small surface area coverage, peatlands function as large carbon stores (Drever et al., 2020; Gorham, 1991), with approximately 147 Gt of soil organic carbon in Canada alone (Tarnocai, 2009), as well as storage and conveyors of water across the landscape (e.g. Quinton et al., 2003; Wells et al., 2017).

As the Canadian northern climate continues to warm (Zhang et al., 2019), peatland ecosystem function is projected to shift, as a warmer climate will likely induce drier peatland conditions (Helbig et al., 2020). Drier conditions will lead to increased carbon losses as aerobic decomposition takes over, which can be further amplified by increased vulnerability to fire (Elmes et al., 2017; Turetsky et al., 2011). This is of particular importance (Thompson et al., 2017a) in the sub-humid climate of the Western Boreal Plains (WBP), where precipitation is often exceeded by potential evapotranspiration on an annual basis (Marshall et al., 1999). The regional climate is already dry, and yet peatlands can persist despite the presence of this sub-humid climate. This persistence is attributed to various ecohydrological feedbacks (Waddington et al., 2015), which help maintain wet conditions. However, not all peatland ecohydrological processes are fully understood, or well-integrated into soil-vegetation-atmosphere transfer (SVAT) models. This has led to a renewed focus (Helbig et al., 2020; Wania et al., 2009; Wu et al., 2016), in order to better represent peatlands in models, and how they will respond to future climate warming.

While there is a solid understanding of the general hydrology (Elmes & Price, 2019; Thompson et al., 2015; Volik et al., 2020) and carbon cycle (e.g. Murray et al., 2017) of peatlands, less attention has been paid to the winter processes in peatlands, particularly the importance of freeze/thaw cycles and the freezing and melting of Seasonal Ground Ice (SGI).

In WBP peatlands where there is no permafrost, thick layers of ice can still form at or just below the peatland surface. This ice forms due to the highly porous nature of the surface moss layer (Woo & Winter, 1993), where porosities can exceed 0.9 (Petrone et al., 2008; Redding & Devito, 2005), and the relatively high water table positions during the fall and winter seasons. This means that anywhere from the top 15-90 cm (Kingsbury & Moore, 1987; Smerdon & Mendoza, 2010) of the

peatland soil largely comprise ice. This forms a relatively impermeable surface that in the following spring, can limit infiltration, directly impacting the spring freshet (Price & FitzGibbon, 1987).

Melting SGI in the spring also means there is a larger ground heat flux, representing a larger portion of the surface energy budget (Halliwell & Rouse, 1987; Lafleur et al., 2005; McKenzie et al., 2007; Woo & Xia, 1996). This large increase is due to the thermal properties of water. First, liquid water has a high heat capacity (4.180 MJ/(m^{3}C)), which means a significant amount of energy is needed to be lost/gained during the freezing/melting process. Furthermore, the latent heat of fusion, that is the energy required to melt ice, is quite high (334 000 J/kg). Having a large ground heat flux reduces the available energy at the surface for evapotranspiration. However, it is unknown what the magnitude of this impact might be. This is of particular relevance for peatlands within the WBP, where evapotranspiration is the dominant flux (Brown et al., 2014; Thompson et al., 2015) and is expected to increase as the climate warms. This may shift one of the potential negative feedbacks to peatland persistence in the WBP. However, an ecosystem's resiliency is in part a function of redundancy (Lawton & Brown, 1994), and it is unclear if the melting of SGI is one of the many negative feedbacks that peatlands have developed in the WBP to persist despite the dry climate. Furthermore, this role of SGI is likely to change as the climate continues to warm in the Canadian boreal forest (Bush & Lemmen, 2019).

While permafrost impacts on the ecohydrological characteristics of peatlands (e.g. Kujala et al., 2008) and its role in a changing climate on peatlands (e.g. Hugelius et al., 2020; Patankar et al., 2015) have been well studied, the role of SGI has received markedly less focus in the literature, despite the large proportion of peatlands that are not underlain by permafrost (Tarnocai, 2009; Wieder & Vitt, 2006), and the lack of permafrost in the WBP. As such, there is uncertainty around when the impacts of melting SGI no longer influence the infiltrability of the peatland. This is further complicated by the fact that SGI melts from both above and below (Woo et al., 2004), and in spatially heterogenous patterns, leading to temporal variability in the timing of ice-free conditions.

The use of ecohydrological models, can help explore the importance of SGI to peatland ecosystem function, however the uncertainties around SGI impact on the spring freshet, available energy, and whether its spatial and temporal variability matter on an annual basis complicates any modelling effort for peatlands that experience seasonal freeze/thaw. SVAT models are often used in

hydrological studies as they are useful for understanding processes within a system. The Cold Regions Hydrological Model (CRHM) (Pomeroy et al., 2007) is one such example that incorporates the various cold region processes experienced in Canada. However, the treatment of freeze/thaw is often relegated to approaches for permafrost environments (Krogh et al., 2017; Stone et al., 2019), and wetlands are often treated as functionally the same despite their variability in type, vegetation, and ecohydrological state (Zoltai & Vitt, 1995), nor do they incorporate the energy impacts of the freezing/thawing of SGI in a peatland.

In addition to the complexities of modelling freeze/thaw, peatland evapotranspiration is a key hydrological component of these models. However, accurately modelling peatland ET is complicated by the uncertainties around Potential (PET) and Actual ET (AET). Peatlands are often assumed to evaporate at potential rates, meaning water is not limited. However, peatland AET in the WBP has been shown to often fall below PET (Volik et al., 2020), necessitating the parameterization of a surface resistance term. However, most resistance schemes are based on vascular plants, which moss, often the dominant vegetation coverage in peatlands, is not. Along with not accounting for the energy impacts of melting SGI on peatland AET, current resistance schemes in SVAT models are not suitable then for modelling peatland evapotranspiration. These uncertainties pose a further challenge if the modelling of reclaimed sites is needed.

1.2 Objectives

Therefore, given the uncertainties around the role of SGI in boreal peatlands, and subsequently how to model its freeze/thaw, and its impacts on peatland evapotranspiration, the research goal of this thesis is to determine the ecohydrological role of SGI in boreal peatlands, to better incorporate peatland processes into hydrological modelling. Achieving this research goal will provide a better understanding of cold regions processes in peatlands, that can be used to inform our understanding of both natural and constructed peatland systems. The specific objectives for this goal build upon each other starting with the conceptualization of the role of SGI in peatlands, moving through how to model it, and ultimately assessing the performance of modelling the freeze/thaw of a boreal peatland and its impacts on evapotranspiration. The objectives are as follows;

1. Conceptualize the ecohydrological role of Seasonal Ground Ice in a boreal peatland
2. Quantify the importance of Seasonal Ground Ice spatial heterogeneity on peatland evapotranspiration

3. Quantify the importance of bi-directional melting of Seasonal Ground Ice to the spring peatland ecohydrological conditions, and how it may change under a changing climate

4. Incorporate peatland freeze/thaw processes and moss resistance into CRHM, to better represent peatland ecohydrological processes in CRHM.

1.3 Organization of thesis

This thesis is divided into seven chapters which conform to the manuscript option at the University of Waterloo. Chapter 1 introduces the research topic, the context for the research goal, and four objectives listed in section 1.1. Each objective is addressed individually by chapters 2-5.

Chapter 2 provides a conceptualization of the role of seasonal ground ice in boreal peatlands, investigating the trends of ice thickness and ice melt rate and how they relate to soil moisture, water table position, and microtopography. It also provides an analysis into the available energy reduction effect of melting ice. Chapter 3 builds on the initial findings of Chapter 2, and investigates the spatial controls on SGI melt patterns, and whether spatial variability in melting ice matters for estimating site scale evapotranspiration. Chapter 4 assesses the importance of including bi-directional melting in ecohydrological models estimating the timing of ice-free conditions in a peatland, and the sensitivity to peatland freeze/thaw cycles to climate change. Chapter 5 incorporates the various impacts of SGI on boreal peatlands into the Cold Regions Hydrological Model, to test the impact of SGI available energy reduction on actual evapotranspiration and improve model evapotranspiration estimates for a boreal peatland. Finally, Chapter 6 provides a conclusion to the thesis, assessing the impact of the findings for boreal peatlands, and discusses subsequent research that is needed.

Chapter 2 : Seasonal ground ice impacts on spring ecohydrological conditions in a Western Boreal Plains peatland

2.1 Introduction

Peatlands are ubiquitous in the Western Boreal Plain (WBP) (Petrone et al., 2007), persisting in the landscape despite the presence of a subhumid climate where annual potential evapotranspiration (PET) often exceeds annual precipitation (Devito et al., 2005; Marshall et al., 1999). Peatlands in the WBP serve as important carbon storage features (Gorham, 1991; Kleinen et al., 2012) and water sources for ecosystems within this landscape (Thompson et al., 2015). Peatland persistence can be attributed to the dynamic nature of their physical properties (Waddington et al., 2015; Whittington & Price, 2006), which keep the peatland surface in close proximity to the water table maintaining the wet conditions required for peat accumulation. However, during the spring (e.g., March-June), water losses from peatlands can be enhanced by the presence of thick seasonal ground ice (SGI) due to a reduction in storage capacity, which increases surface run-off (Price & FitzGibbon, 1987; Woo & Winter, 1993). SGI can also persist well into the growing season (Brown et al., 2010; Goodbrand et al., 2018; Petrone et al., 2008; Thompson & Waddington, 2013), which extends its potential ecohydrological impacts.

SGI differs from permafrost because it melts within a year of its formation, generally occurring soon after ground surface temperatures are ≤0°C. The warmer peatland surface underlying cooler air creates a temperature gradient resulting in a transfer of energy from the ground via conduction (Hayashi et al., 2007)and radiation (Hayashi, 2013; Oke, 1987), leading to the freezing of water within the peat pore spaces.

SGI represents a frozen soil state (van Everdingen, 1975) and exists in two forms: reticulate and concrete (Woo & Winter, 1993). Reticulate SGI forms in the unsaturated zone, from water present at the time of freezing or from moisture migration to the freezing front (Lunardini, 1981). Concrete SGI in peatlands forms at the interface of the unsaturated zone and the water table and freezes downwards into the saturated zone increasing the SGI thickness. The initial thickness of the ice is controlled both by the air temperature and the presence of a snowpack. As the snowpack develops, freezing slows down and stops (Moore, 1987) due to the insulative properties of the snowpack. SGI thickness can also increase from above during periodic melt events. When an overlying snowpack begins to melt, snowmelt reaches the base of the snowpack and can refreeze

upon contact with the frozen ground surface (Granger et al., 1984; Nagare et al., 2012; Redding & Devito, 2011). SGI reduces peatland infiltrability due to ice filled pore spaces.

Reticulate ice in the unsaturated zone only has a minor impact during the spring due to the presence of air in larger pore spaces (Price, 1987; Smerdon & Mendoza, 2010). The greater impact on peatland infiltrability and storage capacity is the position of the concrete SGI relative to the peatland surface, which can vary with micro- topography. When concrete SGI forms close to the ground surface, it reduces the spring snowmelt infiltration rate (Hayashi, 2013), creating a transient perched water table and surface ponding. The impervious nature of concrete SGI is due to the large storage capacity of peat in the near surface layers. Total porosity in the top 20 cm for peatlands in the WBP can range from 0.94 to 0.98 (Redding & Devito, 2005), which means the water content in the near surface peat can range from 94% to 98%. Thus, when concrete SGI forms in peatlands, it is predominantly ice, with little peat material, resulting in a soil layer that is effectively impervious to large amounts of infiltration.

By restricting the infiltration of snowmelt water, concrete SGI increases snowmelt run-off (Price & FitzGibbon, 1987; Price, 1987), an important recharge source in the WBP landscape (Smerdon et al., 2008). Therefore, SGI can promote a peatlands ability to act as a source of water within the WBP landscape. The resulting increase in ponded water and surface saturation also allows for actual evapotranspiration (AET) near PET rates, even during the lower available energy conditions of the spring period (Brown et al., 2010; Petrone et al., 2008). However, snowmelt run-off and evaporated water reduce the amount of water entering peatland storage, increasing the reliance on precipitation and groundwater inputs for peatlands to maintain an adequate moisture supply during the snow free period. Melt water released from melting SGI is not an additional water input into the peatland, because it is a function of the antecedent moisture conditions prior to freezing. However, where this freezing occurs during winter may help keep water closer to the surface for the following spring. During the spring, *Sphagnum* mosses, the dominant peat forming vegetation (Hayward & Clymo, 1982) for bogs and poor fens, are typically close to their optimal moisture content (Moore et al., 2006). Consequently, the absence of SGI in the spring, when combined with a thin snowpack or minimal precipitation, may reduce the resiliency of surface vegetation to moisture stress.

Snowmelt run-off and AET water losses are in part due to the physical presence of SGI. However, the presence of melting SGI means more energy is driving phase change compared with

temperature change. When including this phase change in the ground heat flux (Q_G) calculation, it increases Q_G, which can reduce available energy for evapotranspiration. The Q_G can be partitioned (Rouse, 1984) into a sensible (QG_S) and a latent (QG_L) heat flux. For SGI to melt, a substantial amount of energy is required to drive the phase change due to the high latent heat of fusion of ice (334J/g; Farouki, 1981). This increases the QG_L component of Q_G, increasing the total Q_G (Runkle et al., 2014; Woo & Xia, 1996), which reduces available energy at the surface for evapotranspiration (Lafleur et al., 1997; Rouse, 2000). Despite high moisture conditions supplied by snow and SGI melt near the sur- face promoting conditions where AET is close to PET (Petrone et al., 2008), SGI also has the potential to reduce peatland water losses during the spring. Whether SGI enhances or reduces water losses from the peatland surface is dependent on available moisture and energy during melt, which is controlled by the melt rate.

When SGI is at or close to the peatland surface, melt rates of SGI depend on the energy transfer across the peatland surface, which is controlled by the peat thermal characteristics. A higher proportion of air relative to liquid water in the soil (e.g., hummocks) results in a lower thermal conductivity, and the SGI melt rates may be slower (Kingsbury & Moore, 1987). A higher proportion of liquid water relative to air (e.g., hollows) means melt rates can increase due to the higher thermal conductivity of water (McClymont et al., 2013). Therefore, peatland microtopography may influence SGI melt rates and subsequently horizontal and vertical water losses. Yet the influence of microtopography on SGI melt and whether SGI melt significantly increases or decreases evapotranspiration has not been studied. The role of SGI on hydrological processes in WBP peatlands, particularly during the spring (March to June) when it can have the most pronounced impact peatland hydrological function, is largely unknown.

WBP peatlands are under pressure from resource extraction in the Athabasaca Oil Sands Region, where they are removed during sur- face mining processes or impacted during other development activities (Rooney et al., 2012), and from climate change (Ireson et al., 2015; Waddington et al., 2015), both of which can alter or remove peatlands, removing a water source from the landscape. Climate change predictions for the WBP suggest warmer air temperatures particularly in the winter months (Jiang et al., 2017) and an increase in the length of the snow-free season (Vaughan et al., 2013). Precipitation is projected to increase (Mbogga et al., 2010; Wang et al., 2014); however, there is uncertainty if this is enough to offset higher evaporative losses (Ireson et al., 2015; Thompson et al., 2017). Thus, understanding the potential impacts of SGI on

the ecohydrology of peatlands in the WBP and Athabasaca Oil Sands Region is important for reclamation work and to understand how these systems may respond to climatic change.

Therefore, the goal of this paper is to evaluate the potential role of concrete SGI (herein referred to as SGI) during the spring melt in a WBP peatland, determining whether the net effect is to enhance or diminish water losses via evapotranspiration. The objectives are to (a) quantify SGI characteristics during the melt period and determine the influence of microtopography on ice structure and melt rate; and (b) determine the relationship between SGI and hydrological processes (i.e., water table depth, soil moisture, PET, and AET) to better under- stand the SGI role in WBP peatland ecohydrology.

2.2 Study Area and Methods

2.2.1 Study Area

A field study was completed from April 7 to June 26, 2017, at Pauciflora Fen, a poor fen (56°22'30.36"N, 111°14'3.29"W) approximately 40 km south of Fort McMurray, Alberta (Figure 2-1a,b). Pauciflora Fen is located on the Stoney Mountain complex within the WBP, where a subhumid climate is present. The 30-year climate normal for the area shows a mean annual temperature of 1.1°C and a mean rainfall of 307mm (Fort McMurray Airport, Environment Canada), whereas mean snow water equivalent (SWE) is approximately 104 mm, calculated from an empirical relationship between air temperature and snow density (Hedstrom & Pomeroy, 1998). However, Pauciflora has a wetter climate compared with typical peatlands in the WBP due to its higher elevation in the Stoney Mountains, with a 6-month growing season (April to September) mean over 4 years (2011–2014) precipitation of 412 mm due to orographic precipitation (Wells et al., 2017) approximately 100mm higher compared with the 30-year climate normal. The 4-year mean exceeds the mean PET (369mm) during the growing season, indicating that Pauciflora may not be subject to the same subhumid climate as frequently as other peatlands in the surrounding area.

The fen has an area of 0.11 km^2 and is bounded by a road to the north, where a culvert (Figure 1c) acts as an outlet, and by forested hillslopes surrounding the rest of the fen. Field data were collected in a sparsely treed area of the fen (peat thicknesses ≈ 4m) corresponding with the "neck," part of the North Fen in Wells et al., (2017). The entire fen is underlain primarily by fine-grained silt with a high clay fraction (Wells et al., 2017). Trees were composed of Picea mariana and Larix laricina (Figure 2-1d,e), located between two hillslopes on the east and west sides of the

fen. Understory vegetation is com- posed of a carpet of Sphagnum moss. A detailed description of the fen vegetation can be found in Bocking et al., (2017) and the hydrogeological setting in Wells et al., (2017).
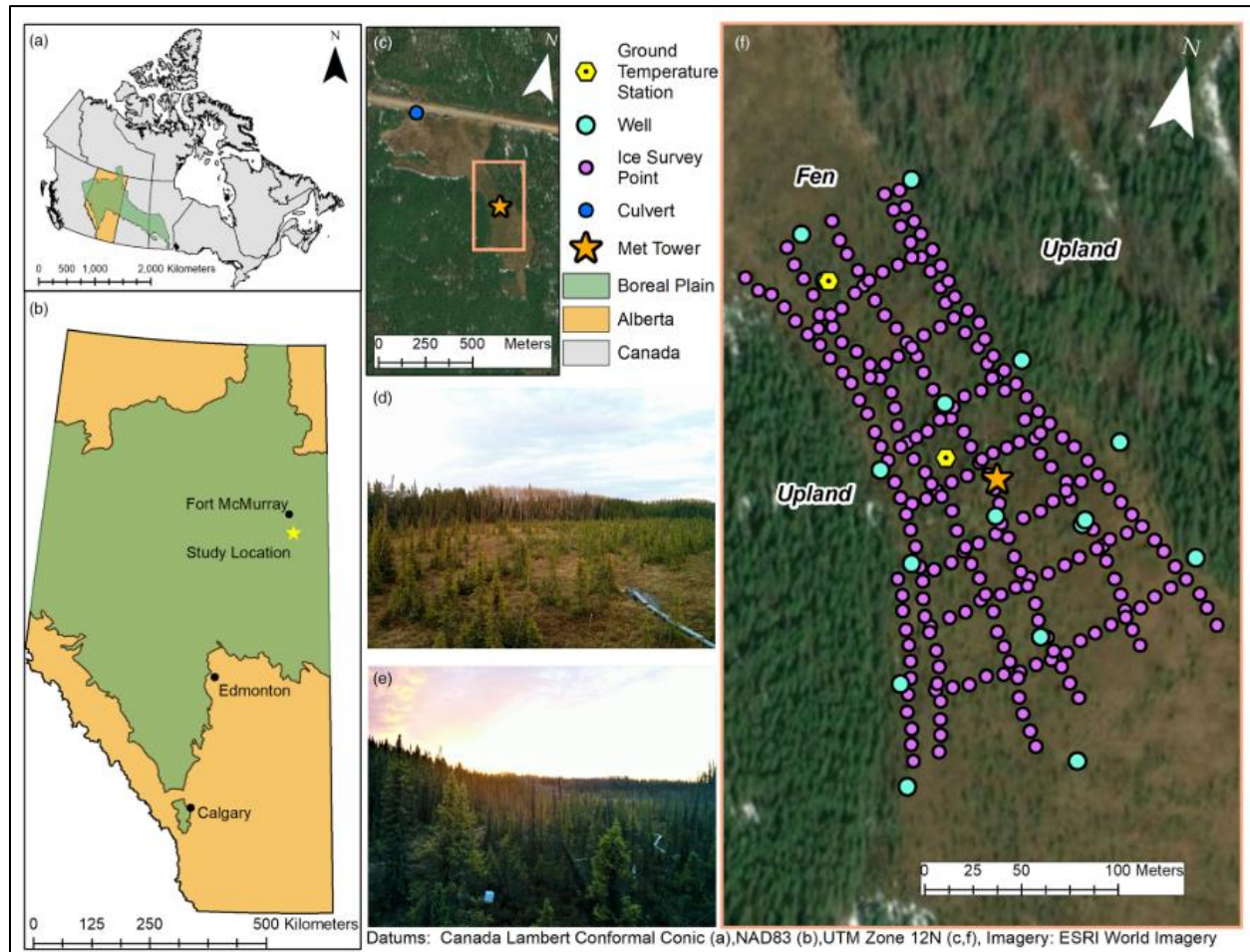
Figure 2-1a) The location of Alberta within Canada. (b) The location of Pauciflora within Alberta and the Boreal Plain. (c) The location of the culvert (outflow) relative to the survey area (d) looking south from the met tower showing the canopy characteristics of the site, (e) looking north showing the proximity of the west hillslope and the mid fen temperature ground station (white box near the bottom of the image). (f) Map shows the study area within Pauciflora Fen including the well.

2.2.2 Micrometerological variables

Air temperature (°C), relative humidity (%), windspeed (m/s), and net radiation (W/m2) were measured at a 60-s interval using a CR1000 data logger (Campbell Scientific Ltd., Logan, Utah) and averaged at 30-min intervals. Air temperature and relative humidity were measured 2m above the surface (HMP35C, Vaisala, Helsinki, Finland). Wind speed and direction (RMYoung 05103, Campbell Scientific, Logan, Utah) and net radiation (CNR4 Net Radiometers, Kipp & Zonen, Delft, Netherlands) were measured at 6m. Precipitation was measured on site,

approximately 200m north of the met station using a tipping bucket rain gauge (HOBO Onset, Hoskins Scientific, Burlington, Canada) connected to a CR1000 Campbell Scientific datalogger.

AET was measured continuously and recorded at half hour intervals, 4 m above the ground surface using an eddy covariance (EC) system, and summed to daily values, following similar approaches used in boreal peatlands (S. M. Brown et al., 2010; Warren et al., 2018; C. Wells et al., 2017). The EC system consisted of a 3D sonic anemometer (Gill Windmaster Pro, Gill Instruments, Lymington, UK) and a closed-path infrared gas (CO_2/H_2O) analyser (LI-7200, LICOR Inc., Lincoln, Nebraska) sampled at 20Hz. EC data were processed in EddyPro software (LI-COR Inc., Lincoln, Nebraska, USA), in which corrections were made for time lag and sensor separation (Song-Miao Fan et al., 1990), coordinate rotation (Kaimal & Finnigan, 1994), periods of low turbulence and energy balance closure (Petrone et al., 2015), and density effects (Burba et al., 2012). A footprint analysis (Kljun et al., 2004) was completed in order to remove any fluxes from the flux total that were found to originate outside of the fen. The mean flux footprint (2014–2018) area was 0.0032 km^2, extending ≈ 41 m north, ≈ 37 m south, ≈ 26 m west, and ≈ 22 m east from the EC system.

2.2.3 Ice and snow surveys

Ice surveys were conducted on April 8, 10, and 13, May 3, 9, 16, 23, and 30, and June 6, 2017, nine in total. The spatial extent, and depth to SGI, was determined using 13 transects with survey points spaced 5m apart within each transect (Figure 1f). Four measurements of depth to SGI were taken within 1m of the survey point by inserting a graduated steel rod into the peat until resistance was met. This method has been reported to have an error up to 4 cm in fen peatlands (Woo & Xia, 1996) due to peat compaction from the sampler's weight but was deemed acceptable because it allowed for broad spatial measurements. At every second survey point, volumetric moisture content (VMC) in the near surface (0- to 5-cm layer) was measured in triplicate and averaged, using a WET-2 soil water sensor (Delta-T Devices, Cambridge, UK), using organic soil parameters as defined by the moisture metre. The 0- to 5-cm layer coincides with the living *Sphagnum* moss layer in the peat profile and contains the capitulum, the site of photosynthesis in *Sphagnum* mosses (Schipperges & Rydin, 1998). Low VMC in the 0- to 5-cm layer can be an indicator of moisture stress for the mosses.

Two hundred forty survey points were measured and classified based on observation of microtopographical form. Hollows were localized depressions where the water table was often

10

visible, hummocks were visibly raised mounds, and lawns were within larger flat areas with no visible hummock-hollow topography. A dual-frequency sur- vey-grade differential global positioning system (Topcon GMS-2, 2011–2012; Leica Viva GS14, 2014) quantified the longitude, latitude, and absolute elevation of each survey point and well location (vertical accuracy ± 0.5 cm).

Four snow surveys were carried out on April 18, 21, 25, and 29 following snow events on April 16 and 17, prior to these dates, the site was snow free. Snow depth was measured along a transect that ran from north to south through the ice survey area using a standard Meteorological Service of Canada snow tube sampler. In order to calculate SWE, snow pits were dug near the transects to obtain representative values of snow density using standard methods (Adams & Barr, 1974). The average SWE for the ice survey area was calculated by multiplying the average density by the average depth for each snow survey.

2.2.4 Water Table Dynamics

Water table was measured manually with a blowstick using 14 monitoring wells constructed from polyvinylchloride (2.5-cm inner diameter) pipe and screened with 200 glass fibre-based well sheathing well sock (Rice Engineering, Edmonton, Alberta). Wells were installed to a depth of 1 m below the ground surface. Pre-existing wells within the fen, labelled with the prefix "T2" in Wells et al., (2017), were also used. Due to differences in sampling location of the SGI and water table depth, interpolated surfaces of the water table were created using an inverse distance weighting (IDW) method in ArcGIS 10.1 with a 1-m cell size and a fixed distance search radius of 12 m. The SGI survey was overlain onto the water table surface, and each survey point compared with the underlying water table cell value. Water table and depth to SGI were compared on May 3,9, 16, and 23 spanning the majority of the melt period. Note that for May 16 and May 23, the water table data are taken from May 17 and May 22, respectively.

2.2.5 Peat ground temperatures and impacts on available energy

Peat subsurface temperatures were recorded at two locations, the mid fen (MF) located 11m north-west of the met tower, had a more open canopy compared with the north treed fen (NTF; Figure 1d,e) located 70 m north of the met tower. For each location, two wooden stakes had eight holes drilled into it that corresponded with the measurement depths (MF: 2, 5, 10, 20, 50, 75, 100, and 150 cm; NTF: 2, 5, 10, 20, 30, 40, 50, and 60 cm). Type-T thermocouple (Omega Engineering, Norwalk, Connecticut, USA) was inserted into each so that just the exposed metal tips of the wire

were extended past the wood. Each wire was sealed using an epoxy resin. One stake was inserted into a hummock and the other into an adjacent hollow and each thermocouple wired into a Campbell Scientific logger (CR1000 Campbell Scientific Ltd., Logan, Utah). These data were used to determine temperature gradients for the 2- to 5-cm peat soil layer, where negative temperature gradients indicate that the peat surface is warmer than deeper soil layers. A temperature gradient of 0 represents isothermal conditions in the top 5cm of the peat soil.

The relationship between the spring ground heat flux (Q_G), SGI, and PET was assessed for each spring from 2013 to 2018. Calorimetric Q_G was calculated using the full temperature profile from the MF ground temperature station following the approach of Halliwell & Rouse, (1987). Calorimetric Q_G was used in the Penman-Monteith equation (Monteith, 1965) to calculate three daily PET rates for the duration of each ice melt period from 2013 to 2017: (a) considering the calorimetric Q_G (PETQG$_{Cal}$), (b) ignoring Q_G (PETQG$_{none}$), and (c) assuming Q_G is equal to 10% of net radiation (PETQG$_{10}$). Only PET daily values that coincided with SGI melt were used for comparisons. PET for this study corresponds to wet-surface evapotranspiration, which considers available energy and atmospheric conditions, and as such represents an upper limit of PET (Granger, 1989). The relationship between AET and depth to SGI was evaluated by comparing AET measured by the EC system to the depth of the 0-degree isotherm (assumed to equal the depth to SGI) and the 2- to 5-cm temperature gradient measured at the MF ground temperature station. Due to a lack of data overlap between the EC system and when SGI was present at the ground temperature monitoring station, only the data from the spring of 2015 and 2018 were used. Both of these springs were warmer and had thinner SGI based off of the ground temperature profiles. As a result, the melt periods (9 days for 2015 and 3 days for 2018) were much shorter compared with the 2017 melt period (19 days).

2.2.6 Spatial Interpolation

An IDW was used to spatially interpolate each survey with a cell size of 1 m. Ice-free areas were included in the IDW process by creating Thiessen, (1911) polygons around each ice-free survey point and added as breaklines in the IDW. A summary of the survey points and cross validation results are shown in Table 2-1.

Table 2-1 Cross validation results for the inverse distance weighted interpolations for the ice and water table surveys.

Survey Date	RMSE (cm)	Mean Error (cm)	Sample Size
Ice Survey			
May 3, 2017	0.063	0.00048	240
May 9, 2017	0.079	0.0013	207
May 16, 2017	0.10	0.0014	177
May 23, 2017	0.12	0.0024	138
June 6, 2017	0.13	-0.0030	25
Water Table Survey			
May 3, 2017	4.2	0.2	11
May 9, 2017	5.9	0.26	12
May 16, 2017	3.7	0.69	12
May 23, 2017	9.3	2.8	14
June 6, 2017	11.8	4.3	15

The volume of ice that melted from above for each cell can be calculated using the following equation:

$$V_{Ice} = \left((\Delta Z_{Ice} \text{ x Surface Area}) \text{ x } \Phi \right)$$

(2-1)

where V_{Ice} is the volume of ice (m^3) for each cell, ΔZ_{Ice} is the change in ice elevation, surface area is the cell raster size (1m^2), and Φ is the total porosity. An IWE depth (mm) was calculated using

$$IWE = \left(\frac{[V_{Ice} \times VEXP_{Ice}]}{\text{Surface Area}} \right) \times 1000$$

(2-2)

where IWE is the ice water equivalent (mm) and $VExp_{Ice}$ is the volume expansion of ice (9%). To better ascertain the error associated with peat compaction, ice measurements were made with a frost probe at the MF and NTF ground temperature stations in 2018. The average difference between the measured ice and the interpolated 0-degree isotherm was −3cm (25mm in IWE) for the MF and −1.4cm (12mm in IWE) for the NTF, which is below the estimated error values due to compaction reported by Woo & Xia, (1996) and support the confidence in IWE reported below.

2.2.7 Peat hydrophysical properties

Twelve unfrozen cores approximately 40cm in length were taken from hummocks (n = 6) and hollows (n = 6). Hummock cores were taken by inserting polyvinylchloride pipe into the moss and cutting through the moss on the outside of the pipe with a hand saw. Hollow cores were taken using Wardenaar Peat profile sampler (Eijkelkamp, The Netherlands). Cores were wrapped in plastic wrap, frozen, and then transferred to the Hydrometerology Lab, University of Waterloo, where peat porosity and bulk density were determined using methods outlined by (Boelter, (1969).

2.3 Results

2.3.1 Ice melt and IWE

Pauciflora was found to be snow free on April 8, and three SGI surveys were completed on April 8, 10, and 13. SGI was <30 cm below the surface, and no significant differences (pairwise Wilcoxon test) were noted in ice depth between the three survey days (p≤ .05) indicating that minimal melting occurred over this period. Two snow events (total SWE ≈ 64 mm) on April 16 and 17 delayed any further ice surveys until snow free conditions on May 1. Six ice surveys were completed in May and June, each differing significantly from each other in depth to ice (p ≤ .01; Figure 2-2).
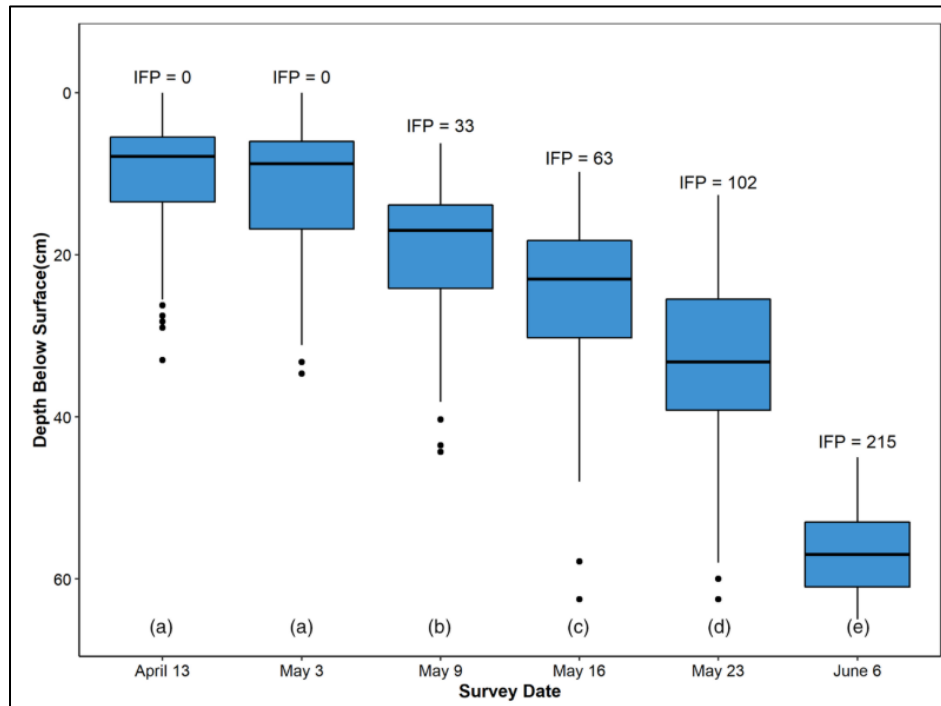
Figure 2-2 Ice depths for ice surveys completed on April 13, May 3, May 9, May 16, May 23, and June 6with the number of ice free points (IFP) for each survey. Different letters indicate statistically significant differences (pairwise Wilcox, p < .05). The ice survey on May 30 was removed due to insufficient data.

14

Results from the surveys show a gradual melt over the month of May and into the month of June. From May 3 to May 23, median depth to ice increased from 8.8 to 32.3 cm while 102 survey points became ice free over a 20-day span (Figure 2-2). From May 23 to June 6, the median depth to ice increased to 57 cm, coinciding with an additional 113 survey points becoming ice free but was over a 15-day span. By June 6, the SGI was quite deep and sporadic, and the majority of the survey area was ice free. Depth to SGI differed significantly within each microtopographic form between ice surveys, where all pvalues for each microtopographic form were <.01 (pairwise Wilcox).
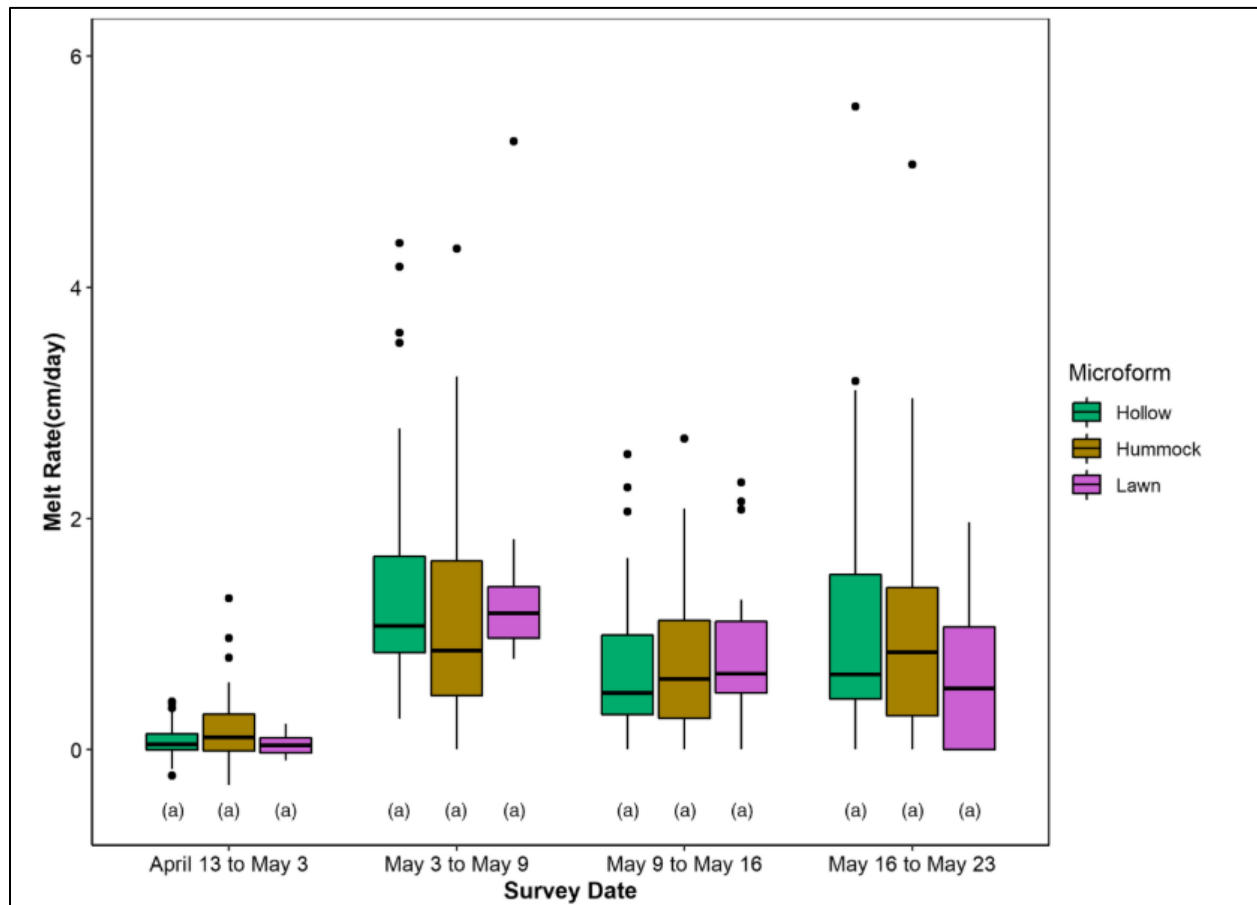
Figure 2-3 Daily average melt rate between ice survey dates, grouped by microtopography, where avg melt rate = Difference in ice depth/ number of days between surveys. Different letters indicate statistically significant differences (pairwise Wilcox, p < .05) within each group.

However, the daily average melt rate between microforms did not differ significantly during the month of May (Figure 2-3). Daily median melt rate ranged from 0.05 to 1.2 cm/day (Figure 2-3). The lowest melt rates occurred between April 13 and May 3, where the fen was covered in snow until May 1. Beginning in May, daily median melt rates were fairly consistent,

ranging from 0.5 to 1.2 cm/day. Melt rates for all micro- forms for the May 3–9 and May 16–23 ice surveys were higher compared with May 9–16 (Figure 2-3), which coincided with cooler air temperatures and a snow event on May 14. All three microforms exhibited higher melt rates earlier in the season (see May 3–9) compared with the rest of the month. Lawns initially thawed faster than hummocks and hollows. However, during the mid and late portions of the month, hummocks and lawns thawed slightly faster than hollows. The May 23 to June 6 melt rates were not included due to low sample size. The amount of water released from the top of SGI during melting (Figure 4) was calculated for each melt period using Equations (1) and (2), the SGI IDW surfaces, and an average porosity of 0.97, based on the peat core hydrophysical properties (Table 2).

Table 2-2 Average porosity and average bulk density from peat cores.

Core	Depth Interval (cm)	Porosity	Porosity Standard Deviation	Bulk Density (g/cm³)	Bulk Density Standard Deviation	No. of Samples
T2 center (hummock)	0-40	0.98	0.01	0.04	0.01	8
T2 center (hollow)	0-40	0.98	0.01	0.04	0.01	4
T2 east (hummock)	0-40	0.97	0.01	0.05	0.02	7
T2 east (hollow)	0-30	0.95	0.03	0.08	0.04	3
T2 west (hummock)	0-40	0.96	0.01	0.06	0.02	5
T2 west (hollow)	0-60	0.96	0.03	0.07	0.04	6
Average of all samples	-	0.97	0.02	0.05	0.03	33

A melt period was defined as the difference between two consecutive SGI surveys. Mean ice depth (+SD) below the peatland surface on May 3 was 12 cm (+2 cm) and increased to 20 cm (+3 cm) on May 9. This coincided with the highest melt rate and produced approximately 62mm of IWE, the highest release of water for the spring. This IWE was slightly lower than the combined total (80 mm) of rain (16 mm total, April to May) and end of winter SWE (SWE = 64 mm, data not shown) released during snowmelt at the end of April following the major snow event on April 16. Subsequent IWE was lower, coinciding with an increase in the number of measured ice-free survey points, and a decrease in the melt rate. A decrease in melting due to a snow event on May 14 also contributed to slower melt rates, reducing the IWE later in the melt period.

Using the mean ice depths for each survey date permitted an approximation of the depth where the water was being released. Approximately 89% or 141 mm of IWE (Figure 2-4a) was available in the top 33 cm of the peat profile (Figure 2-4b). The remaining 11% equated to 18 mm from May 23 to June 6.
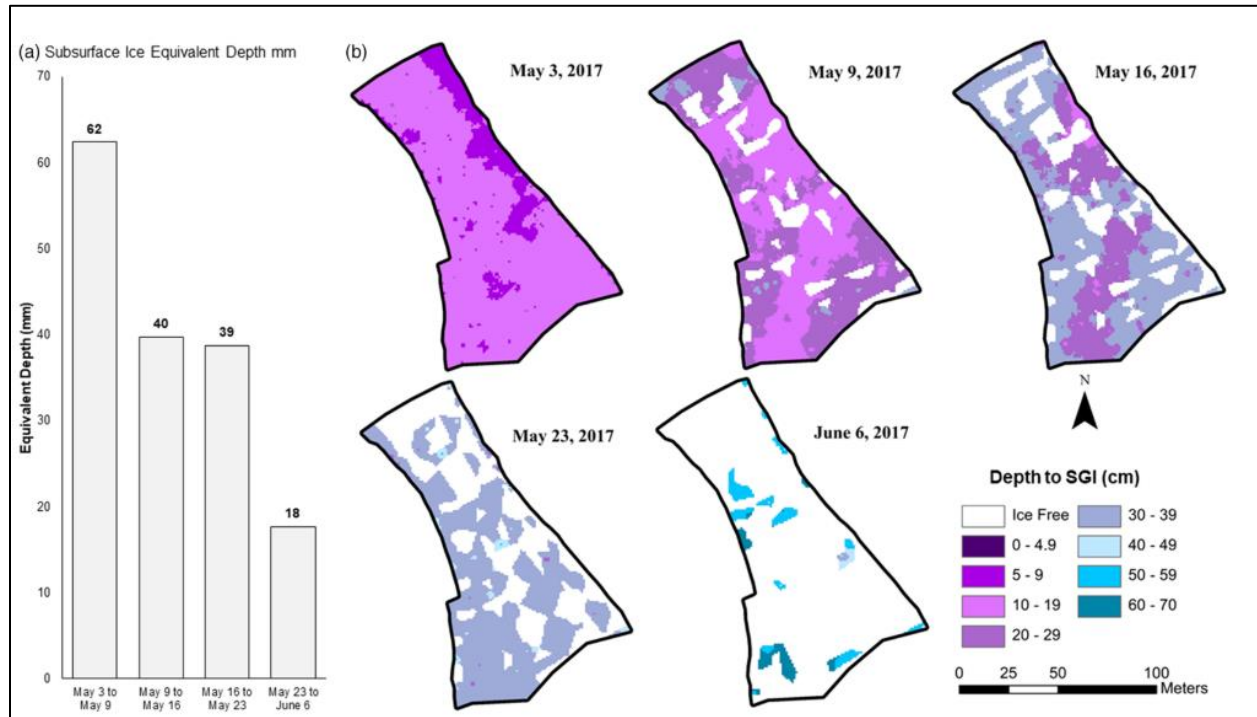
Figure 2-4 (a) The ice water equivalent released between each ice survey (b) maps showing the depth to SGI on each survey day.

2.3.2 SGI, water table, and soil moisture

For the 2017 study period, the water table was consistently above the upper boundary of the SGI. The relationship between water table and SGI is shown to have a significant negative linear relationship (Kendall tau $= -0.21$, $p < .01$; Figure 5a), where shallower ice depths are associated with greater water table depths.

When grouped by microtopographic form, water table depth and SGI exhibited a weak significant relationship (hummock Kendall tau $= -0.13$, $p < .01$; hollow Kendall tau $= 0.09$, $p < .05$; lawn Kendall tau $= -0.14$, $p < .05$). The water table showed a small decline in mean depth below ground sur- face from May 3 (3.4 cm + 8.8 cm) to May 23 (6 cm + 9.2 cm). Due to the snow event on May 14, the median water table rose to 3.3 cm above the ground surface on May 16. The VMC (top 5 cm) was relatively high across all three microforms on May 3 with median values of 92.7%, 86.5%, and 19.3% for hollows, lawns, and hummocks, respectively, but decreased with time

17

(Figure 6). By May 30, soil moisture had dropped significantly relative to initial measurements for hollows (57.7%), lawns (41.4%), and hummocks (9.7%; pairwise Wilcox, p< .01). The decline in VMC occurred along a microtopographical gradient, with hummocks being the driest (median range 9.7–17.8%) and hollows the wettest (median range 57.7–92.7%). The decline with VMC over May declined with an increasing depth to SGI (Kendall tau = −0.36, p< .01). When grouped by microtopographic forms (Figure 5b), there were significant negative relationships between SGI and VMC (hummock Kendall tau = −0.22, p< .01; hollow Kendall tau = 0.30, p< .01; lawn Kendall tau=-0.22, p<.05).
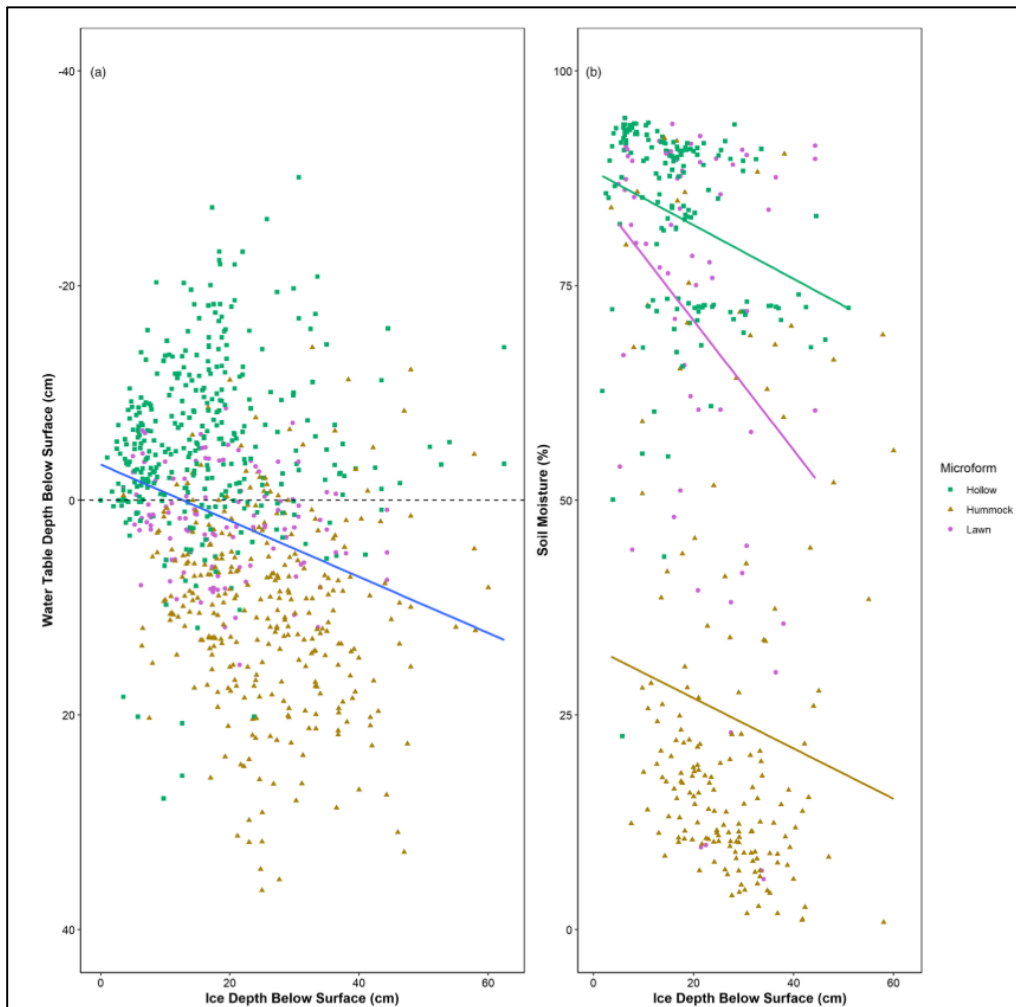
Figure 2-5 (a) The relationship between ice depth and water table. A significant negative relationship was found (Kendall tau = −0.21, p < .01); 0 indicates the peatland surface, where a negative value is above the surface and a positive value is below the surface. (b) The relationship between ice depth and soil moisture (0–5 cm). Significant negative relationships were found for all microtopographic forms (hummock Kendall tau = −0.22, p < .01; hollow Kendall tau = 0.30, p < .01; lawn Kendall tau = −0.22, p < .05.
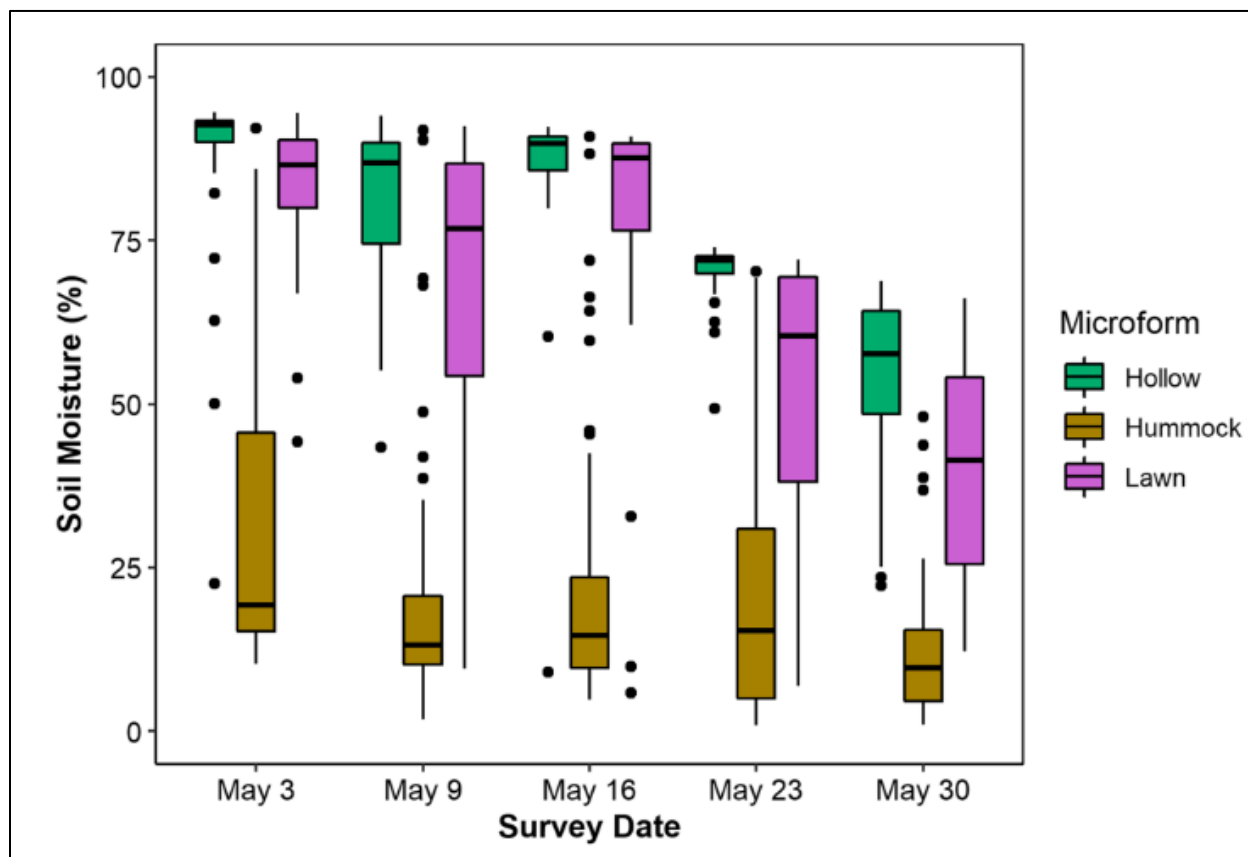
Figure 2-6 Soil moisture (0–5 cm) measurements grouped by microtopography for each ice survey day.

2.3.3 SGI, AET, PET, and ground heat flux

SGI began melting in April for 2015 and 2018, where the 2015 melt period totalled 7 days whereas the 2018 melt period totalled 3 days (Figure 2-7b). For both 2015 and 2018, depth to SGI and melt rate did not exhibit any significant relationships with daily AET in 2015 or 2018 (data not shown). However, there is a shift in the variability of daily AET that coincides with negative temperature gradients between 2 and 5cm below ground surface (Figure 7a). Under such conditions, daily AET varied considerably (mean = 1.3 mm/day, SD + 0.81 mm/ day, n = 26), but once the ice began to melt, the variability decreased (mean = 1.8 mm/day, SD + 0.36 mm/day, n= 16), and daily AET rates were between 2 and 3 mm/day. The transition from isothermal to negative temperature gradients coincided with the beginning of ice melt for 2015 and 2018 (Figure 7b).
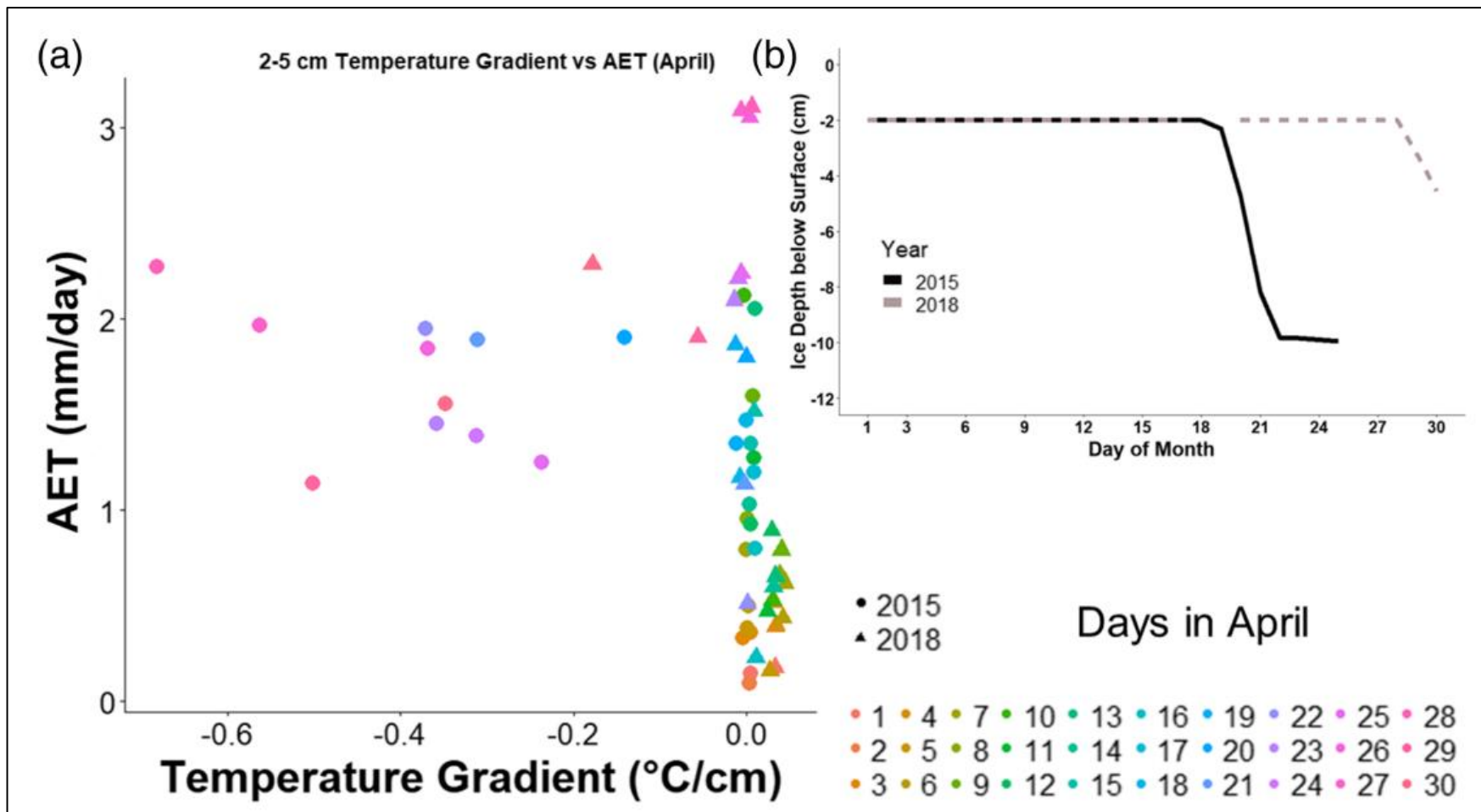
Figure 2-7 (a) Actual evapotranspiration versus the ground temperature gradient from the mid fen ground temperature monitoring station. (b) The depth to seasonal ground ice as measured from the MF ground temperature station for April in 2015 (solid black line) and 2018 (dashed grey line).
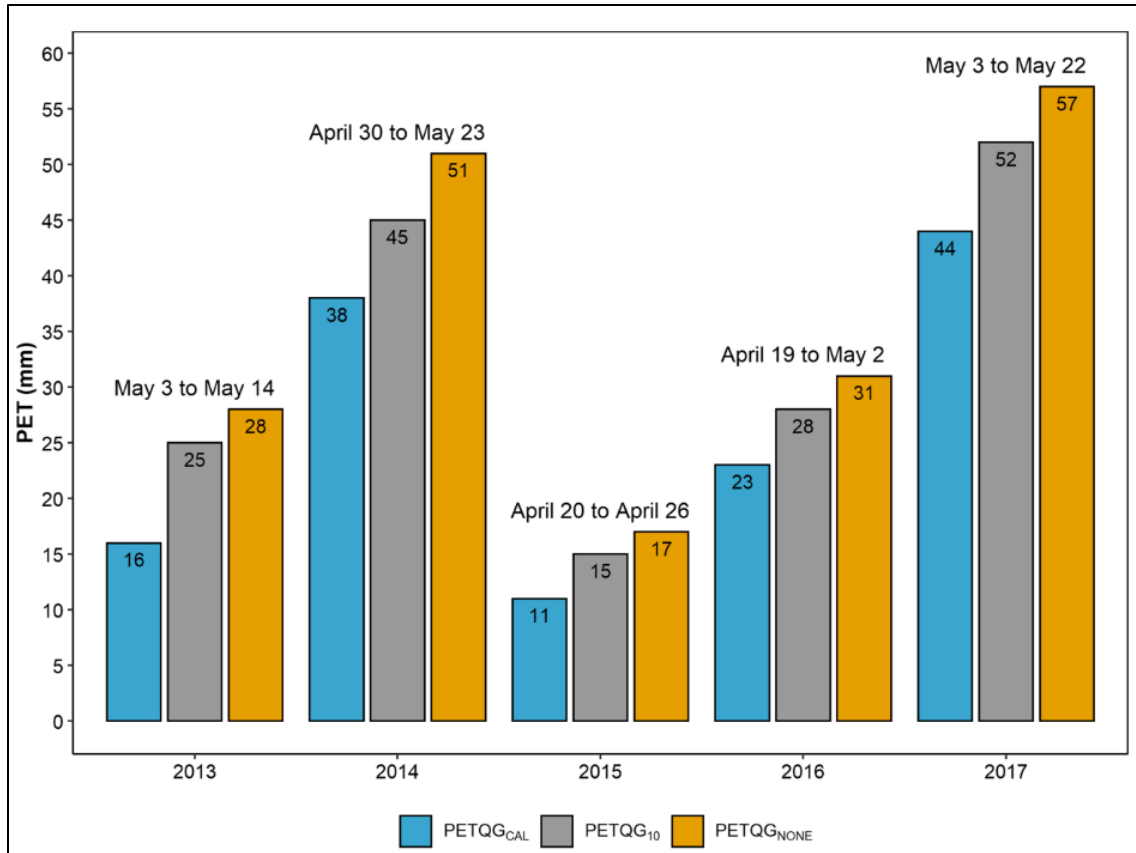
Figure 2-8 The reduction in potential evapotranspiration using three different ground heat flux approaches, the calorimetric method (PETQG$_{Cal}$), assuming Q$_G$ is equal to 10% of net radiation (PETQG$_{10}$), and not including the ground heat flux (PETQG$_{None}$). The melt period and time the model was run for are stated above each year.

For both 2015 and 2018, depth to SGI and melt rate did not exhibit any significant relationships with daily AET in 2015 or 2018 (data not shown). However, there is a shift in the variability of daily AET that coincides with negative temperature gradients between 2 and 5cm below ground surface (Figure 2-7a). Under such conditions, daily AET varied considerably (mean = 1.3 mm/day, SD + 0.81 mm/ day, n = 26), but once the ice began to melt, the variability decreased (mean = 1.8 mm/day, SD + 0.36 mm/day, n= 16), and daily AET rates were between 2 and 3 mm/day. The transition from isothermal to negative temperature gradients coincided with the beginning of ice melt for 2015 and 2018 (Figure 2-7b). The cumulative PET rates calculated for ground heat flux method for each year are shown in Figure 2-8. When including Q$_L$,Q$_G$ is increased thereby reducing the available energy for PET. Figure 2-8 shows an average 10-mm reduction when compared with PETQG$_{none}$ and an average 6-mm reduction when compared with PETQG$_{10}$ while ice is melting. The largest reductions in PET coincided with cooler air temperatures during the spring, such as 2014 and 2017, which also had longer melt periods (data not shown). In 2015

and 2016, when the spring was warmer, PETQG$_{Cal}$ was slightly lower. These springs also experienced shorter melt periods, with SGI free conditions occurring at the beginning of May (data not shown).

2.4 Discussion

2.4.1 Ice melt and IWE

In 2017, Pauciflora became SGI free approximately 1–2 months earlier than what was reported for other WBP spruce peatlands (Brown et al., 2010; Petrone et al., 2008; Thompson & Waddington, 2013). Pauciflora exchanges ground water with adjacent hill slopes (Wells et al., 2017), which means it is possible that bidirectional melting is reducing the time required for the peatland to become SGI free (FitzGibbon, 1981). Similar timing of SGI free conditions were reported by Smerdon & Mendoza, (2010) in a riparian peatland by the end of April, attributed to water exchanges with an adjacent lake. A 3-year study by Elmes et al., (2018) on a rich fen reported SGI free conditions, which ranged from late April to mid-May, which they attribute to low water tables prior to freezing, which prevented the formation of concrete SGI. The faster melting at Pauciflora was not expected due to the cooler climate compared with other WBP peatlands. Wetter surface conditions at Pauciflora may also have increased melt rates. The presence of water on ice enhances melting (Wright et al., 2009) due to its higher thermal conductivity relative to air (Todd, 1909). For Pauciflora, the elevated soil moisture in the upper 2–5 cm (Figure 2-6) may have offset the effects of its generally cooler climate.

The lack of significant differences in melt rate between each microform (Figure 2-3) is likely due to difference in the structure of the SGI (i.e., concrete vs. reticulate), thermal characteristics of the peat, and the methodologies employed. Only the melt rates of concrete SGI were considered, which does not capture the faster melting of reticulate SGI. The concrete SGI measured in the hummocks begins at approximately 30 cm below the ground surface. The lower thermal conductivity of thawed unsaturated peat (Farouki, 1981; Woo & Xia, 1996) and its ability to reduce ice melt (Jones et al., 2014) insulated the SGI under hummocks and slowed melting. This is indicated by the higher melt rates in hollows and lawns compared with hummocks during the first week of melt (Figure 3). The slightly higher rates in hollows and lawns are likely due to melt-water collecting in lower lying areas at the surface, which can preferentially melt the ice (Hayashi et al., 2007). This can create a positive feedback where depressions form in the SGI where

subsurface water can collect, further enhancing melt (Wright et al., 2009). However, as SGI continued to melt, there were no further differences between microtopographic forms' melt rate.

These negligible differences suggest that SGI does not have to melt beyond 5 cm below the hollow surface before differences in melt rate are reduced by the thermal properties of the peat overlying the SGI. Although unfrozen VMC at the base of hummocks was not directly measured, the relatively close proximity of the water table (Figure 2-5a) near the hummock base implies a high unfrozen VMC, likely similar to hollows and lawns. Additionally, ponded water over a hollow could move laterally into a hummock, providing additional thermal energy to melt SGI beneath the hummock. This could create similar thermal conditions between the base of the hummocks, hollows, and lawns, reducing melt rate variability. The transect point spacing (5m) within each transect may also impact the results. If a smaller spacing (≤ 1 m) was used, it is possible that different microforms closer to each other may exhibit different melt rates. However, at basin scale, these trends were not evident, which suggests that at a larger scale, the influences of microtopography on melt are negligible for Pauciflora.

As SGI melted, a considerable amount of liquid water (≈ 159 mm) was released in the near surface layers of the peat moss, of which 141 mm was released in the upper 30cm of the peat soil. The limited amount of water received via snowmelt (SWE ≈ 64 mm) and measurable rain (16 mm) during April and May of 2017 highlights the importance of this water from melting ice, particularly under the dry conditions typical in the WBP. While a long-term P record for Pauciflora does not exist, Wells et al., (2017) completed a 4-year study from 2011 to 2014 and found that the average P input for April and May is 69 mm, which was below PET (79 mm). This indicates that the release of melt water is important during the spring even for a wetter site such as Pauciflora. The impact of SGI may be larger for surface vegetation in drier peatland systems in the WBP. At a site with similar surface vegetation in the Alaskan Boreal Forest, Young-Robertson et al., (2017) have shown that vascular plants will tap into ice water under dry conditions. For *Sphagnum* mosses, which do not have root systems to tap into deeper water, wet conditions in part maintained by the SGI may provide optimal moisture conditions for mosses to begin photosynthesizing (Moore et al., 2006), which could increase moss resiliency to stress.

2.4.2 SGI-water table and near surface VMC

Although the high relative position of SGI likely promoted a high water table by blocking snowmelt from infiltrating (Ireson et al., 2015), only weak correlations between depth to SGI and

water table position were evident in the three microtopographic forms (Figure 2-5a) with hummocks and lawns exhibiting a weak negative relationship, whereas hollows had a weak positive relationship. This difference in relationship sign between microforms is likely due to the snow event that occurred on May 14 and the subsequent snow melt over the next 48hr, where hollows may have shown a more prominent response in water table depth. As SGI free areas opened, liquid water released from melting SGI would help offset the impact of water table drawdown from evaporation. Figure 2-5a shows that for all microtopographic forms, the water table was often within 20 cm of the surface (the 0 mark on the y-axis) for the duration of the ice surveys. The gradual increase in SGI free conditions with minimum change in water table depth suggests that the spatial continuity of SGI does not control the water table depth at Pauciflora during the spring. This could be because the water table depth is usually within 20 cm of the surface (Wells et al., 2017). However, if the lower boundary of the SGI and the water table depth is decoupled over winter forming an unsaturated zone beneath a SGI layer, it is possible that spatial discontinuities in SGI may be more important. Elmes et al., (2018) reported over-winter water table drawdown, whereas a frozen reticulate ice layer persisted in the top 20 cm of the peat. Although Wells et al., (2017) reported a water table increase over the winter at Pauciflora in 2011, it is possible that SGI could separate from the water table via other mechanisms due to frost heave (Kingsbury & Moore, 1987), moisture migration towards the freezing front (Cheng & Chamberlain, 1988; Talamucci, 2003), or if any outflow from the fen occurs after SGI formation. Decoupling of a frozen peat layer and the water table below has been reported before (Kingsbury & Moore, 1987). Rather quick water table drawdown was observed in the 2018 spring at Pauciflora where a change in surface ponding water of approximately 5 cm was noted relative to black spruce trunks over 3 days. However, thawing of any ice dam in the culvert may also explain the observed decrease in ponded water, by allowing for more rapid discharge from the fen. Further evidence is needed though to confirm whether the drawdown was due to a decoupled water table or the ice dam thawing in the culvert.

It was hypothesized that there would be a relationship between depth to SGI and VMC. Melting SGI close to the peatland surface would act as a close supply of water for the surface vegetation. As the depth to SGI increased, VMC decreased. However, the weak (Kendall tau = −0.36), significant (p< .01) relationship between SGI position and VMC (0–5 cm) appears to suggest minimal influence. There are several reasons why this maybe. First, the mean porosity of

the moss and peat (0–40 cm) in hummocks (mean porosity = 0.97 + 0.01, n = 20) and hollows (mean porosity = 0.96 + 0.02, n = 13), which is typical of peatlands in the WBP (Goetz & Price, 2015; Petrone et al., 2008; Redding & Devito, 2005), indicate large pores near the surface. Larger pores facilitate larger changes in VMC with relatively small increases in water table depth (Waddington et al., 2015) because larger pores will drain before smaller pores. For the upper layers of the moss, this may mean that there is no gradual decline in VMC with ice depth but rather a step change in soil moisture. Such a change is evident with hollows, where a clear drop from approximately 90% to 75% is evident (Figure 2-5b). However, this step change is not evident for hum- mocks and may be due to the VMC sampling location at the top of the hummock, where a larger step change in VMC may not be captured. An associated shift along the x-axis indicated that the drop may be a result of increasing depth to SGI, which also coincided with an increasing water table depth.

The generally weak relationships (Kendall tau < 0.3) for each microtopographic form may also be due to the site location. Pauciflora is a wet site (Wells et al., 2017) compared with other peatlands in the area (Elmes et al., 2018; Wells & Price, 2015), and the potential range of soil moisture during spring conditions was likely not captured in 2017 explaining the weaker relationships found between SGI and VMC. Further study is needed to assess this relationship under dry and wet spring conditions. Depth to SGI, water table depth, and VMC exhibited a general decline over May (Figures 2-2, 2-5, and 2-6), suggesting such relationships could be masked by the generally wetter conditions. Figure 2-5a shows that there is a significant relationship between SGI and water table depth at Pauciflora. Using microtopography as a proxy for variable SGI and water table depth, increasing depth to SGI is associated with generally drier conditions. This supports the hypothesis that melting SGI closer to the surface may indeed promote wetter conditions. The sharp drop in hollow VMC with increasing depth to SGI suggests that the impact of SGI on VMC may vary with microtopography.

2.4.3 SGI and evapotranspiration

There is a clear distinction between the soil temperature gradient and AET (Figure 2-7a) under isothermal conditions and when the ice is melting. AET ranges from 0 to 3 mm/day, but as the temperature gradient becomes negative (i.e., ice melt), AET becomes constrained to 1.5– 2.5 mm/day. The reduction in range of AET coincides with the beginning of ice melt in 2015 and 2018. This is indicative of the larger QG_L component of Q_G being considered and is caused by the

ice phase change to water (Hayashi et al., 2007; Woo & Xia, 1996), increasing Q_G and reducing available energy. Although these results support the findings of (Petrone et al., 2008) that the presence of melting SGI promotes AET, they also indicate that the melting SGI holds AET rates relatively constant. The reduced variability may lead to an overall reduction in AET, which may help keep WBP peatlands wet during drier springs. The overall impact of this potential influence will depend on the persistence of SGI. Also, it is possible that this effect could be reduced by lateral melting induced by ground water inputs as the SGI becomes spatially discontinuous. This means that the energy required for melting the ice is not being supplied entirely at the surface via conducted solar energy. To what extent this is occurring though is unknown and requires further study.

Increases in QG_L due to melting SGI also resulted in a reduction in PET across all 5years when compared with $Q_G = PETQG_{10}$ or $Q_G = PETQG_{NONE}$ (Figure 2-8). The average difference between $PETQG_{10}$ and $PETQG_{CAL}$, and $PETQG_{NONE}$ and $PETQG_{CAL}$ was small, averaging 6 and 10 mm, respectively. Over the typical melt period at Pauciflora (April to May), melting SGI led to decreases in cumulative PET, where longer melt periods resulted in differences of 2–4 mm compared with $PETQG_{10}$, increasing to 10–16 mm when compared with $PETQG_{NONE}$. For the annual water budget, a difference of 10mm can be enough to change a peatland water deficit, to a slight water surplus or net-neutral conditions (Wells et al., 2017). However, a difference of 10mm is also well within the range of error for most water budget studies, and as such its significance should be considered with some caution. Also, similar to the reduced effect discussed with AET, as the SGI becomes discontinuous, lateral melting could lessen the reduction in PET.

Furthermore, SGI free areas can open up over the course of the melt period suggesting that there are spatial differences in both the melt rate and ice thickness. These spatial differences would mean QG for peatlands is spatially variable, and possibly AET and PET. Despite these caveats, future studies should focus on incorporating QL into QG for peatlands that experience more frequent wet and dry cycles to better understand the relative impact of melting SGI on PET and AET. For this study, it was assumed that evapotranspiration was a function of available energy and atmospheric conditions, and was not limited by moisture. Towards the end of the spring season though, this assumption may not be true, particularly for sites with pronounced microtopography. Figure 6 illustrates that hummocks were consistently drier than hollows due to their elevated position. This means SGI would be deeper relative to the surface and may be insulated by the

26

overlying peat layers, leading to slower melt rates in hummocks compared with hollows such as between the May 3–9 ice survey (Figure 2-2). If the air during the spring is particularly dry, then water above the ice may evaporate more quickly than the melting SGI can supply liquid water. Such a scenario (Kingsbury & Moore, 1987) could slow melting, reduce the QG, and lead to desiccation. Similar results were shown under unsaturated conditions by Thompson & Waddington, (2013) who further suggested that the desiccation could be due to moisture migration within the microtopographic feature (Nagare et al., 2012). Whereas a reduction in melt may increase PET due to a smaller QG and increased available energy, there may not be an increase in AET. The reduction in VMC would lower the unsaturated hydraulic conductivity of the peat, and the moss would not be able to meet evaporative demand (McCarter & Price, 2014) possibly leading to desiccation. Surface desiccation was observed in some hummocks, with associated low (<5%) VMC during the 2017 spring at Pauciflora; however, the site scale impact was likely minimal. Further- more, the IWE (139 mm) exceeded PET (44 mm) during the melt period, indicating SGI would promote wet rather than dry conditions at Pauciflora. Unfortunately, there was insufficient data overlap between the AET dataset and spring SGI melt to assess the impact of SGI melt on AET across multiple springs. Future studies should investigate whether or not the melting of SGI reduces AET significantly below PET.

2.4.4 SGI's role in a headwater catchment peatland in the WBP

The role of SGI at Pauciflora may be most pronounced during the spring, when it can act as a moisture source and constraint on evapotranspiration. SGI melt did not begin until after the snow that fell on April 16 had melted, which resulted in low infiltrability for the peatland, and subsequently less snowmelt water likely remained within the peatland (Ireson et al., 2015; Watanabe et al., 2013). This suggests that for the 2017 spring, most of the 64mm of SWE was likely lost to run-off, evaporation, and sublimation and had a minimal contribution to early plant photosynthesis. The presence of SGI close to the peat surface (Figure 2-4) and a subsequent high water table (Figure 2-5a) created wet conditions, elevating near surface soil moisture conditions (Figure 2-6). Hummocks remained drier compared with hollows and lawns due to their elevated positions above the water table and SGI. As the SGI melted, the increase in water table depth was minimal ($\approx$3 cm below the peat surface in hollows), because SGI was converted to liquid water. The high amount of water released in the upper 30 cm supplemented any snowmelt loss from the peatland, reducing the potential for moisture stress conditions for surface vegetation. This amount

of water also supplements any snowmelt that was lost from the peatland. In this way, the melting SGI acted as a supplier of water for peatland vegetation, particularly in the absence of precipitation. This available water also resulted in evapotranspiration rates occurring closer to potential rates, which were lowered by reduced available energy from melting SGI (Figure 2-8). SGI acted both as an enhancement due to it supply of water and a constraint due to suppressed soil temperatures on evapotranspiration (Figure 2-7).

The water released by melting SGI is not "new" water being added to the peatland, and its position relative to the surface is likely a function of the antecedent moisture conditions prior to SGI formation. Lack of a SGI layer close to the peatland surface prior to melt may be due to a lower water table at the time of freezing. The coincidence of a low SGI layer and a drier spring may lead to early season moisture stress for peatland vegetation. SGI keeps a water source close to the surface, reducing the effects of water table drawdown. For our study area, a poor fen, (Wells et al., 2017) reported a steady increase in the water table over the winter from 2011 to 2012. Missing data over subsequent winters however limited these observations to only one winter. In a western boreal forest wetland basin, Price & FitzGibbon, (1987) found that whereas fens maintained water table levels at the freezing front, bogs experienced some water table drawdown over winter. Conversely, (Kingsbury & Moore, 1987) found that a "dehydrated" layer formed beneath the SGI but above the lower water table in a subarctic fen. This highlights that the role of SGI as a source of water may be more relevant for bogs than fens in the WBP. For a bog, any water table drawdown, over the winter after SGI formation, would not be replenished until after snowmelt, increasing the importance of SGI melt water.

This work was completed at a headwater catchment within the WBP, and as such the role of SGI in the WBP may differ depending on the amount of snowmelt, and peatland location within the land- scape. At the individual peatland scale, SGI importance to peatland vegetation may be higher when there is less snowmelt. Its contribution of a large amount of water to the surface in one event may help offset the effects of a drier spring. If there is little SGI present, and low water tables (i.e., increased peatland storage capacity) at the beginning of spring, this may decrease snowmelt run-off from the peatland. Given the potential hydrological importance of headwater peatlands such as Pauciflora (Wells et al., 2017) and the "downstream" impacts of headwater peatlands, this could mean that the presence and persistence of SGI in headwater catchment peatlands may impact the hydrological regime of lower elevation ecosystems.

2.5 Conclusion

This study highlights the potential roles of SGI during melt in a WBP peatland. Microtopography and soil moisture had limited influence on SGI melt as evidenced by similar melt rates across the site. The role of peatlands as a source area for run-off in this environment is aided in part by the presence of SGI due to its role in elevating the water table after the snowmelt period. The large amount of water released by melting SGI supplies water close to the surface while melting reduces PET. This lowers the upper limit of what AET could be, despite keeping AET close to PET, and reduces overall evapotranspiration rates from a peatland. This may be a mechanism that allows peatlands to persist in the subhumid WBP. Further research is needed to assess how these roles may vary across different peatland types, and under wet and dry cycles. Furthermore, the spatial characteristics of SGI melt are poorly understood, and an investigation into the controls on SGI melt may help elucidate the persistence of SGI influence on evapotranspiration during the spring. Finally, future modelling efforts should investigate how SGI might respond to a warmer climate and how that might impact its role within peatlands in the WBP. This work ultimately has improved our understanding of the role of SGI in WBP peatlands and can serve as a baseline comparison for future studies.

2.6 Acknowledgments

Chapter 3 : Quantifying the spatial variability of melting seasonal ground ice and its influence on potential evapotranspiration spatial variability in a boreal peatland

3.1 Introduction

Seasonal ground ice (SGI) forms in western boreal plain (WBP) peatlands in late October or early November (Van Huizen et al., 2019), and completely melts the following spring. The thick relatively impervious layers of SGI are able to form due to the high peat porosity in the surface peat and living moss layer (>90%, 0 - 40cm)(Petrone et al., 2008; Redding & Devito, 2005; Van Huizen et al., 2019) which allows for high water storage 15-20 times its dry weight (Halsey et al., 2000).

The length of the spring melt period can vary from year to year for an individual peatland (e.g. Chapter 2). For example, ground water inputs may lead to ice free conditions in the early spring (e.g Smerdon & Mendoza, 2010), or tree cover could allow for SGI to persist well into the summer months (Brown et al., 2010; Petrone, Devito, & Silins, 2008; Thompson & Waddington, 2013). The timing of SGI melting and ice free conditions impacts the magnitude of the spring freshet, which is heavily influenced by the presence of ice (e.g. Price & FitzGibbon, 1987), and can vary from peatland to peatland. During the spring, the thick layers of SGI require 331 J/g of ice to melt (Farouki, 1981), which can lead to a substantial decrease in available energy and subsequently potential evapotranspiration (PET) (Brown et al., 2010; Petrone et al., 2008; Van Huizen et al., 2019) which represents the upper limit of what actual evapotranspiration (ET) could reach. Both of these SGI impacts contribute to a peatlands role as a source of water within the WBP landscape (Thompson, Mendoza, Devito, & Petrone, 2015; Wells, Ketcheson, & Price, 2017), while the reduction in PET suggests that SGI melting could act as a limiter on water losses from the peatland (see Chapter 2).

The peatland role as a water source is magnified by the sub-humid climate in the WBP, where evapotranspiration (ET) is the dominant water flux, and PET commonly exceeds precipitation on an annual basis. Given the importance of ET fluxes to WBP peatland water balances (Helbig et al., 2020; Petrone, Silins, & Devito, 2007; Thompson, Mendoza, & Devito, 2017) and the negative feedback between available energy for ET and melting ice, it is important to have a firm understanding of how SGI impacts peatland hydrological function, particularly when developing representative hydrological models. However, uncertainties exist around how

melting SGI impacts may effect site scale estimation of ET and PET, due to the apparent high degree of SGI melt spatial variability that occurs (Van Huizen et al., 2019). Furthermore, the controls on SGI spatial variability are poorly understood.

The magnitude of the reduction in available energy for ET depends on how much SGI forms, how quickly it melts, and the total amount of energy (i.e. net radiation) at the surface. This relationship where ice melt reduces PET, can be evaluated in a peatland by using *in situ* measurements of SGI melt rate, which serve as an indicator of the total ground heat flux (Q_G). During the melt period, the energy consumed by the melting SGI (QG_L) often makes up 80 - 90% of Q_G, while the remainder of Q_G is allocated to the sensible heat flux (QG_S) (Hayashi etal., 2007; Lafleur etal., 1997; Woo & Xia, 1996). This Q_G value can then be incorporated into PET equations such as Penman (Penman, 1948) or Priestley-Taylor (Priestley & Taylor, 1972) where PET can be compared between melting and SGI free conditions (c.f. Chapter 2).

SGI and ET measurements, however, are often taken from one or two point measurements, which can create uncertainty when attempting to scale these effects from the plot scale ($< 1m^2$) to the peatland scale. Further, peatlands often have heterogenous cover conditions with differing microtopography (hummocks, hollows, lawns, ridges, pools) and surface vegetation (mosses, grasses, shrubs and trees), which change within horizontal distances ≤ 1 m. This heterogeneity can extend to larger scales (>100 m) where peatlands in the WBP can have sinuous boundaries and be interspersed within uplands (c.f. Elmes & Price, 2019), or located within varying topography such as flat terrain (c.f. Wells & Price, 2015), riparian zones (c.f. Smerdon & Mendoza, 2010) or distinct hillslopes (c.f. Wells et al., 2017). Environmental factors (air temperature, snow cover, stand density, topography) at both large and small scales may lead to spatial differences in the amount of SGI that forms during the winter, and influence spring melt rate. Therefore, developing a clear understanding of the spatial heterogeneity of SGI, specifically its melt rate and the amount that forms, is needed to better understand the overall effect of melting SGI on PET, and what constitutes a representative scale for this effect.

Spatial heterogeneity in peatlands has been explored, particularly when attempting to scale up carbon fluxes (Becker et al., 2008; Davidson et al., 2017) for the purposes of modelling climate change on continental scales. Carbon fluxes show distinct variation between differing microtopographic forms (Korrensalo et al., 2017; Strack et al., 2004) and vegetation types (Riutta et al., 2007; Strack et al., 2006), largely due to physiological responses to decreases in volumetric

moisture content (VMC), ground temperature at depth and water table position. These same variables also effect the thermal conductivity and heat capacity of the peatland surface (O'Donnell et al., 2009), which can influence the melt rates of SGI (Wright et al., 2009) and consequently the Q_G and PET.

As with carbon fluxes, spatial heterogeneity presents a challenge when attempting to scale evaporative fluxes from the plot scale to site scale. Point scale measurements are often deployed using a stratified sampling approach (Brown et al., 2010; Davidson et al., 2016; Riutta et al., 2007) in order to measure representative combinations of vegetation and microtopography (i.e. hummocks and hollows). Using a stratified approach is beneficial because obtaining a continuous spatial coverage is constrained by the number of chambers being used. To scale chamber ET fluxes to the site scale, areal weighting is a relatively simple technique to employ. Measured ET is averaged for each land cover group, which can be based on vegetation (Brown et al., 2010; Phillips et al., 2016) or microtopography (Becker et al., 2008). The average ET can then be multiplied by the areal coverage of their respective land cover type. However, this approach requires a suitable sample size that captures the intra-variability in ET fluxes within each land cover type. If the intra-variability of the fluxes is not properly captured with a suitable sample size, this average may not be representative of the spatial variation across the site (Becker et al., 2008). Such a scenario would lead to errors in estimating the site scale flux, creating uncertainty when using site scale fluxes for water budgets, or as inputs to larger models (Famiglietti & Wood, 1995).

Site scale measurements of ET can also be completed using eddy covariance systems. The spatial scale for these measurements is often an order of magnitude higher (10-100 m^2) than point scale measurements. However, EC measurements assume a homogenous landcover (Foken, 2009), which is rarely the case in boreal peatlands. As such, the larger scale spatial variability in ET also needs to be considered. Furthermore, if there is a potential for spatial variability in ET at the small scale due to spatial variations in SGI, then it is possible that this impacts the larger scale ET measurements. Like the potential controls on small scale SGI spatial variation (topography, vegetation etc.), these same variables can influence ET. For example, higher proportion of trees can lead to an increase in shade, reducing available energy for ET at the surface (i.e., mosses and vascular shrubs). Depending on the amount of trees and exposed moss, there can be stark differences and between the contributions of moss and trees to total ET (Gabrielli, 2016). Variable vegetation cover can also lead to varying ET in a wetland (Brown et al., 2010), due to physiological

differences (vascular versus non-vascular plants) or due to size (shrubs versus trees). To measure this spatial variability in SGI, a systematic approach (e.g., grid based survey) using the steel rod method (Woo & Xia, 1996) that can cover wide spatial areas is advantageous. Using this approach allows for the investigation of environmental phenomenon at different scales (e.g., Petrone et al., 2004; Mitchell et al. 2008).

However, the uncertainty around ET estimates at small and large scales in relation to melting SGI warrants further investigations into whether spatial variability in SGI translates to spatial variability in ET. Insight into these small scale processes will provide a better understanding of site scale fluxes (A. J. Baird et al., 2013). Furthermore, determining what scale of spatial heterogeneity should be explicitly modeled will provide more information on modelling complexity (Famiglietti & Wood, 1995).

Therefore, the objectives of this chapter are to (1) quantify the effect of ice thickness and melt rate on peatland PET; (2) quantify the spatial variability of SGI thickness and melt rate across spatial scales; and (3) assess how/if spatial variability in SGI thickness/melt rate affects site scale PET.

3.2 Study Area and Methods

3.2.1 Study Area

To assess the spatial variability of SGI, a field study was completed over two spring seasons in May, 2017 and April-May 2018 at a 11 ha poor fen (56°22′30.36″N, 111°14′3.29″W), herein referred to as Pauciflora (Bocking, Cooper, & Price, 2017; Goetz & Price, 2016; Van Huizen et al., 2019; Wells et al., 2017). Pauciflora is located approximately 40 km south of Fort McMurray, Alberta, Canada (Figure 1a,b), and located on the Stoney Mountain complex, within the WBP. The 30-year climate normal for the area (Fort McMurray Airport, Environment and Climate Change Canada) show a mean temperature of 1.1°C, while the mean rainfall and snowfall are 307 mm and 104 mm, respectively. However, the climate at Pauciflora is slightly wetter and cooler (Wells et al., 2017), likely due to its elevated position (~367 m higher than the Fort McMurray Airport) causing orographic precipitation (Wells et al., 2017). The fen is bounded by a road to its north, where a culvert acts as an outlet for the fen, while the rest of the fen is bounded by forested hillslopes that vary in steepness. Field data was collected within a 0.93 ha area of the fen comprised of a sparsely treed area of the fen (peat thickness ≈ 4m) (Figure 1 c). This part of the fen is bounded by particularly steep forested hillslopes to the east (max slope of 28°) and west (max slope of 26°)

where the trees comprised *Pinus banksiana* and *Populus tremula*, and are an average height of 12 m (±6 m) and 14 m (±5 m) above the peatland surface (Figure 3-1d). Trees within the peatland are comprised of *Picea mariana* and *Larix laricina*, while understory vegetation is comprised of *Ledum groenlandicum*, *Campadaphne calyculata* and a carpet of *Sphagnum* moss. A detailed description of the fen vegetation and the hydrogeological setting can be found in Bocking et al. (2017) and Wells et al. (2017), respectively.
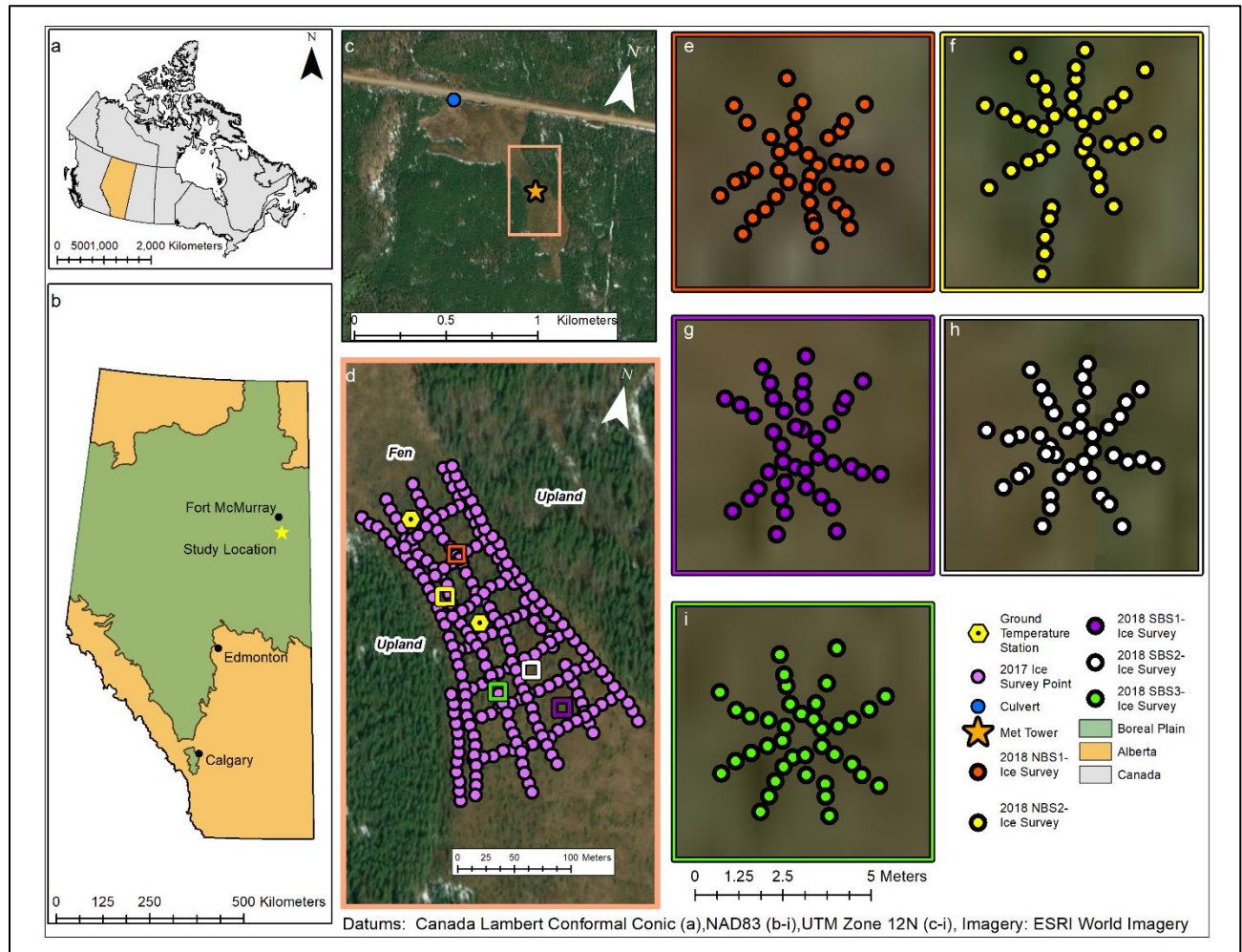
Figure 3-1(a,b) Location within Canada. (c) Study site was a poor fen located on top of Stoney Mountain, approximately 40 km south of Fort McMurray. (d) 2017 large-scale ice survey. Thirteen transects were laid out with a 5 m spacing between each point. Depth to ice was measured using the steel-rod method. (e–i) 2018 small-scale ice surveys. Five black spruce trees were chosen and eight transects were centred on each tree with a 0.5 m spacing. NBS refers to the North Black Spruce trees, SBS refers to the South Black Spruce Trees. North and South are relative to the EC tower.

3.2.2 Micrometerological Variables

Relative Humidity (%), air temperature (°C), net radiation (W/m^2) and windspeed (m/s) were measured at 60 s intervals using a CR1000 data logger (Campbell Scientific Ltd., Logan,

Utah) and averaged at 30-minute intervals. Relative humidity and air temperature were measured 2 m above the peatland surface (HMP35C, Vaisala, Helsinki, Finland). Net radiation (Q*) (CNR4 Net Radiometers, Kipp & Zonen, Delft, Netherlands) and windspeed and direction (RM Young 05103, Campbell Scientific, Logan, Utah) were measured 6 m above the peatland surface.

3.2.3 Sensitivity Analysis for PET

A sensitivity analysis for PET to melting SGI and SGI thickness was completed using the Penman-Monteith equation and ground temperature data. Daily melt rate was derived from two thermocouple profiles installed in 2013 and 2016 in hollows, converted to an equivalent latent energy (Van Huizen et al., 2019) for all melting that only occurred from above. The latent energy was incorporated into the ground heat flux (Q$_G$) using the calorimetric method (Halliwell & Rouse, 1987) where Q$_G$ is partitioned into a latent heat (QG$_L$) and sensible heat (QG$_S$) components. This Q$_G$ was then incorporated into the Penman equation (Penman, 1948) to calculate PET,

$$PET = \frac{\Delta(Q^* - Q_G) + \rho_a c_p C_{at}(e* -ea)}{\rho_w \lambda_v (\Delta + \gamma)}$$

(3-1)

where PET is the daily PET (mm), Δ is the slope of the vapour-pressure vs. temperature curve (kPa/°C), γ is the psychrometric constant (0.00662 kPa/°C), Q^* is the daily cumulative measured Q* (MJ), ρ_a is the density of air (kg/m^3), c_p is the specific heat of air (MJ/kg K), C_{at} is the aerodynamic conductance (m/day), ρ_w is the density of water (kg/m^3), e^* and ea are the daily average saturated (kPa) and daily average actual vapour pressures (kPa) respectively, and λ_v is the latent heat of vaporization (MJ/Kg) for water. PET was calculated using melt rates of 0, 0.01, 0.02, 0.03, 0.04 and 0.05 m/day, assuming scenarios of 0.18 m and 0.32 m of total ice to melt. Both total amounts were measured at thermocouple profiles in hollows during 2017. The thicker ice was measured in a more treed area, while the thinner ice was measured in a more open area and are representative of conditions observed in this peatland.

3.2.4 Seasonal Ground Ice Survey

Each ice survey was completed using the steel rod method (Woo & Xia, 1996). In 2017, 240 survey stakes were installed over six north-south transects and seven west-east transects, with 5m spacing between each point within a transect (Figure 1d). At each point, an average of four depth to ice measurements were taken weekly. In 2018, five *Picea mariana* (NBS1, NBS2, SBS1, SBS2 and SBS3) were selected as a central location around which 40 survey points were set up

into 8 transects, at 0.5 m spacing between each point within a transect (Figure 3-1e,f,g,h,i). To minimize compaction, only one depth to ice measurement was taken for the 2018 survey, every 2 to 3 days. The difference between the first and last depth to ice measurement before ice was no longer found is assumed to estimate the ice thickness. Average melt rate was determined by dividing the ice thickness over the melting period for each surveyed point. Each survey point was classified as a hummock, hollow or lawn. VMC was measured at the same time as ice depth, in triplicate and averaged at every second survey point 2017 and every point in 2018, using a WET-2 Soil Water Sensor (Delta-T Devices, Cambridge, UK), using organic soil parameters as defined by the moisture meter. VMC values were subsequently calibrated using seven cores (0-10 cm below the ground surface). A calibration curve was created by comparing gravimetric moisture content to the volumetric moisture content as measured by the wet sensor. VMC measurements from the field were subsequently corrected using a 3rd order polynomial (Appendix A, Figure A1) which had an R^2 of 0.94. A dual-frequency survey-grade differential global positioning system (DGPS) (Topcon GMS-2, 2011-2012; Leica Viva GS14, 2014) quantified the longitude, latitude and absolute elevation of each survey point (±0.05 m).

3.2.5 Hillshade Modelling and Tree Analysis

To compare shading from the hillslopes to ice thickness and average melt rate at the large scale (2017 data), a hill shade analysis was completed using the *Hillshade Tool* in ArcMap 10.1. and a digital surface model. Raster surfaces of cumulative shade hours for the first, middle and last day of each winter month (October - March) and spring (May) were created, and summed, to create a cumulative winter shade surface. This surface represents the potential maximum number of shaded hours assuming clear sky conditions. It was compared to the ice survey points that were found to be significantly clustered. Tree locations were determined by digitizing tree locations using aerial and satellite imagery and on-site observations. The distance between an ice survey point and the closest tree was determined using the *Near Tool* in ArcGIS 10.1 (ESRI, Canada). 2018 comparisons were completed by comparing both ice thickness and average melt rate to the distance to the center tree and spring shaded hours.

3.2.6 Net Radiation and Spatial PET Modelling

Q* and spatial PET modelling were completed for the 2017 ice survey dataset. To model Q* at each survey point, the Solar Radiation toolset was used within ArcMap 10.1. The Points Solar Radiation tool was used to calculate cumulative incoming shortwave radiation (Fu & Rich,

2002) at each point from May 1 - 31. Each day was classified as Clear, Generally Clear, or Cloudy sky or cloudy conditions (see Table A1 in Appendix A) based on observed Q* values and sub-daily site images that included the sky taken from a camera located within the study area. Values for proportions of diffuse shortwave and atmospheric transmittivity (Table A1, Appendix A) values were based on the recommendation of tool manual (ESRI, 2016), where typical transmittivity values of 0.6-0.7 are observed for clear sky conditions, and 0.5 for generally clear sky conditions. The diffuse proportion is the inverse of the transmittivity value. These values were manually adjusted for each day and determining which provided the best fit for net shortwave radiation measured at the met tower. A hemispherical viewshed raster was created for each survey location with a digital surface model (2m resolution) that included the trees within the peatland. Using a constant albedo value of 0.205, typical for snow free conditions in a peatland (Thompson et al., 2015), daily cumulative net shortwave radiation (K*) was determined for each day. K* was converted to Q* using a linear relationship developed between Q* and K* from 2018 data via,

$$Q^* = 0.8099 \cdot K^* + 87.823$$

(3-2)

which had a R^2=0.99. The daily cumulative Q* from the tower was compared to the closest (<5 m) surveyed point. An R^2 of 0.7 was found between modelled Q* and observed Q* (Appendix A Figures A2 & A3) indicating a reasonable approximation.

PET was calculated for each day at each ice point using the Priestley-Taylor equation,

$$PET = \frac{\Delta \cdot (Q^* - QG)}{\rho_w \cdot \lambda_v \cdot (\Delta + \gamma)}$$

(3-3)

where PET is a daily value (mm/d), Δ is the slope of the saturated vapour pressure curve (°C/kPa), ρ_w is the density of water (g/m^3), γ is the psychrometric constant (kPa/ °C), λ_v is the latent heat of vaporization (2.45 MJ/g), Q^* is the sum of daily positive Q* values (MJ/m^2) taken from the short wave model and Q_G is the ground heat flux (MJ/m^2) as determined by the average melt rate between each ice survey. This PET represents equilibrium potential evapotranspiration, which is a lower bound of the range in possible PET (Granger, 1989). For our purposes, the daily average temperature from the tower was used to calculate Δ and γ for each survey point.

3.2.7 Spatial Variability Assessment

Spatial variability for SGI thickness, melt rate and PET were assessed using the following approach using ArcMap 10.1 (ESRI, Canada). The spatial scale at which spatial autocorrelation is occurring was first assessed for Ice thickness, Melt Rate and Total PET using the Incremental Global Moran's I tool, which runs a Global Moran's I at increasing neighbourhood distances, and assesses at what distance processes controlling spatial autocorrelation is most pronounced. The Anselin Local Moran's I (Anselin, 1995) was used to identify any spatial outliers for Ice Thickness and Melt Rate. These spatial outliers were removed from the dataset for subsequent analysis because they are not representative of the bulk spatial structure inherent in the dataset and may be representative of different phenomenon controlling the spatial pattern at a different scale.

Global Moran's I does not indicate where within the dataset any spatial clustering is occurring, and so the Hot Spot Analysis tool was used, which identifies clusters of high values (ie. thicker ice, faster melt rates, higher Q* and higher PET) and clusters of low values (ie. thinner ice, slower melt rates, lower Q*, lower PET) using the Geti-I* Statistic (Getis & Ord, 1992). The output from this tool includes a z-score based on a normal distribution, and a p-value. The combination of a high (> 1.65) or low (< -1.65) z-score and p-values < 0.1 indicates whether the observed spatial clustering is significantly different from a random distribution of the ice thickness or average melt rate at the same locations. To investigate what is controlling any spatial clustering that may be present, values of high and low clusters will be compared to spatial datasets including hill shading, proximity to trees, tree density, and Q*.

3.3 Results

3.3.1 Sensitivity Model

Results from the sensitivity model show that on a daily timestep, reductions in PET from melting SGI were ≤ 1 mm/day. However, this corresponded with larger reductions in total PET for the month (Figure 3-2, Table 3-1). Under no ice conditions, total PET was 102 mm for the month of May. The presence of melting SGI at 1 cm/day caused a reduction of 8 mm when there was 18 cm of ice to melt and increased to 14 mm when there was 32 cm of ice to melt. However, further reductions in total PET with increasing melt rate were minimal (0 - 1 mm). Consequently, PET appears to be more sensitive to differences in ice thickness, which led to a larger decrease in total PET compared to increasing melt rate.
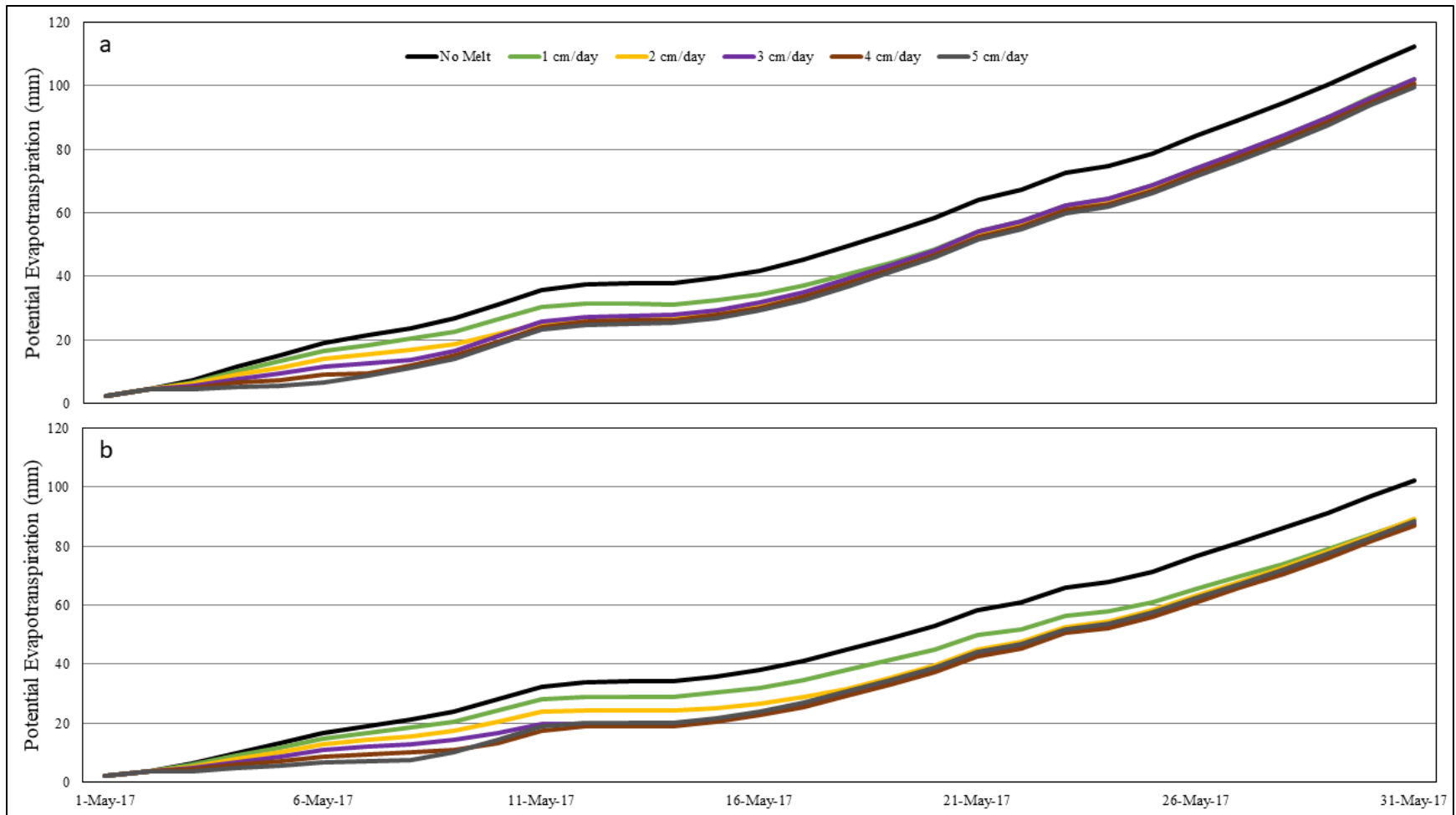
Figure 3-2 Sensitivity analysis results. (a) Cumulative PET with 18 cm of ice to melt. (b) Cumulative PET with 32 cm of ice to melt.

Table 3-1 Results from the sensitivity analysis

Melt Rate	Cumulative Potential Evapotranspiration (mm)	
	32 cm of ice	**18 cm of ice**
0 (no melt)	102	102
1 cm/day	89	95
2 cm/day	89	93
3 cm/day	88	94
4 cm/day	87	93
5 cm/day	88	92

3.3.2 Scales of seasonal ground ice spatial variability

The results from the Global Moran's I (Appendix A, Table A2) and hot spot analysis (Figure 3-3a,b) indicate that peak spatial autocorrelation occurred at a scale of 30 m for the ice thickness large-scale dataset. Two distinct areas of ice formed along the southwestern edge of the study area, while three distinct thinner areas of ice formed along the eastern portion of the study area (Figure 3-3b), with an average difference in ice thickness of 0.09 m (± 0.06 m).
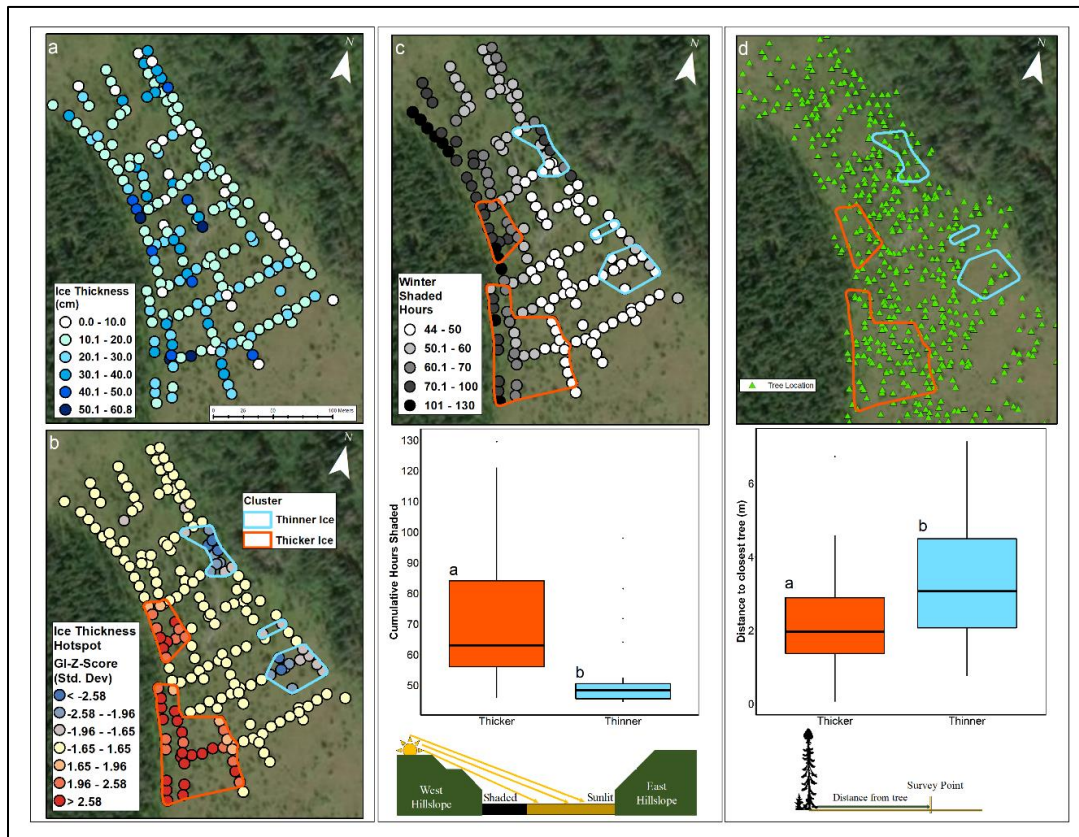
Figure 3-3 (a) 2017 ice thickness. (b) Ice thickness clusters (orange = thicker, blue = thinner) (c) Upper; modelled cumulative winter shaded hours. Below; Box plot showing significant difference in Winter Hillshade between ice thickness clusters. (d) Upper; location of trees within ice thickness clusters. Lower; Box plot showing significant difference in distance between the closest tree and ice thickness of the closest point.

Average melt rate also exhibited large scale spatial autocorrelation, which peaked at a scale of 60 m. Three distinct clusters were found: two in the northern part of the study area, and one in the southern part of the study area (Figure 3-4b). Melt rates in the northern section were significantly higher (Wilcox, p-value <0.05), on average 0.01 m/day (± 0.003 m/day) faster than the melt rates from the slower cluster.
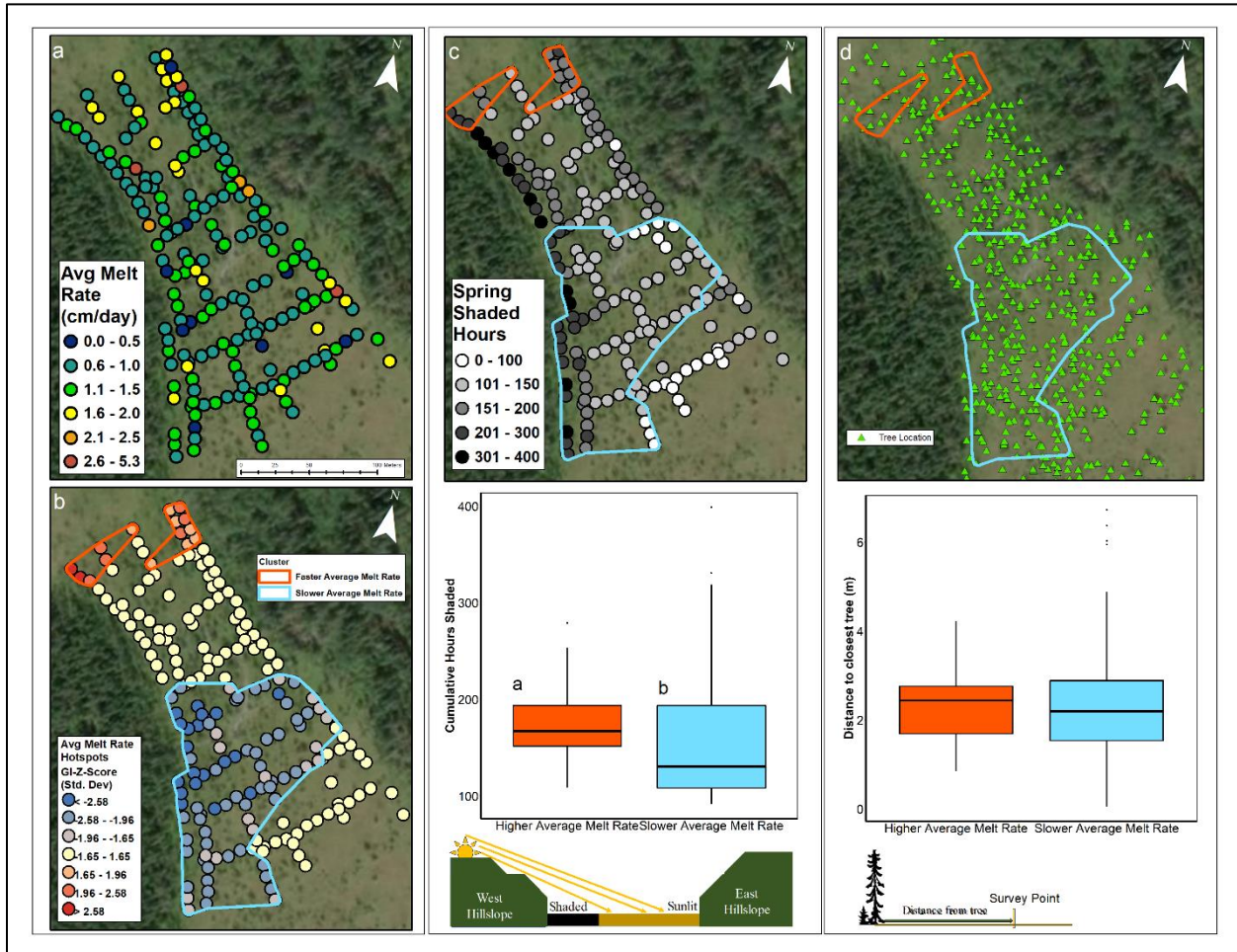
Figure 3-4 (a) 2017 average melt rate. (b) Melt rate clusters (orange = higher melt rate, blue = slower melt rate) (c) Upper; modelled cumulative spring shaded hours. Below; Box plot showing significant difference in Spring Hillshade between melt rate clusters. (d) Upper; Location of trees within melt rate clusters. Lower; Box plot showing no significant difference in distance between the closest tree and melt rate of the closest point.

Small scale spatial variability was analyzed using the 2018 dataset where ice surveys were centered around 5 black spruce trees (Figure 3-5). Ice thickness and average melt rate spatial variability were analyzed on points pertaining to each individual tree. Spatial clustering was present around SBS1, SBS3, NBS1 and NBS2 for ice thickness, where clusters of thick ice were present around the center tree, while thin points were found further away (Figure 3-5a). Due to small sample sizes but similar spatial patterning for ice thickness between the trees, the data from all four trees were

combined for subsequent analysis. Individual differences for each tree are reported in Table A3 in Appendix A. The median difference in ice thickness between the thick and thin clusters was 0.14 m. Average melt rate exhibited limited spatial clustering and was only present in SBS1 and SBS3 (Figure 3-5b). There were commonalities in the melt rate spatial pattern though, as the cluster of slower melt rates appeared to be on the northern side of the trees while faster melt rate clusters were found on the southern side of the trees. However, the majority of the melt rate data for each tree was spatially random. The average differences in melt rate between thick and thin clusters was 0.03 m/day (± 0.007 m/day).
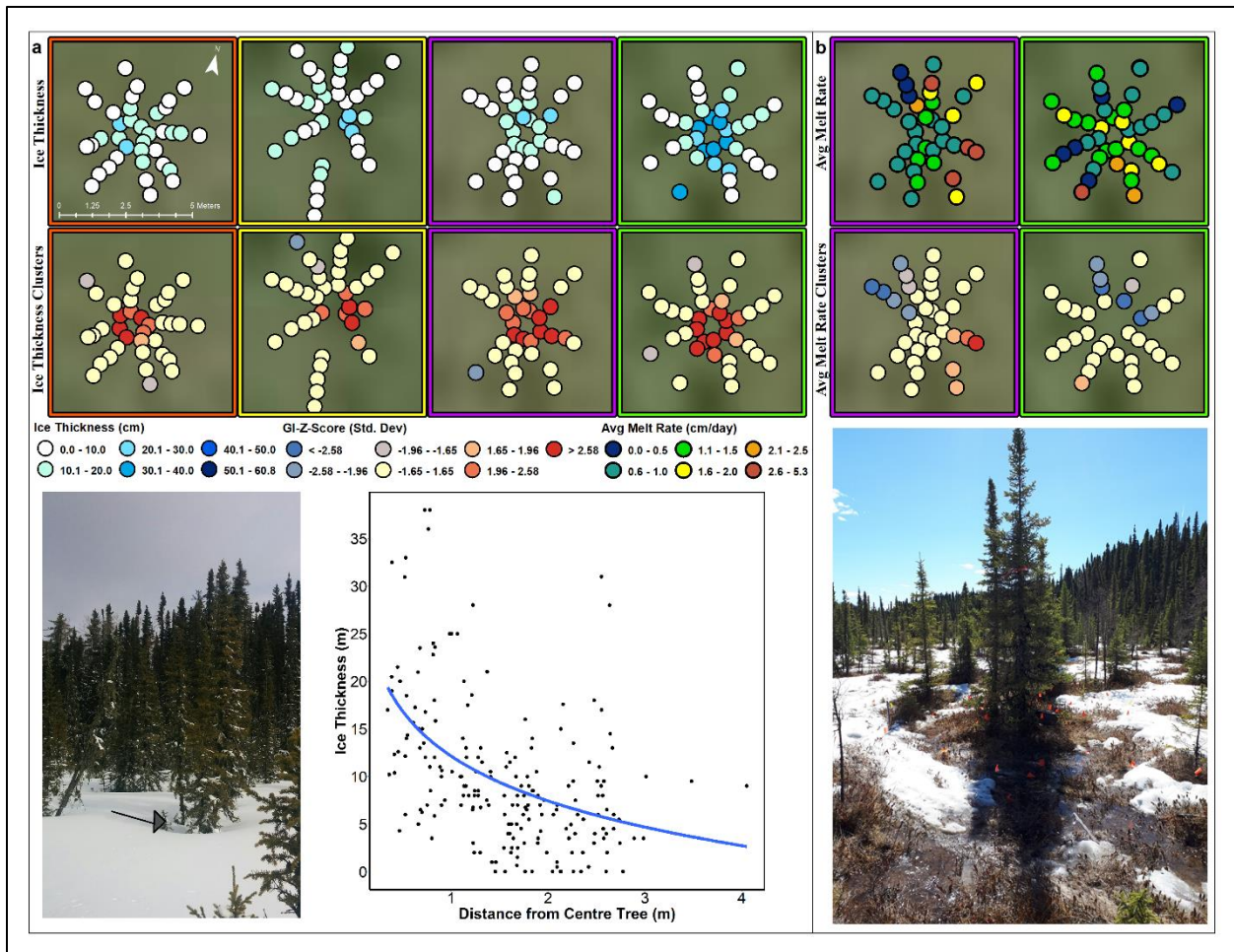
Figure 3-5(a) Upper row; 2018 ice thickness. Lower row; ice thickness clusters (orange = thicker, blue = thinner) Picture left; Arrow shows the slope of the snow around a tree, indicating a tree well where snowpack thickness decreases. Scatter plot; distance to the centre tree vs. ice thickness. (b) Upper row; 2018 average melt rate below. Lower row; Average melt rate clusters (orange = higher melt rate, blue = slower melt rate). Picture; A shadow tracks across the northern side of the tree on a sunny day.

Table 3-2 Proportion of different microforms between thick and thin ice clusters, and average ice thickness (m)

	Hollow	**Hummock**	**Lawn**
2017 thick ice clusters			
Count	18	24	4
Average ice thickness (m)	0.29	0.24	0.22
2017 thin ice clusters			
Count	7	8	9
Average ice thickness (m)	0.17	0.16	0.19

3.3.3 Driving factors in Spatial Variability in SGI

Ice thickness spatial variability in 2017 was compared to winter hill-shading, tree density, distance to trees, and microtopography, while average melt rate spatial autocorrelation was compared to spring hill shading, Q*, soil moisture, and microtopography.

Visual interpretation suggests that large scale ice thickness patterns coincided with large scale winter hill shade patterns. The western margin of the fen received on average 23% (±13%) more shade over the winter compared to the eastern margin of the fen (based on the maximum amount of shade received), which was a significant difference (Wilcox, p-value <0.01). This area of increased winter shade coincided with the two clusters of high ice thickness (Figure 3-3c). However, no significant correlations (Spearmans Rho, p-value >0.05) were found within clusters of thick ice or thin ice between both ice thickness and winter shade, or when grouped by the entire dataset.

Surveyed points within the thick ice clusters were significantly closer to individual trees (Wilcox, p-value <0.01) compared to points inside the thin clusters, where the average distance to a tree was 2.2 m (min = 0.058 m, max = 6.7 m) for thick clusters, and increased to 3.3 m (min = 0.77 m, max = 7.1 m) for thin clusters. Both the hot and cold clusters of ice thickness had similar proportions of hummocks, hollows, and lawns, with little difference in average ice thickness within each grouping (Table 3-2).

For small-scale spatial patterns, thicker ice exhibited a non-linear relationship with distance to the center tree (Figure 3-5a) where a threshold response was evident. Surveyed points within 1 - 2 m of a tree were often thicker than surveyed points outside of the tree. This relationship manifested itself in the spatial pattern as well, where significant clusters of thicker ice formed closer to the tree than ice further away for 4 of the 5 trees surveyed (Figure 3-5a). Median ice

thickness for all significantly thicker clusters was 0.18 m, which was significantly higher (Wilcox, p-value <0.05) than the median ice thickness for the thinner clusters (0.04 m). Winter hill-shading from adjacent hill slopes did not exhibit a significant relationship with small scale ice thickness clusters (Wilcox, p-value <0.05). There were no significant differences between ice thickness for hummocks and for hollows within the greater ice thickness clusters.

3.3.4 Melt Rate

Melt Rate was compared to near surface VMC, Q*, and Distance to tree. Median near surface (0 - 5 cm) VMC, was compared between the faster and slower melt rate clusters. The median VMC for slower melt rates (54%,9- 64% IQR) was higher compared to the median VMC for higher melt rates (19 %, 10 - 63% IQR). There were also no significant differences (Wilcox, p-value>0.05) between median VMC when grouped by microform and cluster. Hummock VMC's were 5%, IQR 3 – 7%, for the high melt rate cluster and for the low melt rate clusters were 6%, 1 - 20% IQR). For hollows, VMC values were similar between melt rate clusters with no significant differences (Wilcox, p-value >0.05). The higher melt rate clusters had a median VMC of 63 % (IQR 52 – 79%) compared to the lower melt rate clusters, which had a median VMC (64 %, IQR 60 – 70%).

Q* was found to be significantly different between the two main melt rate clusters (Wilcox, p-value <0.05). However, the higher melt rate cluster was associated with lower Q*, where the median cumulative Q* was (376 MJ, IQR 376 – 424 MJ) compared to the lower melt rate cluster that had a higher median Q* (460 MJ, 395–490 MJ), which was unexpected. As expected, spring hill-shading from the adjacent slopes exhibited the opposite pattern between the two melt rate clusters, where the slower melt rate cluster had significantly less shade (131 Hours, IQR 109 – 194 Hours) (Wilcox, p-value >0.05) compared to the higher melt rate cluster (167 Hours, IQR 152 - 194 Hours). Distance to tree did not exhibit any significant difference between melt rate clusters.

For small scale melt rate, only two of the five trees (SBS1 & SBS3) exhibited any spatial autocorrelation for average melt rate (Figure 2b). Due to the small spatial footprint, each cluster for each tree was only made up at most of 7 points and at minimum of 1. Therefore, each slow melt rate cluster was combined, and each fast melt rate cluster was combined (Slow melt rate n=14, fast melt rate n=6), however this was insufficient sample size for robust statistical difference testing when comparing to controlling variables. Median VWC for the higher melt rate cluster was 63% (50-70% IQR) while the slower melt rate clusters had a median VWC of 53% (39-56% IQR).

The total spring hillshade (May1-May16) exhibited small differences between the higher and slower melt rate clusters, ≈1 hour for SBS1 & ≈6 hours for SBS3. However, there does appear to be a relationship for two trees (SBS3, SBS1) between the location of the cluster and the aspect of the tree. Figure 5b shows that slower melt rates on the northern side and faster melt rates on the southern side of both SBS3 and SBS1.. The image in the bottom of Figure 3-5b highlights how the position of the tree (SBS3) led to a shadow that moves in a west to east pattern, ≈175°- 90°.

3.3.5 PET Spatial Variability

Cumulative PET exhibited distinct zones of spatial variability (Figure 3-6), where peak spatial autocorrelation occurred at a scale of 50 m.
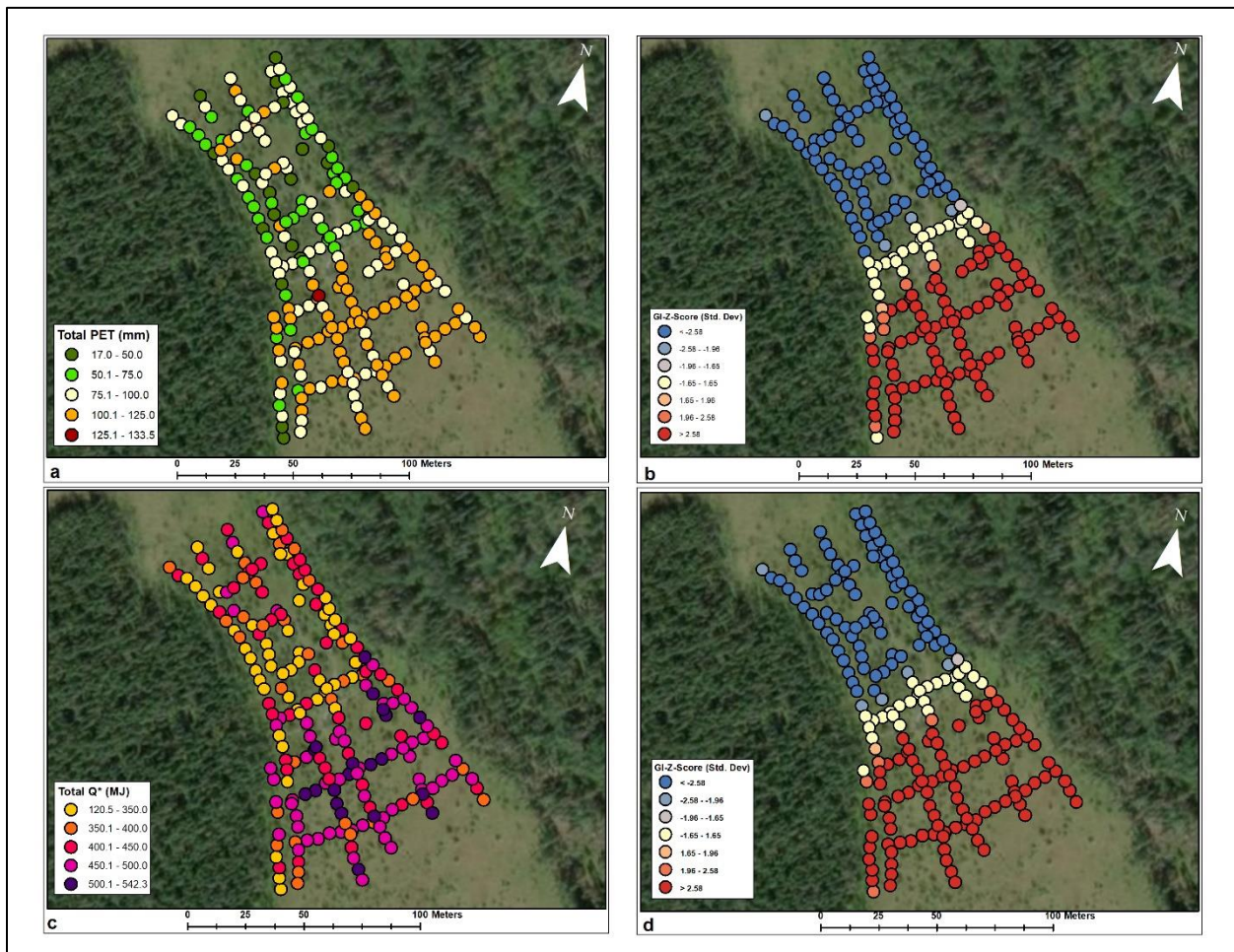
Figure 3-6 (a) May 2017 cumulative potential evapotranspiration. (b) Cumulative potential evapotranspiration clusters (red = higher potential evapotranspiration, blue = lower potential evapotranspiration). (c) May 2017 cumulative net radiation. (d) Cumulative net radiation clusters (red = higher net radiation, blue = lower net radiation).

Two distinct clusters of higher and lower cumulative PET formed, effectively splitting the study area in half, with lower PET in the northern part and higher PET in the southern area. A visual

comparison of these spatial patterns to the spatial patterns in ice thickness and melt rate show no obvious correlation. Grouping the PET by ice thickness clusters and melt rate clusters showed no significant differences in PET. However, the spatial patterns do match that of the spatial patterns in net radiation across the site, which also exhibited a peak spatial autocorrelation at 50 m.

3.4 Discussion

3.4.1 Sensitivity Analysis

The results shown in Figure 2 and Table 1 clearly show that cumulative PET is more influenced by the amount of SGI that forms (SGI thickness) than how fast it melts. At a daily time step, there can be large decreases in PET during melt especially with higher melt rates. However, these decreases are balanced by the larger number of days when there is no SGI melting, resulting in little change in total PET for the month. Rather, the amount of SGI that forms is more influential to PET reduction, as this ultimately dictates how long the effect of melting SGI occurs. The SGI thicknesses used for the sensitivity analysis were based on observations from two ground temperature stations from the field. It is possible with thicker SGI formation, that reductions in SGI may become more pronounced. For this study, the maximum ice thickness was 58 cm in 2017 and 38 cm in 2018 as measured by frost probes. Over the period 2013-2018, using thermocouple data (Appendix A1 Table A4), Pauciflora exhibited ice thicknesses at the beginning of melt ranging from 0.12 - 0.26 m. These thicknesses appear to be closer to the 2018 frost probe measurements. However, this long-term data comes from a thermocouple profile in a single location, situated in a more open area, and may be more representative of the lower end of the ice thickness range entire study area. The maximum ice thickness in 2017 is more in line with those reported in the literature. FitzGibbon (1981) reported frozen ice layer thicknesses in a boreal fen that reached a maximum thickness of 0.7 m, with no ice separation present. Kingsbury & Moore (1987) found a similar ice thickness (0.57 m) for a sub-arctic fen, while more recently Smerdon & Mendoza (2010) reported freezing depths in a saturated floating mat boreal peatland up to 0.6 m. These studies provide some assurances that the sensitivity analysis is highlighting typical results for boreal peatlands.

It is also important to note that not all the SGI is being melted by energy supplied from the surface. Using the same thermocouple profiles, clearly some melting occurs from below, likely due to the warmer ground water below. At Pauciflora between 2012 and 2018, an average of 72% (± 13%) of the ice melted from above, while an average of 28% (± 13%) of the ice melted from

46

below (Appendix A1, Figure A4, Table A4). Thus, to increase the amount of SGI needed to affect the surface energy balance, ice thicknesses likely closer to a meter would need to occur. Such ice thickness values have not been observed at Pauciflora.

3.5.1 Controls on Ice Thickness

Both SGI thickness and melt rate exhibited spatial variability at both large and small spatial scales. For ice thickness, the spatial patterns at both smaller and larger scales are largely driven by surface characteristics that modify the surface energy balance over the winter such as proximity to trees and hill shading. At the large scale (50 m) ice thickness is intrinsically linked to the amount of shade received from the surrounding landscape over winter. The increased amount of shade along the western of the fen (Figure 3-3c) margin likely promoted cooler air temperatures, which caused a steeper temperature gradient at the peatland surface leading to deeper freezing (Jumikis, 1977). However, winter shading was not evident at the smaller scale, as there was no directionality in the ice thickness (spatial patterns were most pronounced at a scale of 1 m), but rather it appeared to be proximity to trees that controlled ice thickness. This is likely because at that small of a scale, the survey points are exposed to very similar shading dynamics from the hillslope, but very different snow depth due to variations in canopy cover. During the winter, tree wells can form in part due to snow interception leading to a general trend of increasing snow depth away from the tree (Figure 3-5a) (Sturm, 1992). Snow depth is a controlling factor on depth of freezing, where the low thermal conductivity of snow, combined with deep snow packs provides an insulating layer for the ground, drastically reducing the freezing rate (Moore, 1987; Zhang, 2005). Although snow depth was not directly measured at the same locations as the ice survey, visual observation confirmed the presence of tree wells at each surveyed tree prior to snow melt. It is also possible, that there were localized cooler temperatures closer to the tree due to shading, which would also cause deeper freezing. Sturm (1992) showed that these tree wells can act as energy loss windows across the landscape during the late winter. The results from this study support those finding as evidenced by the thicker ice around the trees, which means subsequently, that these thicker areas of ice could mean larger ground heat fluxes closer to trees, and reduced PET. The trees in the 2018 survey were located on hummocks or surrounded by hummocks <0.5 m from the tree. This may provide a benefit for the vascular vegetation and mosses on hummocks, by reducing water losses.

The effects of the trees were also observed at the larger scale, as proximity to trees also showed significant differences in the large-scale ice thickness patterns, where the more open areas

had thinner ice. However, the presence of a thin ice cluster at the large scale still correlated with a higher tree density (top thin cluster, Figure 3-3d), which suggests that the effect of trees on increasing ice thickness is secondary to the hill shading effects. Furthermore, tree densities were similar between thick and thin clusters where the average difference was only 0.03 m^2. The presence of this thin ice cluster despite the presence of trees could be due to proximity to the eastern hillslope, which only produced shadows during the morning hours. Compared to the thick clusters along the western hillslope, this would have left the ground more exposed to more incoming solar radiation and warmer temperatures over the winter. Such conditions could explain the thinner ice clusters along the eastern hillslope.

The controls on ice thickness spatial variability highlight the importance of tree proximity particularly at the small scale, and peatland orientation at the large scale. Depending on the orientation of the peatland and the surrounding topography, there will be different spatial patterns in different peatlands. For this study, the peatland is largely oriented along a north-south axis and is approximately 50 m wide. Changes to these variables, such as an east-west orientation, or a decrease in peatland width will alter the angles for incident solar radiation, changing shadow patterns and ultimately the thickness of ice. At the small scale, spatial variability may be reduced with increases or decreases in tree density and canopy closure. Forested peatlands may have a decrease in spatially variability SGI thickness due to less incoming energy reaching the ground surface. However, snow cover within forested areas can still exhibit spatial variability (Winkler & Moore, 2007; Woo & Steer, 1986) resulting in a likely tradeoff between tree density and the effects of incoming energy on SGI thickness. Conversely if there were no trees within the peatland, although the SGI might be thinner overall, it would still likely have lower spatial variability at the small scale. Any spatial variability in ice thickness under a completely open peatland would likely be due to large scale processes such as shading.

3.4.2 Controls on Melt Rate Spatial Variability

It is generally accepted in the literature that the presence of liquid water over ice will enhance melting (McClymont et al., 2013; Wright et al., 2009). However, results here show that for large scale melt patterns, the slower melt rate cluster at the larger scale had a higher median VMC (54%) compared to the faster melt rate cluster (19%). It is possible that this was due to incorporating both hummock and hollow values into the median, which often have large differences in near surface VMC values. However, between the faster and slower melt rate clusters,

there were no significant VMC differences between hollows or hummocks. This is likely due to the generally wet conditions found on site during the 2017 ice survey (Van Huizen et al., 2019). Spring hill shading, although significantly different between the two clusters, showed an opposite effect, where melt rates were higher under shadier conditions.

At the small scale, only SBS1 and SBS3 showed any spatial patterning. However, there may have been some effect from the individual tree itself. Both of these trees were ≈4 m in height and had shadows that would extend ≈ 3m out from the tree (Figure 3-5b), and the slower melt rates were on the northern sides of the tree while the faster melt rates were on the southern side of the tree. These findings also suggest that longwave radiation from the trees may not enhance SGI melt rate. Longwave emissions from the tree can enhance snowmelt, and the timing of snow free conditions (Pomeroy et al., 2003), which initiate the beginning of SGI melt. In permafrost environments this has been supported by observations where the depth to frost is deeper in areas that have been snow free longer (Carey & Woo, 2000; T. Zhang, 2005). This leads to the assumption that depth to SGI would increase at distances closer to the tree, and that melt rates may be faster due to long wave radiation from black spruce. Longwave radiation was not measured at our trees, however the findings from the 2018 ice surveys show that at the small scale, SGI melt rates were not higher. This suggests that longwave emissions from the trees may have a minimal effect on SGI melt rates, and that snow free conditions do not necessarily mean less ice. This could be because the SGI is insulated by the overlying moss and peat, at which point energy would have to be conducted down towards the SGI, and if the overlying layer has a higher proportion of air (i.e. the peat is drier) the thermal conductivity will be lower, leading to less energy available for melt.

However, although these results indicate a statistical difference between the melt rate clusters at small and large scales, when looking at the median difference in melt rate, and accounting for the sensitivity analysis findings, the differences in melt rate (1-3cm/day) would not make a functional difference in reducing PET. These findings further emphasize the greater importance of the amount of SGI that forms (i.e., thickness) versus how quickly it melts.

3.4.3 Spatial Variability in PET

The results from PET modelling (Figure 3-6a) show that the large-scale SGI spatial patterns did not impact the spatial variability of PET, instead, the patterns in PET matched that in Q* which generally increased from north to south within the study area. This pattern is likely due to the

variation in the tree canopy, where there is a higher tree density in the northern section compared to the southern section (Figure 3-3d). The narrowing of the hillslopes in the northern section also likely contribute to this reduction in Q^*. However, the magnitude of Q^* is bigger than QG, which means Q^* is driving available energy and subsequently PET.

SGI still acts as a constraint on PET though, reducing it across the site. The model was run a second time under ice free conditions (i.e., no melting SGI). PET within the thicker ice clusters showed an average decrease of 14 mm over May when factoring in melting SGI. This was greater than the 12 mm difference for the thinner ice clusters, reflecting the lower available energy consumption with thinner SGI, although the difference was not statistically significant (p value > 0.05, Wilcox). Based on these findings it can be concluded that the spatial variability of SGI does not need to be explicitly accounted for when modelling PET in this particular peatland

However, PET still exhibited differences across 100 m, which raises challenges in assessing not only cumulative PET at a site, but AET as well due to differences in Q^*. The differences observed here are likely due to the variation in the tree canopy, where there is a higher tree density in the northern section compared to the southern section (Figure 3-3d). The narrowing of the hillslopes in the northern section also likely contributed to this reduction in Q^* by increasing the shaded area of the peatland. It is also possible that differences in albedo could lead to changes in Q^*. Changes in albedo could be due to *Sphagnum* whitening due to desiccation, as well as leaf growth in the shrub layer. However, a study by Berglund & Mace, (1972) at a *Sphagnum* sedge bog in northern Minnesota showed that growing season albedo, averaged by space and time, varied from 11.6%-16.1%, a range of approximately 5%. Likewise, Thompson et al., (2015) reported a similar range in albedo values, averaged by space and time, over 20-25 % over the growing season, and no significant differences between albedo values for hummocks and hollows. Our PET and Q^* modelling was only for the month of May, when the peatland was still quite wet, where leaf-out occurred at the end of the month, and *Sphagnum* desiccation is restricted to a small number of hummocks.

If the footprint of the EC tower was situated in the area where there is greater Q^*, (i.e. the southern portion of the study area), site scale AET could be overestimated. Alternatively, site scale AET could be underestimated if much of the footprint was situated in the northern half of the study area (Figure 3-5a). This same caution holds true for measuring AET at the community or point scales, using chambers, lysimeters or porometry. When scaling up to site scale based on areal

50

weighting, not properly accounting for this spatial variability could introduce substantial error into the final numbers.

While this work suggests that SGI effects on PET can be represented in a model with a representative thermocouple profile, it may still be necessary to account for SGI spatial heterogeneity, depending on the model chosen. SGI can reduce peat volume changes (Petrone et al., 2008), especially in the upper moss layers, where the most significant volume changes occur (Waddington et al., 2010; Whittington & Price, 2006). A study in a boreal peatland by Nijp et al., (2019) showed that peat volume changes had similar largescale spatial autocorrelation (40.8 m) to the large scale spatial autocorrelation for ice thickness (30 m). Given the impact of SGI on peat volume changes, if the peatland model accounts for volume change (e.g. (Kennedy & Price, 2005; Nijp et al., 2017), the spatial heterogeneity of SGI may still need to be accounted for in the model.

This research shows that care must be taken when attempting to homogenize heterogeneous systems such as peatlands. Future peatland research needs to consider spatial variability, particularly if site scale models are going to be used and assess whether incorporating that spatial variability is necessary. While this study showed that spatial variability in ice does not influence spatial variability in PET, this is only one peatland. While future research should look to expand ice surveys like the ones conducted in this study the effects of SGI melt on evaporative fluxes should also be incorporated into cold regions hydrological models. The effects of SGI in WBP peatlands can then be evaluated under differing canopy conditions, peatland type (i.e., bog & fen), and climatic conditions.

3.5 Conclusions

The purpose of this study was to investigate the controls on SGI spatial variability to determine if SGI spatial variability translated into PET spatial variability. While the findings for this site showed that PET spatial variability was controlled by net radiation and not SGI, SGI still acted as a constraint on PET, helping to potentially reduce the overall amount of water leaving the peatland during the spring. This study highlights an important step when moving from field data to modelling. Spatial heterogeneity should be explored prior to modelling, to ensure that the model is using accurate representation of the field dataset. While spatial heterogeneity in SGI was not a factor in affecting PET, it remains unclear if it could be in other peatland systems. Furthermore, the spatial variability in PET highlights the need to make sure that when designing sampling plans

for peatland evapotranspiration, that care is taken to ensure the measurements are ultimately representative of the study area.

3.6 Acknowledgements

Chapter 4 : Assessing the importance of bi-directional melting when modeling boreal peatland freeze/thaw dynamics

4.1 Introduction

Seasonal ground ice (SGI) is a common feature in boreal peatlands (e.g. FitzGibbon, 1981; Friesen et al., 2021; Petrone et al., 2008; Price, 1987; Smerdon & Mendoza, 2010; Van Huizen et al., 2019) and has a large impact on the spring freshet, an important hydrological period within cold regions (W. L. Quinton et al., 2004; Zhao & Gray, 1997). SGI forms when the peatland ground surface temperature falls below the freezing mark (≈0°C). Fall saturated conditions, combined with the highly porous (0.8-0.96) moss and peat soils (Friesen et al., 2021; Petrone et al., 2008; Redding & Devito, 2005; Van Huizen & Petrone, 2020) lead to ice forming near the peatland surface that can range from 15-90 cm in thickness (e.g. Kingsbury & Moore, 1987; Smerdon & Mendoza, 2010; Van Huizen et al., 2019). This near-surface ice impedes water infiltration and drastically reduces the peatland subsurface water storage capacity (Price & FitzGibbon, 1987). During the subsequent spring, snowmelt can quickly exceed the limited storage capacity causing extensive spring flooding and large snowmelt losses from the peatland (Bowling et al., 2003; Woo, 2012). This results in the peatland acting as a source of water within the western boreal plain (WBP) landscape (Thompson et al., 2015).

Once the SGI has melted (here referring to the complete phase change of SGI) completely, or at least to a depth where its influence is negligible (Thompson et al., 2015; Van Huizen et al., 2019), infiltration can readily occur, filling the peatland storage capacity. This storing or conveying of water has large implications for the sub-humid climate of the western boreal plains (WBP)(Marshall et al., 1999), where peatlands can act as water sources for adjacent upland forests in undisturbed (Elmes & Price, 2019; Thompson et al., 2015) and fire disturbed landscapes (Depante et al., 2019), and convey water to downstream wetlands (Wells et al., 2017) contributing to their persistence (Hwang et al., 2018) in the dry WBP climate.

Integrating peatlands and their ecohydrological dynamics into larger scale climate models has received renewed focus (Helbig et al., 2020; Wania et al., 2009; Wu et al., 2016), owing to the impact peatland carbon and water fluxes have on climatic feedbacks (Drever et al., 2020; Gorham, 1991; Hayward & Clymo, 1982; Waddington et al., 2015) and their wide spatial coverage (Xu et al., 2018). As the climate changes, boreal peatland ecosystem function has been repeatedly highlighted as at risk of shifting (Helbig et al., 2020; Tarnocai, 2009; Vaughan et al., 2013;

Waddington et al., 2015; Zhang et al., 2019) due in part to the longer growing season brought on by a shorter duration of below-freezing air temperatures (Bush & Lemmen, 2019). Therefore, properly accounting for the freezing and melting of SGI in boreal peatlands will provide insight as to how climate change may impact these northern ecosystems. When modelling peatland ecohydrology, ensuring that SGI freeze/melt is accurately represented in peatland models allows for robust predictions in both peatland carbon and water fluxes. Not properly accounting for the unique role of SGI in peatlands can lead to erroneous estimation of surface runoff (Connon et al., 2015) and dissolved organic carbon concentrations (Davidson et al., 2019; Dyson et al., 2011). This is of particular importance given that the duration and timing of SGI melt is projected to diminish under a warming climate (Thompson et al., 2015)

The modelling of frozen ground has been studied extensively over the years (Lamontagne-Hallé et al., 2020) with models ranging from complex heat transport models such as SUTRA-Ice (e.g., McKenzie, et al., 2007), SHAW (e.g., Flerchinger & Saxton, 1989), and COUP (e.g., Jansson & Moon, 2001), to semi-empirical temperature index models (Kurylyk & Watanabe, 2013). The required level of model complexity is dependent on the research question being asked (Barbour & Krahn, 2004) and the physical processes that are being modelled (Lamontagne-Hallé et al., 2020). In the case of freeze/melt cycles in northern environments, including peatlands, focus is often directed on when the ground is frozen, versus when it is not (e.g. Carey & Woo, 2000; Davidson et al., 2019; Krogh et al., 2017; Patankar et al., 2015; Sutton & Price, 2020). As such, it is important to know the extent of SGI formation, specifically the depth to which SGI forms, and during melt, the depth below the surface, which dictates the peatland water storage capacity during the spring. Depth of freezing and melting can be modelled using the Stefan equation (Lunardini, 1981), which provides a relatively simple approach to modelling one-dimensional freeze and melt in one (top-down) (Krogh et al., 2017; Xie & Gough, 2013) and two directions (top -down, bottom-up)(Woo et al., 2004; Xie & Gough, 2013).While there have been extensive studies that measure freeze/melt in non-permafrost peatlands (e.g. FitzGibbon, 1981; Friesen et al., 2021; Kingsbury & Moore, 1987; McClymont et al., 2013; Moore, 1987; Petrone et al., 2008; Smerdon & Mendoza, 2010; Van Huizen et al., 2019), there has been very little work reported in the literature on freeze/melt modelling in peatlands (e.g. McKenzie, et al., 2007). While freeze/melt cycles have been represented in modelling studies, it is often not the focus of study, and validation of the freezing routines is often not explicitly discussed. Further, many of these studies take place in peatlands

underlain by permafrost(e.g., Krogh et al., 2017; Zhang et al., 2008), yet a large proportion of boreal peatlands are not underlain by permafrost (Tarnocai, 2009). In such systems, groundwater flow can still occur even while the peatland is frozen (Price & FitzGibbon, 1987), and melting during the spring can occur both from above and below. Kingsbury & Moore, (1987) reported a higher melt rate from below (4.1 mm/day) compared to melting from above (3.1 mm/day), while Chapter 3 reported that melting from below (bottom-up) comprised up to 1/3 of the total ice melting. Simple models like the Stefan equation can be adapted to employ bi-directional melt (Woo et al., 2004; Zhang et al., 2008) and be readily incorporated into soil-vegetation-atmosphere-transfer (SVAT) models. Given the potential importance of bi-directional melt in the timing of ice-free conditions, and the emerging need to include peatland-specific hydrological processes in hydrological models (e.g. Hwang et al., 2018), it is important to accurately model peatland SGI to understand how high latitude ecosystems may respond to warming.

Understanding how the timing of ice-free conditions may change under a warming climate can help mitigate some of the uncertainty of how the spring freshet may change (Thompson et al., 2015, 2017). However, not every peatland is the same, nor are peatlands internally homogeneous. Hydrophysical properties that determine water storage capacity such as porosity can vary with depth (Petrone et al., 2008; Van Huizen et al., 2019; Wells et al., 2017) and peat parent vegetation (Goetz & Price, 2015; McCarter & Price, 2014) and subsequently both between (Redding & Devito, 2005) and within boreal peatlands(Baird et al., 2016; Balliston & Price, 2020). Along with precipitation patterns, differences in porosity and water retention capacity will lead to differences in the absolute amount of antecedent soil moisture at the time of freezing. This quantity of moisture has a critical impact on the magnitude of ice formation over the winter due to the complex relationships between the volumetric heat capacity of water as it changes from liquid to solid, and subsequent changes in thermal conductivity (Hayashi et al., 2007; Oke, 1987) for the peat matrix (Ireson et al., 2013). The depth and volume of SGI formation will dictate the infiltrability of the peat soil following spring. Further, it is important to not only accurately model freeze/melt in a peatland but also to assess how hydrophysical properties and soil moisture may impact freezing. This will contribute to a better understanding of how the behaviour of SGI in boreal peatlands may change as the climate continues to warm, and what impact that will have on the spring freshet and the ecohydrological role of boreal peatlands.

Therefore, the objectives of this study are to: (1) Quantify the difference in the timing of ice-free conditions when modelling SGI melt with a unidirectional versus a bi-directional melt approach and assess the goodness of fit with both approaches; (2) Conduct a sensitivity analysis on the model to better understand how freeze/thaw cycle progresses under different soil moisture regimes and hydrophysical properties in peatlands.

4.2 Study Area and Methods

4.2.1 Study Area

Data used for this study were obtained at Pauciflora peatland (56° 22' 30.36" N, 111° 14' 3.29" W), a poor fen located on the Stoney Mountain complex, approximately 40 km south of Fort McMurray, Alberta, (Figure 4-1).
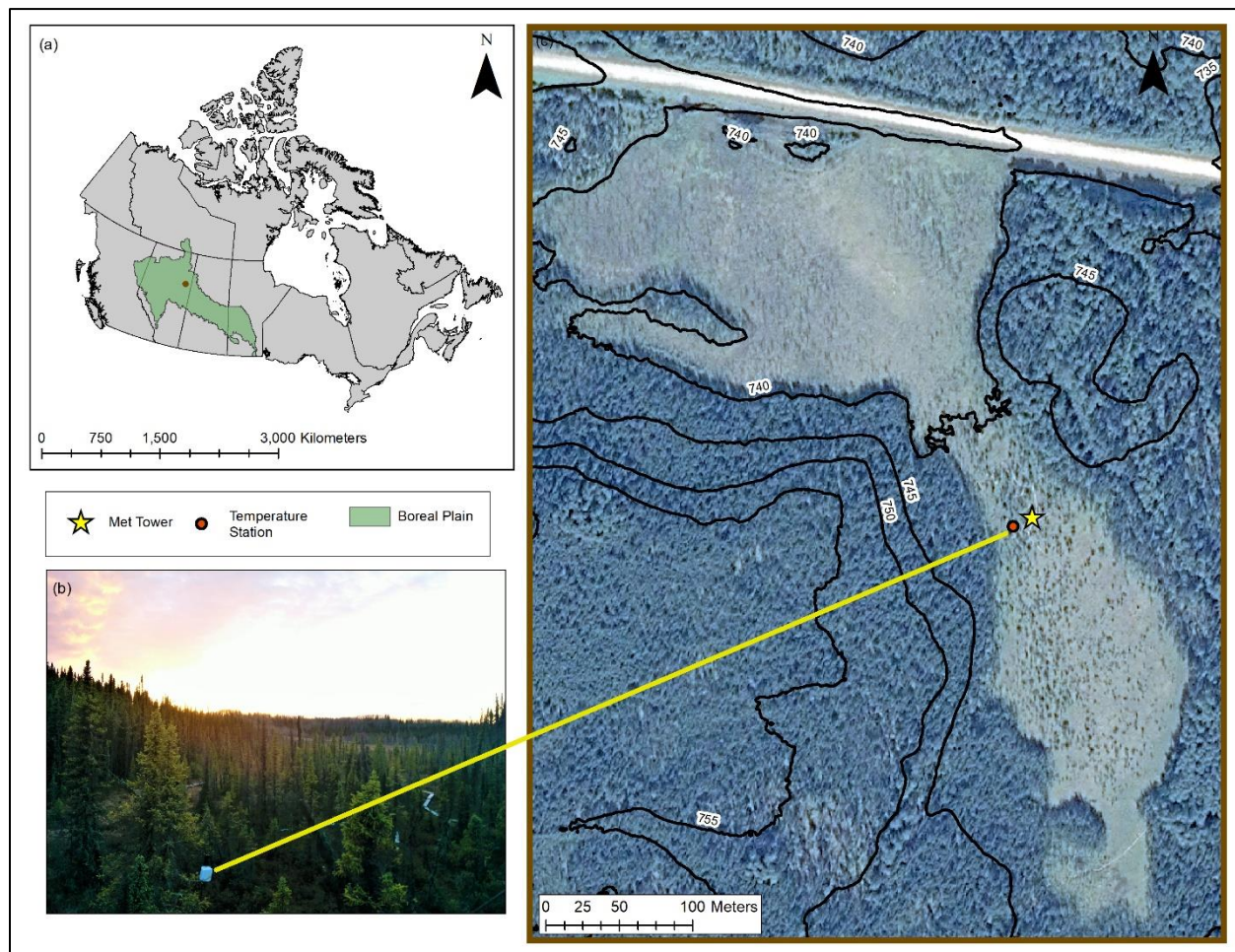
Figure 4-1 a) Location of site within Boreal Plain and Canada. (b) Image of location of thermocouple profile. (c) Map of relative location of met tower, thermocouple profile and soil moisture station. Yellow line points to the location of the thermocouple profile in (b) & (c). Contour interval is 5 m.

This peatland is located within the sub-humid climate of the Western Boreal Plain (WBP) where precipitation often exceeds potential evapotranspiration on an annual basis (Devito et al., 2005; Marshall et al., 1999). The 30-year climate normal (1981-2010) exhibits a mean annual air temperature of 1.0 °C, a mean rainfall of 316 mm (Fort McMurray Airport, Environment Canada) and a mean snow water equivalent of approximately 104 mm, calculated from an empirical relationship between snow density and air temperature (Hedstrom & Pomeroy, 1998). However, due to its elevated position (750 masl, ≈ 200 m above the surrounding area), Pauciflora receives approximately 100 mm more precipitation compared to the 30-year climate normal (Volik et al., 2020; C. Wells et al., 2017), and precipitation (4 year growing season average of 403 mm) often meets or surpasses potential evapotranspiration (4 year growing season average of 369 mm)(C. Wells et al., 2017).

Data for model parameterization were collected from the central part of the fen, corresponding to the "neck" part of the North fen in Wells et al. (2017) (Figure 4-1) where the peat depth averages 4 m. The understory vegetation is comprised of shrubs including *Ledum groenlandicum*, *Champadaphne calyculata, Rhododendron groenlandicum, Carex Aquatilis* and *Eriophorum spp.* and a carpet of *Sphagnum* mosses, primarily S. Angustifolium, but also including *S. capillifolium*, and *S. magellanicum*. Tree cover is comprised of relatively short, stunted *Picea Mariana* and *Larix Laricina* that occur in sporadic groupings. Hummocks, hollows, and lawn microtopographic features each comprise approximately 1/3 of the land cover in the study area. A ground temperature monitoring station was installed in an open Mid-Fen (MF) area. Subsurface temperatures were recorded at 2, 5, 10, 20, 50, 75, 100 and 150 cm below the ground surface in a hollow using Type-T thermocouples (Omega Engineering, Norwalk, Connecticut, USA). Data were measured using a Campbell Scientific logger (CR1000 Campbell Scientific Ltd., Logan, Utah) at a 60 second interval and averaged at 60 minutes intervals. Ground temperatures were then averaged daily. Any gaps smaller then 3 days were filled by linear interpolation. Gaps greater than 3 days were filled by averaging daily average ground temperature by day of year across 2012-2019 and using the average value corresponding to the day of year. From these ground temperature values, the position of the 0-degree isotherm (Carey & Woo, 2000) was interpolated and represents the observed position of the freezing/melting front.

A modified form of the Stefan equation (Jumikis, 1977; Kurylyk, 2015) for estimating freezing and melting was used,

57

$$z = \sqrt{\frac{2k_l I_l}{\lambda_f \omega_l \rho_l}}$$

(4-1)

where z is the Freezing/Melting Depth (m), k_l is the bulk soil thermal conductivity (W/m/°C), I_l is the freezing or (melting) index which represents the accumulated gain or loss of energy used in freezing or melting of SGI. It is calculated by summing the daily average ground surface temperature while above and below 0°C. λf is the latent heat of fusion of water (ice) (334 000 J/kg), ω_l is the water (ice) content for peat (equal to porosity), and ρ_l is the density of water (ice); 997 (kg/m^3). To employ a bi-directional melt routine, this equation was run separately for both the 2 cm (assumed surface) ground temperature (Temp$_{surface}$) and the 50 cm ground temperature (Temp$_{below}$) (see Figure B6 in Appendix B) to calculate two independent melting indices, where Temp$_{below}$ is referring to the temperature driving melt from below. The position of the 0-degree isotherm was determined first with the melting index calculated from Temp$_{surface}$, and then any upward thaw (upward shift in 0-degree isotherm) driven by Temp$_{below}$ was subtracted. However, during freezing a simplifying assumption was employed, whereby it was assumed that if Temp$_{surface}$ < Temp$_{below}$ then melting from below was considered negligible and ignored. Thus, bidirectional melting was implemented primarily during the spring thaw, and any brief mid-winter periods when the surface temperature increased above freezing. k was calculated using the following equation as outlined by (Farouki, 1981),

$$k = \prod_a k_a{}^{f_a}$$

(4-2)

using the individual thermal conductivities as listed in Woo & Xia, (1996) for peat/moss (0.25 W/m°C), air (0.025 W/m°C), water (0.57 W/m°C), and ice (2.20 W/m°C), where a refers to each soil component; k_a refers to each component thermal conductivity; and f refers to the fractional proportion of each component. The ω was assumed to be equal to porosity. For this particular peatland, the average porosity for the top 50 cm was determined to be 0.96 (Chapter 2). Due to data gaps in measured soil moisture (7.5 cm below ground surface) at the time of freeze up, the logged daily volumetric moisture content (VMC) was not used, and saturated conditions were assumed for the base model run (i.e. VMC=Porosity) for both bi-directional and unidirectional modelling approaches. VMC was also assumed constant for the duration of each model run. This

assumption was deemed to be adequate because varying soil moisture during the growing season does not impact the freeze/melt status, rather it is the soil moisture prior to freeze-up that is important. Furthermore, the site generally experiences high soil moisture close to or at saturation prior to freezing (Van Huizen et al., 2019). During the freezing process, frozen soil layers were assumed to have a residual liquid VMC of 0.15 Nagare et al., (2012) for the peat soil used in their study.

4.2.2 Model Performance, Sensitivity and Statistical Analysis

Model performance was assessed by comparing modelled freezing and melting depths to observed values, and calculating the root mean square error (RMSE), mean average error (MAE) and the relative time domain error (RTDE). For RMSE and MAE, the smaller the value the better the performance. For the RTDE, a value less than 1 indicates good model performance (Woo et al., 2004).

To conduct the sensitivity analysis, soil moisture, ground surface temperature, and peat porosity were all altered. Altering each of these provides insight into both potential climate change impacts (soil moisture and ground surface temperature) and variation in peatland hydrophysical properties (soil moisture and porosity). Each model run was completed using R statistical software (R Core Team 2018). To conduct the temperature sensitivity analysis, the average monthly ground temperature (°C) measured at 2 cm was calculated for each month across all years that ground temperature was recorded (October 29, 2012-July 24, 2019). For each temperature scenario, a percentage (starting at 10% and increasing to 70%) of each of monthly average was added to each daily average ground temperature as measured by $Temp_{surface}$ while holding porosity at 0.96 and saturation at 1(where all pore spaces are assumed to be filled with water). The 10-70% range used kept the adjusted temperatures within the expected range of temperature data under the different climate change scenarios used in Thompson et al., (2017). For the soil moisture scenarios, VMC was decreased by 10% each scenario, up to 50%. For the different porosity scenarios, the model was run with peat porosity values of 0.96, 0.9, 0.85 and 0.8, while saturation was assumed to be 1 and the ground temperature was set to the observed values. The effects of VMC and porosity are likely to be similar, owing to the control of porosity has on the total volume of water present in the soil. However, they were both included because VMC elucidates the role of changing water content, while porosity elucidates the role of changing peat physical structure on the formation of ice. Sensitivity was determined by comparing percentage change in maximum frost depth from the

base model run and conducting a multiple linear regression to assess the most influential variable to maximum frost depth.

To assess the impact of climate on timing of ice-free conditions, average ground temperatures for the month of May (when the snow has already melted and when ice free conditions typically occur) were compared to modelled mean ground temperature in the month of May under 13 different climate scenarios, which were run from 2011-2090. For a detailed overview of these scenarios, we refer the reader to Thompson et al., (2017). An overview of how modelled ground temperatures were calculated can be found in Appendix B.

4.3 Results

4.3.1 Freezing & Melting Depth Model Performance

The results from both the unidirectional approach (UNI), where melt came from the top-down, and a bidirectional approach (BI) where melting occurred from above and below, are shown below in Figure 4-2. Hashed lines represent the modeled, and solid lines represent the observed data. In general, there is good agreement between modeled and observed freezing depth for both UNI and BI, with BI having a slightly better root mean square error (RMSE) based on all years (5.3 cm) compared to UNI (RMSE = 7.6 cm). Some years appear to have a better fit than others (2012-2013 vs 2016-2017 in Figure 4-2). However, in general RMSE, mean average error (MAE) and Relative Time Domain Error (RTDE) were very similar for freezing depth under both modelling approaches (Table 4-1), but the bi-directional approach did show a slightly better fit overall (r^2 of 0.80) compared to UNI (r^2 of 0.65) (Figure 4-3).

Table 4-1 Model Fit. The top two rows show Root Mean Square Error and Mean Average Error for the entire dataset. Relative Time Domain Error is a metric used by Woo et al., (2004). The middle two rows show the number of days different between modelled and observed ice free conditions for each model run for each year, while the bottom two rows show the average and standard deviation (n=7).

Model	RMSE Freezing Depth (m)	MAE Freezing Depth (m)	RMSE Melting Depth (m)	MAE Melting Depth (m)	RTDE	RTDE Wet Tundra (Woo, 2004	
Uni	0.077	0.048	0.042	0.023	0.66	0.55	
Bi	0.054	0.035	0.027	0.018	0.50	0.19	
Ice Free Date Difference for Each Year (Days)							
Model	2012-2013	2013-2014	2014-2015	2015-2016	2016-2017	2017-2018	2018-2019
Uni	7	7	8	13	1	13	14
Bi	3	-2	2	5	-6	7	2
Model	**Average Ice Free Date Absolute Difference (Days)**						
Uni	9.0 ± 4.7						
Bi	3.9 ±2.1						

Figure 4-2 Uni (Upper) and Bi (Lower) Modelled and Observed Freezing and Thawing Depths. Note the improvement in fit in 2017–2018, 2018–2019 between the UNI and BI approaches. The constant offset between observed and modelled thawing is because the observed temperature is measured at 2 cm, but it is assumed to be representative of the surface temperature.
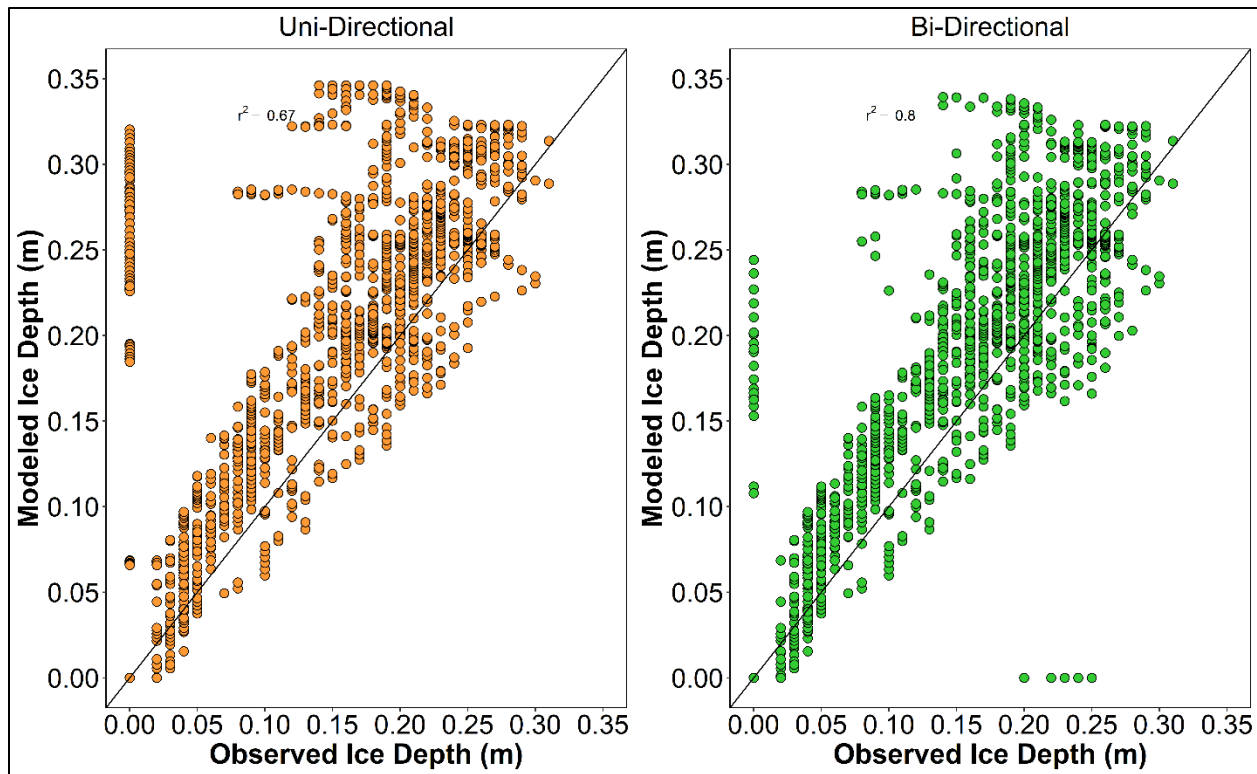
Figure 4-3 Uni Directional and Bi-Directional modelled ice depth vs observed ice depth. The black line represents the 1:1 line. Points above the model line indicate overestimation, and points below the line indicate model underestimation.

While overall fit did not appear to vary much between BI and UNI, accurate modelling of bi-directional melt and estimation of the timing of ice-free conditions did improve (Table 4-1). This is evident in the model years of 2017-2018 and 2018-2019. Substantial melting from below can be seen in the observed data (decreasing depth of the freezing depth with time during April and May). UNI model runs do not capture this, and ice-free conditions are dependent on the melting front meeting the freezing front at much deeper depths. BI model runs do capture this bidirectional melt, where a clear decrease in the freezing front occurs approximately in line with the observed decline. Using the BI model improved the average estimation of ice-free conditions by just under a week (absolute difference of 5.1 days).

There was a similar model performance for melting depth (orange lines, Figure 4-2). BI scenarios performed slightly better (RMSE =2.7 cm) compared to the UNI scenario in RMSE (2.7 cm vs 4.2 cm) and MAE (1.8 cm vs 2.3 cm). However, the r^2 were much lower (BI = 0.26, UNI = 0.10) compared to the modelled freezing depths, due to difference in the observed ground surface temperature being measured at 2 cm.

63
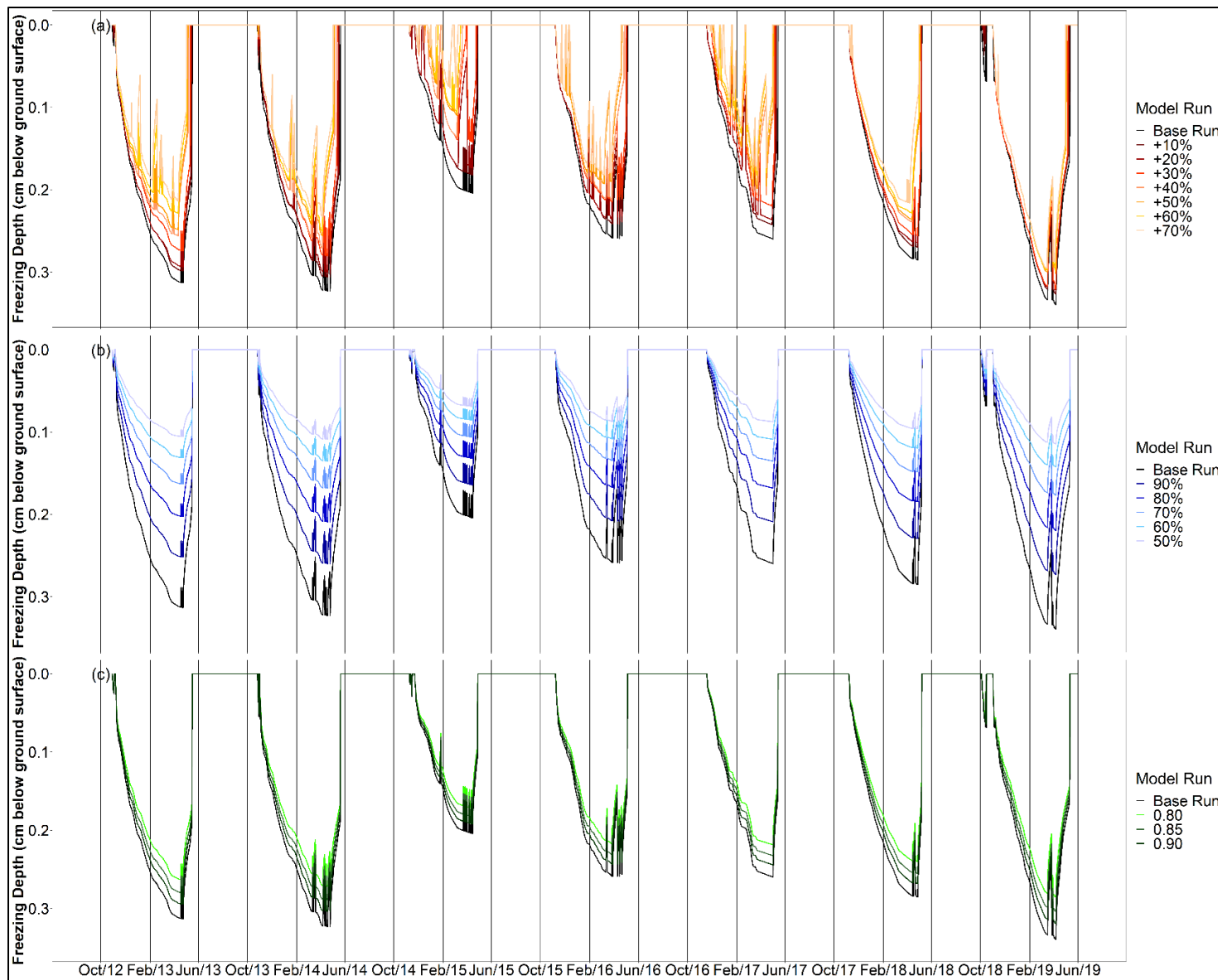
Figure 4-4 Time series for Sensitivity Analysis. Note, that these were completed using a Bi-directional approach.
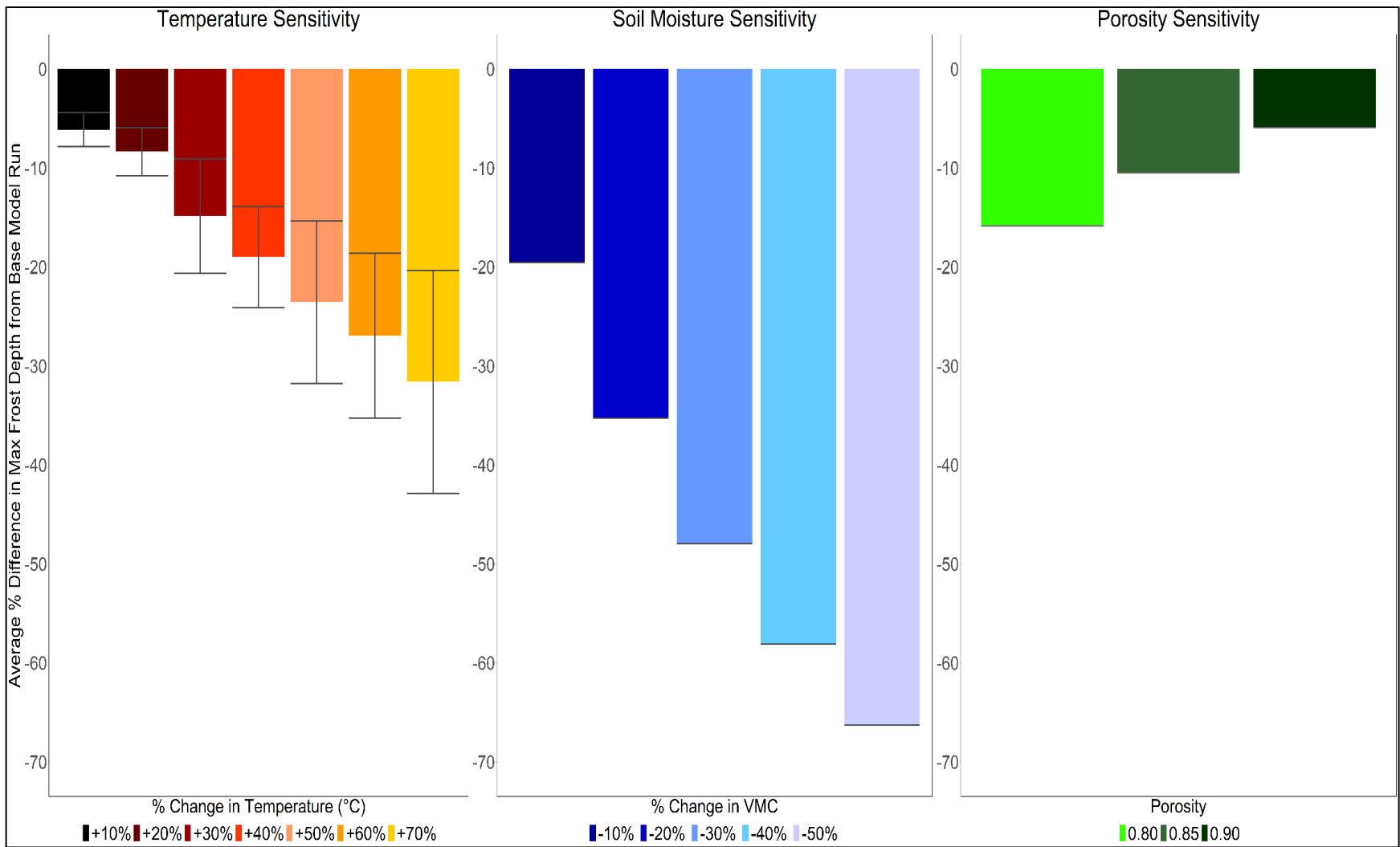
Figure 4-5 Percentage change in Maximum frost depth, compared to the base model. Vertical Error Bars are the 95% confidence intervals. Note that the 95 % confidence intervals for VMC and Porosity are $< 10^{-15}$.
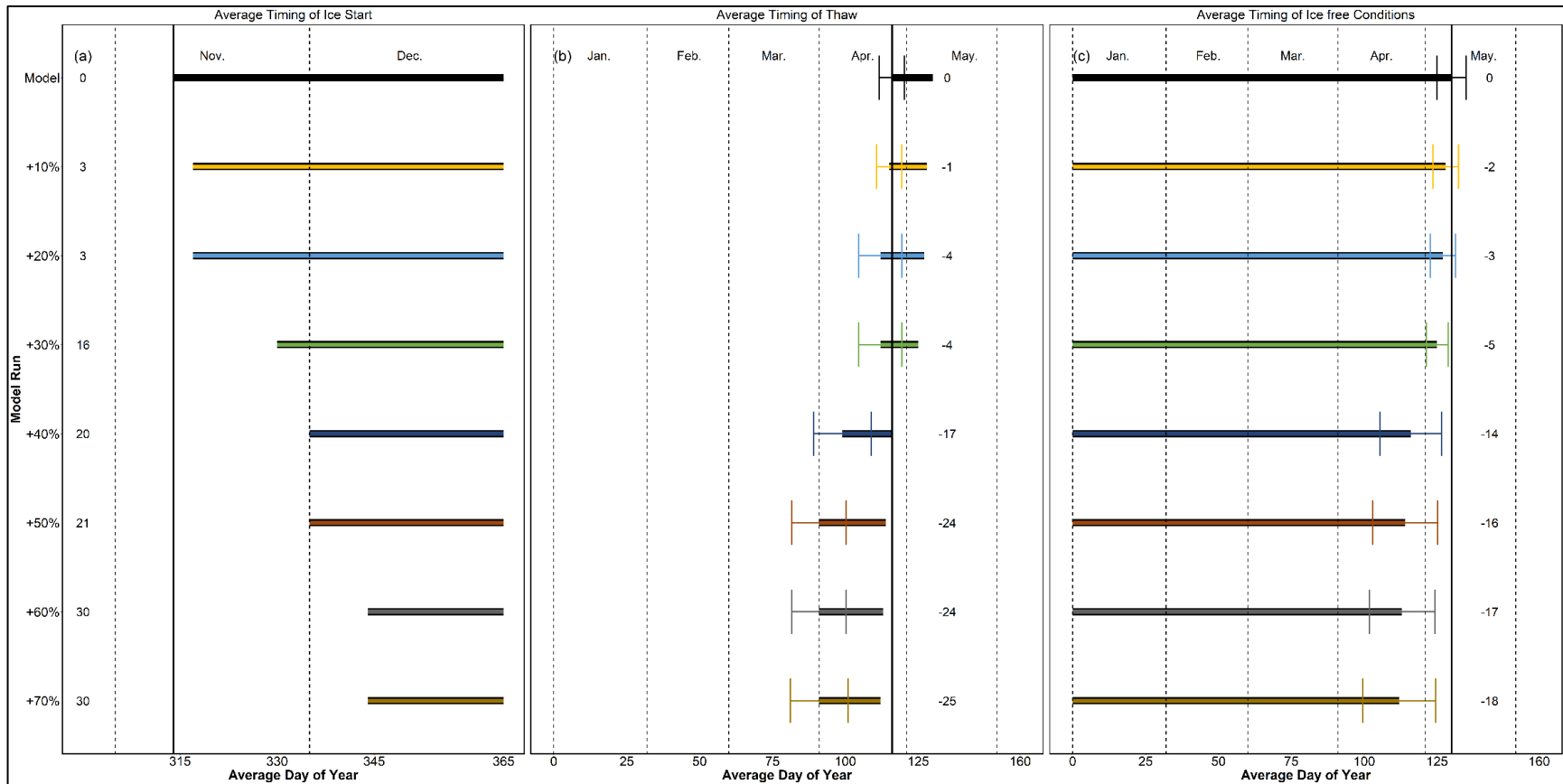
Figure 4-6 Average Day of Year where the beginning of freeze-up, timing of thaw, and ice free conditions occur. (a) Timing of Ice Start. (b) Timing of Thaw (c) Timing of Ice Free Conditions. Error bars represent the 95% confidence intervals which are not shown for panel (a) for clarity but listed here; Base ± 5 days, +10% ±9 days, +20% ±9 days, +30% ±20 days, +40% ±21 days, +50% ±21 days, +60% ±29 days, +70% ±29 days. Average is based on the 7 freeze thaw seasons: 2012–2013, 2013–2014, 2014–2015, 2015–2016, 2016–2017, 2017–2018, 2018–2019.
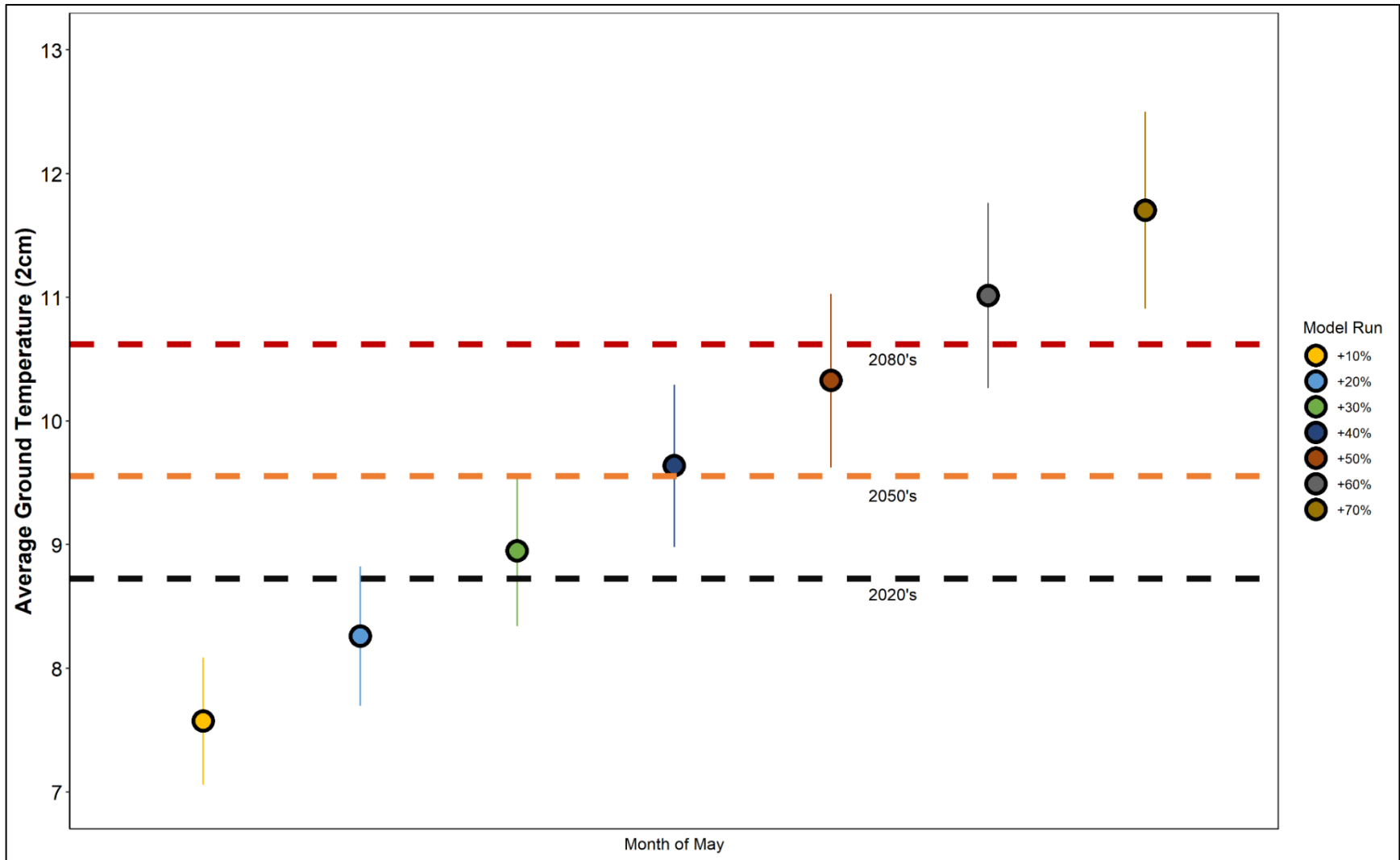
Figure 4-7 Comparison of Mean May ground temperature for each temperature sensitivity run. Points are offset for visibility. For complete graph of data, refer to Supplementary Material Fig. A3. Dashed horizontal lines represent the mean may ground temperature for the climate projections. Vertical lines represent the 95% confidence intervals.

4.3.2 Model Sensitivity to Porosity, Soil Moisture, and Ground Temperature

The results from the sensitivity analysis (Figure 4-4a,b,c) showed that all three parameters play a significant role in controlling the depth of freezing. The multiple linear regression showed that all three coefficients are significant (p value <0.05) (Appendix B, Table B1). While each parameter was significant there were differences in the parameters relative impact on freezing depth. Changes in the variables were meant to reflect potential changes that could be seen in the field. Therefore, for an expected range in VMC, there were bigger changes in max freezing depth compared to reasonable changes in porosity. This is shown clearly in Figure 4-5 (center panel) where a decline in soil moisture up to 50% resulted in a decline of 66% in maximum ice depth. This was double the + 70% ground surface temperature scenario, which resulted in a decline of 30%. Porosity appeared to have the smallest impact, where a porosity of 0.8 only led to a 14% decline in maximum ice depth.

4.3.3 Sensitivity to a warming climate

Figure 4-6 illustrates the average difference in the day of year for the timing of ice-free conditions, melt and freeze up for each temperature scenario. Warmer ground surface temperatures lead to later starts for ice freeze up, from 1 day earlier to as much as 30 days (Figure 4-6c). This corresponds to a potential shift in the initiation of freezing conditions by as much as a month, where freeze up typically began in November under base model conditions, this shifted to early December under the warmest scenario (+ 70%). Conversely, the timing of melt shifted from 1 day earlier, up to 25 days earlier on average (Figure 4-6b), meaning a shift in the beginning of melt from May to the beginning of April. Consequently, there is a shift in the timing of ice-free conditions, ranging from on average 2 to 18 days earlier (Figure 4-6 c).

Of note, is a consistent shift in the earlier (later) timing of melt (freeze up), and ice-free conditions that occurs between the +30% and +40% temperature scenarios, which coincide with the largest increase in the average number of days where ground temperatures are >0°C (Appendix B Figure B5). Between +30% and +40%, the average increases by 12 days, compared to the average increases between the other temperature scenarios which are <=8 days. These results indicate that a large shift in the modelling of frozen conditions is occurring between the +30% and +40% modelling scenario.

To contextualize these results within a changing climate, the mean 2 cm temperature (representing the ground surface temperature) for the month of May for each temperature

sensitivity analysis run was plotted against the average modelled ground surface temperature for the month of May under a warming climate in the Western Boreal Plains (Thompson et al., 2017). Except for the + 10% and +70% runs, each sensitivity run falls within the range of one of the climate change scenarios (horizontal dashed lines). These results suggest that by the end of the 2020s there could be a shift in the timing of ice-free conditions by approximately 3-5 days. By the 2050s this increases to approximately 17 days, and by the 2080s, the timing of ice-free conditions may shift by as much as a month earlier (i.e. May to April).

4.4 Discussion

4.4.1 Model Performance and the need for Bi-directional Melt

Incorporating bi-directional melt led to marginal increases in model performance when assessing freezing depth. This could be due to the relative importance of melting from below. In Figure 4-2, the observed freezing depth (solid blue line) shows that bi-directional melt is not always an important process. While there is clear melting from below occurring in the 2014-2015, 2015-2016, 2017-2018 and 2018-2019 ice seasons, it is less clear if there is any significant melting from below in the 2012-2013, 2013-2014, and 2016-2017. For melting from below to occur, enough energy needs to be supplied to the bottom of the ice layer from the warmer groundwater, to overcome the rate of energy loss from the freezing front up the ice to the surface (Mohammed et al., 2018). The high thermal conductivity of the ice-dominated peat matrix (1.6 W/m°C while frozen, 0.55 W/m°C while unfrozen) in our study, means that melting from below is unlikely to occur during the winter, where steep energy gradients between the ground surface and the cooler air above mean that the ground is losing energy. Of course, with a snowpack present, maintaining the ground surface at near-freezing temperatures (Friesen et al., 2021), it is possible these energy gradients could reverse allowing for some melting from below to occur during the winter. There are some periods (Figure 4-2), where melting from below is possibly occurring during the winter months (Dec-March) in each of the years. However, it is difficult to determine what is actual melt from below, and what might be "noise" introduced by the thermocouple on a daily time scale. Similar model performance between BI and UNI may also be due to significant bi-directional melt not occurring until the spring melt season, which, on average is a relatively short time frame (average 15±1 days) compared to the length of the entire ice season (average 181±8 days). Indeed, when analyzing model fit for just the spring season, the difference in UNI and BI model runs, stays similar to the model fit for the entire season (see Table 1), as both UNI and BI have improved

model fit during the spring (BI: r^2 0.80, RMSE 0.054 m, MAE 0.035 cm, UNI: r^2 0.67, RMSE 0.077 m, MAE 0.048 m) compared to the model fit for the entire season (Table 1). Therefore, both models can accurately simulate freezing depth for most of the winter months, and it is only when melting from below is occurring that the two models begin to deviate in their performance.

Model fit of freezing depth for both the BI and UNI models were consistent with similar studies that used the Stefan equation. Woo et al. (2004) reported an RTDE of 0.55 and 0.19 for UNI and BI respectively (Table 1). However, their "Wet Tundra" site had relatively low peat porosity (0.8) for the top 20 cm compared to Pauciflora (0.96). While our UNI model run RTDE was like Woo et al. (2004), our model performance did not exhibit as big an improvement in RTDE between both model-run approaches. It is possible these differences could be due to the single soil layer for the model that was employed in our study, compared to the multi-layered soil used in theirs. While it does not occur consistently in every year, there does appear to be a general deviation between the modelled and observed data that occurs in the 15-20 cm depth below surface (see Figure 4-2; 2013-2014, 2014-2015,2017-2018). The average porosity value of 0.96 is less representative of the lower 20 cm of the 0-50 cm model domain. Another possible reason is because the Stefan Equation assumes that the sensible heat required to change the ground temperature is negligible (Kurylyk & Hayashi, 2016), although the favourable model performance suggests that this impact is relatively small. Finally, it is also possible that Woo et al (2004) found a greater improvement in model fit because there was more bi-directional melt occurring at their more northern location (69°08'N 148°51'W). Although for that to occur, there would need to be talik development to provide a thawed layer (Devoie & Connon, 2019) beneath the frozen layer. Similar model performance was also shown when comparing to peatlands in other permafrost environments. Xie & Gough (2013) showed that the Stefan equation produced a model error of 5-10 cm, while Krough et al. (2017) report a model difference of 4 cm for summer melt depth, although the model performance was poorer for freezing depth (difference of 15 cm). While evaluating several different freeze/thaw algorithms, Zhang et al., (2008) found a model error of 12-14cm for a permafrost peatland when using a bi-directional Stefan's equation. However, they also concluded that unless the original assumptions of the Stefan's equation are met (i.e., wet homogenous soil conditions), that the Stefan's equation is not suitable compared to using more computationally intensive numerical models. For peatlands though, wet homogenous soil conditions are generally present. These results suggest that the Stefan Equation is a suitable, and

simple model for estimating the general trends of freezing depth in boreal peatlands. Furthermore, with climate change leading to talik development (Connon et al., 2018), the prevalence of bi-directional melt in the active layer of permafrost peatlands may become more important. The relative ease with which to measure the surface temperature in a peatland also means establishing the driving data for the equation is less intensive compared to other approaches such as the n-factor (Kurylyk & Watanabe, 2013).

Where the BI model run outperformed the UNI model run is specifically the timing of ice-free conditions (3.9 vs 9 days). Almost a weeklong discrepancy in the timing of ice-free conditions can lead to erroneous model results. For example, if a model shows that the ground is still frozen, despite being unfrozen in reality, and a large precipitation event occurs, there will likely be significant runoff when compared to observed data. Of course, there are ways of mitigating this by modelling infiltration into frozen soils (e.g. Granger et al., 1984; Gray et al., 2001; Hayashi, 2013; Mohammed et al., 2018). However, many of these approaches rely on the assumption that unfrozen, unsaturated macropores are present in the soil allowing for preferential flow paths. While this is likely to be true in mineral soils, preferential flow is less likely to occur in peatlands, especially when there are high antecedent moisture conditions prior to freezing. Rather, as the SGI melts away, large unfrozen areas form within the peatland, allowing for infiltration. Barring a spatially distributed freeze/thaw model, it is important to have a representative approximation of the frozen status of a peatland. Consequently, when modelling frozen peatlands, it is likely more important to capture the timing of ice-free conditions, rather than some intermediate state. Bi-directional melt can enhance the spring melt, which is due not only to the relatively warmer groundwater underneath, but as the SGI melts it begins to form holes (Van Huizen et al., 2019). These holes increase the surface area of the SGI, exposing more of it to warmer air temperatures from above, but also likely inducing lateral melting as the SGI becomes fully surrounded by an unfrozen, saturated peat matrix. Lateral melting has been suggested as being more important when thicker ice is present, where the vertical heat inputs are not sufficient to melt all of the ice present (Kurylyk et al., 2016). In Kurylyk et al., (2016) their permafrost was reported to be 9 m ± 3 m. The frozen layer at Pauciflora, was between 30-40 cm, much thinner compared to the 900 cm reported above, suggesting that the relatively thinner ice at Pauciflora could be melted primarily from vertical energy inputs. The generally good agreement between

observed and modelled values (Figure 4-2, Table 4-1) suggests that lateral melt is likely less influential for the thinner SGI found at Pauciflora.

This study took place in a poor fen, where groundwater inputs from the surrounding hillslopes occur quite regularly. There is uncertainty if bi-directional melt is as important in a bog, where groundwater inputs from adjacent mineral uplands do not occur. However, there is lateral groundwater movement that can occur within a bog especially if there is a dome present (McKenzie et al., 2007). While warmer pulses of groundwater from upward hydraulic gradients may not occur, this internal, horizontal flow of water may enhance bi-directional melt. Due to the dependence on precipitation for water, a bog could experience water table decline over the winter. This can lead to a decoupling between the water table and SGI layer, further limiting melting from below. Decoupling of the SGI and water table could also occur due to frost heave (Moore, 1987). Future work is needed to characterize the differences between SGI freeze/thaw in bogs and fens.

4.4.2 Model Sensitivity: what is the most important to parameterize accurately?

Results (Figure 4-6 and Appendix B, Table B1) demonstrate that VMC was the most significant controlling factor on freezing depth, which can be attributed to the thermal conductivity of water when it is in a frozen (2.2 W/m°C) and liquid state (0.57 W/m°C). When saturated and frozen, the bulk soil thermal conductivity was greater by a factor of 2 (1.65 W/m°C) compared to unfrozen (0.55 W/m°C), a difference of 1.1 W/m°C. This shift in thermal conductivity, which controls the rate at which energy is transferred upwards from the freezing front through the soil during freezing, is what causes freezing depth to be most sensitive to soil moisture. As such, when modelling freeze/thaw in peatlands, it is important to accurately measure soil moisture prior to freezing. For our study soil moisture was not directly measured. However, Pauciflora is a relatively wet site, owed to its local climate (Wells et al., 2017), and given the good base model performance (RMSE = 5.4 cm), our assumption of saturated conditions prior to freezing appears to be reasonable. This presents a challenge for using field-based data for modelling peatlands though, as there is uncertainty around the accuracy of typical soil moisture measurement methods during frozen conditions, and pressure transducers for logging water table measurements seldom function properly under freezing conditions. For the purposes of this modelling experiment, once freezing was initiated, the amount of soil moisture present in the top 50 cm of the peat column was not allowed to change, only the relative proportions of liquid and frozen water changed (i.e., moisture migration was not explicitly modelled). Upward vapor flux in a frozen soil has been shown to vary

from 1-30mm/winter season (Santeford, 1978; Woo, 1982) in peatlands, while Kingsbury & Moore (1987) suggested it as a possible mechanism for the development of a partially dehydrated frozen peat layer at depth. However, for Pauciflora, given the likelihood of saturated conditions prior to freeze-up, and the presence of SGI at the surface prior to spring melt, it is assumed that moisture migration had a negligible impact on the freezing characteristics in this study. Once a portion of the soil was frozen, it was assumed that a small amount of liquid VMC (15%) remained (Nagare et al., 2012), adsorbed to the peat fibres (Farouki, 1981). This unfrozen water content can also vary, depending on the soil type and subsurface temperature. However, based on the typical ranges of liquid VMC in a frozen soil (0.01-0.3) (Ireson et al., 2013), the thermal conductivity range is likely to be relatively small (0.64 W/m°C) in the highly porous upper soil layers.

Ground surface temperature had the second biggest impact on freezing depth, after VMC. Its relatively lower impact compared to VMC is likely because ground surface temperature is more important for initiating the freezing conditions, while VMC, due to its disproportionate impact on thermal conductivity, has a bigger influence over freezing depth. Changes in porosity had the smallest impact on freezing depth, due to the small, range of porosity values used in the sensitivity analysis (0.8-0.98) for the modelled soil layer. This range is representative of the top 50 cm of the moss and peat in most peatlands. Typical freezing depths extend from the first few cm to 50 cm depth, which can however, cover a range of porosities. For Pauciflora, the highly fibric moss and peat extended down through the top 50 cm. However, based on the sensitivity results, freezing rates could vary, likely slowing with depth, as a lower porosity means a lower water holding capacity under saturated conditions, and subsequently lower thermal conductivity. Of course, less porous peat soil does not necessarily mean shallower freezing depths. Water has a high heat capacity (4.180 MJ/(m^{3}C)) meaning less water present in the soil means less energy is needed to increase or decrease the temperature above/below the freezing point. If a highly porous peat soil has a lower VMC prior to freeze up, then more air will be present at the time of freezing. This can lower the thermal conductivity leading to potentially shallow freezing, yet the decrease in heat capacity could also lead to more rapid ground surface temperature swings. However, with the presence of a snowpack it is likely these rapid changes occur over a short period at the beginning of the winter, as the snowpack likely insulates the ground from any further rapid ground surface temperature changes (Kingsbury & Moore, 1987). Furthermore, the model used here does not account for heat capacity, and our model domain treats the soil as one layer, making the modelling

of a discrete layer of saturated unfrozen peat over frozen saturated peat difficult to assess. However, results from Wright et al. (2009) would seem to suggest that the heat capacity of unfrozen water might not be as important as its higher thermal conductivity during the spring thaw where unfrozen liquid water in the peat matrix above the frozen layer led to faster melt rates. This is also likely due to the lower heat capacity (1.9 MJ/(m^{3}C)) of ice. In the winter, this could mean that freezing rates are initially slower, under saturated conditions, and it is not until enough ice forms, increasing the thermal conductivity, that ice formation can speed up. Another complicating factor is that if there are unsaturated conditions prior to SGI formation, moisture migration, or early winter snowmelt could fill up the remaining storage capacity (Appels et al., 2018; Redding & Devito, 2011; Woo & Heron, 1981), leading to saturated conditions as freezing begins. The probability of this occurring will likely increase as well with more frequent mid-winter departures above the freezing point over the growing season. Finally, the zero-curtain effect (Outcalt et al., 1990) has been shown to delay temperatures rising above the freezing mark in peatlands during the spring (McKenzie, Siegel, et al., 2007), where the peat soil can be iso-thermal for up to a month or more during the spring thaw. While there was some evidence of iso-thermal soil conditions in the top 20cm at Pauciflora, this typically coincided with a ripening snowpack, meaning the peatland surface was predominantly covered by snow. Ground thaw and melting of SGI typically does not occur until the snow has disappeared. This likely means the zero-curtain effect had little impact on the melt rates and timing of ice-free conditions at Pauciflora.

4.4.3 Implications for a shifting SGI regime in boreal peatlands

The results from the climate sensitivity analysis, show a clear shift towards earlier ice-free conditions (Figures 4-6 & 4-7). By 2030, the apparent threshold response between the 30% and 40% sensitivity runs may occur, resulting in a shift of ice-free conditions by approximately a week on average, and up to two weeks. By the end of the century, ice-free conditions could occur up to a month earlier. These results are generally in line with climate predictions for the boreal forest, which suggest warmer air temperatures, and earlier onset of spring conditions (Buermann et al., 2013; DeBeer et al., 2020; Price et al., 2013). These may be conservative estimates of the timing of ice-free conditions though, as the sensitivity analysis did not account for shifts in precipitation patterns, or increased rain on snow events, the latter of which is expected to increase (Zhang et al., 2019). An increase in rain on snow events could enhance melting, as precipitation provides additional heat inputs both into the snow pack and any exposed ground (Woo & Xia, 1996),

potentially leading to even earlier melt compared to the results of the climate sensitivity analysis. In addition to uncertainty in the estimates due to precipitation, soil moisture conditions are expected to be drier for the boreal forest (Wang et al., 2014) due to the increase in air temperatures, longer growing season and subsequently higher evapotranspiration rates (Helbig et al., 2020). It is possible that SGI freezing depth may increase, as the depth is strongly controlled by snowpack thickness (Friesen et al., 2021; Iwata et al., 2010), although this effect could be mitigated by lower antecedent moisture conditions prior to freeze-up. Our sensitivity analysis implicitly assumes that the timing of snowfall stays the same for each model run. As precipitation regimes shift, it is possible that there could be slight increases in freezing depth in the short term. Under a warming climate, Bi-directional melt may also increase. In the warmer scenarios, there was an increase in the number of freeze/thaw events (data not shown), where melting from below became more frequent, as there were more days where the surface temperature was above 0°C. This highlights the potential importance of characterizing melt from below when modelling freeze/thaw in future model studies.

Interesting to note however, is that while shifts in soil moisture resulted in different freezing depths, timing of ice-free conditions did not change. This is likely due to the proportional changes in thermal conductivity associated with changes in VMC (Appendix B, Figure B4) where there is less ice to melt, energy transfer is less efficient and there is a lower melt rate. It is possible with this scenario of decreased melt rates, that spring evapotranspiration rates could increase, as less energy is allocated to melting ice, and could increase potential evaporation rates (Chapter 2). This may also lead to more desiccation, as a slower melt rate could be outpaced by evapotranspiration rates (Moore, 1987). This increased drying may increase fire risk for peatlands due to a decrease in the near-surface soil moisture of the upper moss layer (Shetler et al., 2008). However, this increased fire risk may also depend on the relative proportion of hummocks and hollows that form in peatlands, as hummocks are typically thought to be more resistant to burning owing to their capacity to maintain higher water content during droughts (Thompson & Waddington, 2013). Also, SGI can melt at different rates across a peatland (Chapter 3). While results from Chapter 3 showed that these spatial differences were quite small, it is possible that evaporation rates could outpace melt rates in one area of the peatland compared to another.

A similar pattern to the VMC and the timing of ice-free conditions is seen with porosity as well, where the timing of melt and ice-free conditions stays the same, despite the changes in the

amount of ice that formed. This suggests that despite potential differences in upper-level soil porosities between bogs and fens, any differences in freeze/thaw conditions between peatlands will be largely climate driven.

These similarities in the timing of ice-free conditions, despite differences in porosity and VMC imply that the thickness of ice (i.e. the amount of ice that forms), while consequential for the spring surface energy balance (e.g. Chapter 3), may not be as integral when modelling the timing of ice-free conditions. As for the role of SGI in boreal peatlands, the thinning of SGI, combined with the earlier timing of ice-free conditions, suggests that boreal peatlands may become less reliable sources of water on the landscape, particularly during the spring freshet, or at the very least, there will be increased variability in the magnitude of the spring freshet.

4.5 Conclusion

This work builds upon the conclusions of Woo et al., (2004), which demonstrated that including bi-directional melt in peatland hydrological models is important to ensure proper modelling of the timing of ice-free conditions. Using the Stefan Equation to achieve this, provides a relatively simple model that should be easily integrated into soil-vegetation-atmosphere-transfer (SVAT) models. However, more work is needed to better understand if there are any differences in SGI freeze/melt cycles between peatland types, and if its relative impact on the spring freshet may change with hydrogeomorphic setting of the peatland. Furthermore, this work highlights the importance of conceptualizing what is to be considered as "ice free" when modelling peatland freeze/thaw. Does it occur when all the ice is gone? Or is there a functional definition for "ice-free" where the impact of SGI on infiltration and other hydrological processes is negligible, despite the presence of some SGI? Finally, as the climate warms, the timing of ice-free conditions will shift earlier in the season, by as much as 1 month earlier by the end of century. This could mean that a peatlands role in the landscape may change. Spring discharge may become more variable especially for headwater catchments, and less water could leave these peatlands during the spring. In addition to shifts in the peatlands hydrological role within the landscape, a reduction in SGI may result in an increased shift in peatland vulnerability to spring fires, where increased desiccation, due to slower melt rates combined with increased evaporation rates could lead to higher water losses from the living moss layer. Future research is needed to investigate this potential positive feedback that could increase peatland fire risk and subsequent carbon losses.

4.6 Acknowledgements

Chapter 5 : Evaluating the use of Penman-Monteith and Priestley Taylor for modelling peatland evapotranspiration using the Cold Regions Hydrological Model

5.1 Introduction

Evapotranspiration (ET), the combined gaseous water losses from land and plant surfaces, is an important component within boreal plains peatlands, where it is often the dominant vertical water flux (Brown et al., 2014; Thompson et al., 2015). As such, ET has a major influence on peatland water table position, which plays a significant role within the various peatland eco-hydrological feedbacks (Waddington et al., 2015) that maintain their carbon sink status (Gorham, 1991; Roulet et al., 2007). Furthermore, the ecohydrological importance of peatland ET within the broader boreal landscape is likely to increase as the climate changes, leading to increases in peatland ET that surpass even the forested uplands (Helbig et al., 2020). Given the importance of ET rates to peatland ecosystem function, there have been many studies that have quantified ET water losses from peatlands using various *insitu* methods such as lysimeters (e.g. Scarlett et al., 2017; Whittington & Price, 2006), chambers (e.g. Brown, 2010; Gabrielli, 2016), sap flow measurements (e.g. Gabrielli, 2016; Patankar et al., 2015) and site scale measurements using eddy covariance systems (e.g. Van Huizen et al., 2019; Volik et al., 2020). These direct measurements of ET are prone to large uncertainties brought on by the accuracy and precision of each method, as well as the time-consuming monitoring that is required. In addition to *insitu* methods, there have been several mathematical approaches, calculating both potential, (PET) where water availability is unlimited, and actual ET, (AET) where water availability is limited. These approaches include the Bowen Ratio, Priestley-Taylor (Priestley & Taylor, 1972), Penman-Monteith (Monteith, 1965; Penman, 1948), Thornwaite (Thornthwaite,1948), and Granger-Gray (Granger & Gray, 1989) methods. However, the mathematical approaches are also complicated by the parameter requirements, which are often driven by onsite measured meteorological observations, and require a physical knowledge of the site. Still, *insitu* vs mathematical approaches are not mutually exclusive, and often are used in conjunction with each other to develop continuous ET records from a particular field site. When modelling approaches are used to understand peatland ecohydrological processes, a mathematical equation is used to estimate ET, which is then validated against observed field data. Of these, Priestley-Taylor and Penman-Monteith are commonly used

and often integrated into soil-vegetation-atmosphere-transportation (SVAT) models such as the Cold Regions Hydrological Model (CRHM) (Pomeroy et al., 2007).

When using SVAT models that include wetlands, they are often assumed to be evaporating at a potential rate, and so Priestley Taylor is often used (e.g. Krogh et al., 2017; Quinton & Baltzer, 2013; Stone et al., 2019), as it has fewer parameters to determine. Furthermore, the alpha value, which relates actual to potential evaporation rates is often set to 1.26. However, research has shown that northern peatlands, do not always evaporate at potential rates (Volik et al., 2020) as indicated by alpha values (AET/PET) ranging from 0.51-0.97 (Gong et al., 2012a). To calculate AET using Priestley-Taylor, site specific alpha values need to be calculated, that often require the use of *insitu* measurements such as Eddy Covariance. Conversely, the Penman-Monteith equation can calculate AET directly by incorporating the surface resistance term (r_{surf}).

However, while resistance schemes have been well established for vascular plants (Jarvis, 1976; Stewart, 1988), there is greater uncertainty around determining the surface resistance from a moss soil, in part because moss is non-vascular and lacks stomata (Stiegler et al., 2016). For vascular plants, resistance (sometimes referred to as conductance, its inverse) refers to the control that stomata have over the transpiration that occurs within the stomatal cavity (Oke, 1987). As vapor pressure deficit, soil moisture, and energy varies, so too do the size of the stomatal openings (Jarvis et al., 1997; Kettridge et al., 2013). The original conceptualization of surface resistance does not directly transfer to moss and poses a challenge when attempting to model the actual physical process. Many of the resistance schemes used in models are based on vascular plant responses to these driving factors (e.g. Stewart, 1988), or are bulk surface values that have been determined as a residual to the Penman-Monteith equation (e.g. Alves & Santos Pereira, 2000; Raddatz et al., 2009; Stiegler et al., 2016)

Rather than having stomata open and close, moss resistance is controlled by the transport of moisture to the evaporating surface, which is a function of soil tension (Philip, 1957) in the unsaturated layer of the moss and can be impacted by water table decline (Raddatz et al., 2009). As the water table declines, and soil moisture drops, the unsaturated hydraulic conductivity will also begin to decline as tension forces increase (McCarter & Price, 2014). Concomitant with water table drawdown is the evaporation of the water held in the pores formed by the moss, which further reduces the soil moisture at the surface, increasing soil tension beyond equilibrium (Kettridge & Waddington, 2014). At a certain soil tension, the amount of water being transported up to the

surface, at a rate equal to the unsaturated hydraulic conductivity (K_{unsat}), will not be able to meet the evaporative demand at the surface, and a decline in AET will begin to occur. This threshold response occurs (Waddington et al., 2015) as water tables approach 30-40 cm below the ground surface (Romanov, 1968), or a soil tension of 100-200 mb (Clymo, 1973). If the tension reaches >400 mb the hyaline cells in the *Sphagnum* capitulum will begin to drain, and desiccation of the surface moss occurs. However, it is likely that this tension threshold may vary (Kettridge et al., 2016; Lewis, 1988; McCarter & Price, 2014) due to the variation in hydrophysical properties between *Sphagnum* species (Bond-lamberty et al., 2010)

The decline in K_{unsat} and increase in soil tension is akin to the closing of the stomata in vascular plants, and so can be conceptualized as the driver of moss resistance, presenting a physical process that can be incorporated into a SVAT model. By incorporating moss resistance into SVAT models, uncertainty in ET estimates using Penman-Monteith can be reduced (Drexler et al., 2004). It also reduces the reliance for on-site field calibration necessary for site specific approaches, such as the use of alpha values (ratio of actual to potential evapotranspiration) when calculating ET using Priestley Taylor. Such an approach is also inline with the stated methodological philosophy of CRHM, where calibration of model parameters is avoided. Rather, an emphasis on understanding the underlying processes is emphasized, in order to minimize calibration, and allow for the modelling of ungauged basins (Pomeroy et al., 2007). Finally, while the impact of reduction in available energy, brought on by melting SGI, was evaluated for PET in chapter 3, it had not been evaluated for AET. This is due to the difficulty in parameterizing actual evapotranspiration equations such as the Penman-Monteith for moss, brought on by the surface resistance term.

Therefore, the overall objective of this paper is to incorporate a physically representative resistance model for a *Sphagnum* moss layer into CRHM, in order to better represent moss evaporation and ice melt feedbacks. The specific objectives are: (1) to parameterize moss resistance based on the hydrophysical characteristics of the moss/peat soil; and (2) compare the ability of the Penman-Monteith equation to model peatland site scale ET to the Priestley Taylor equation and (3) to assess the impact of melting SGI on Actual Evapotranspiration.

5.2 Methods

5.2.1 Study Site

This modelling study took place at Pauciflora peatland, a poor fen located on the Stoney Mountain uplands (56° 22' 30.36" N, 111° 14" 3.29" W), approximately 40 km south of Fort

McMurray Alberta, Canada (Figure 5-1a) at an elevation of ≈750 masl. The 30 year climate normal (1981-2010) has a mean annual air temperature of 1.0 °C, a mean rainfall of 316 mm (Fort McMurray Airport, Environment Canada) and an estimated mean snow water equivalent of approximately 104 mm, calculated from an empirical relationship between snow density and air temperature (Hedstrom & Pomeroy, 1998).
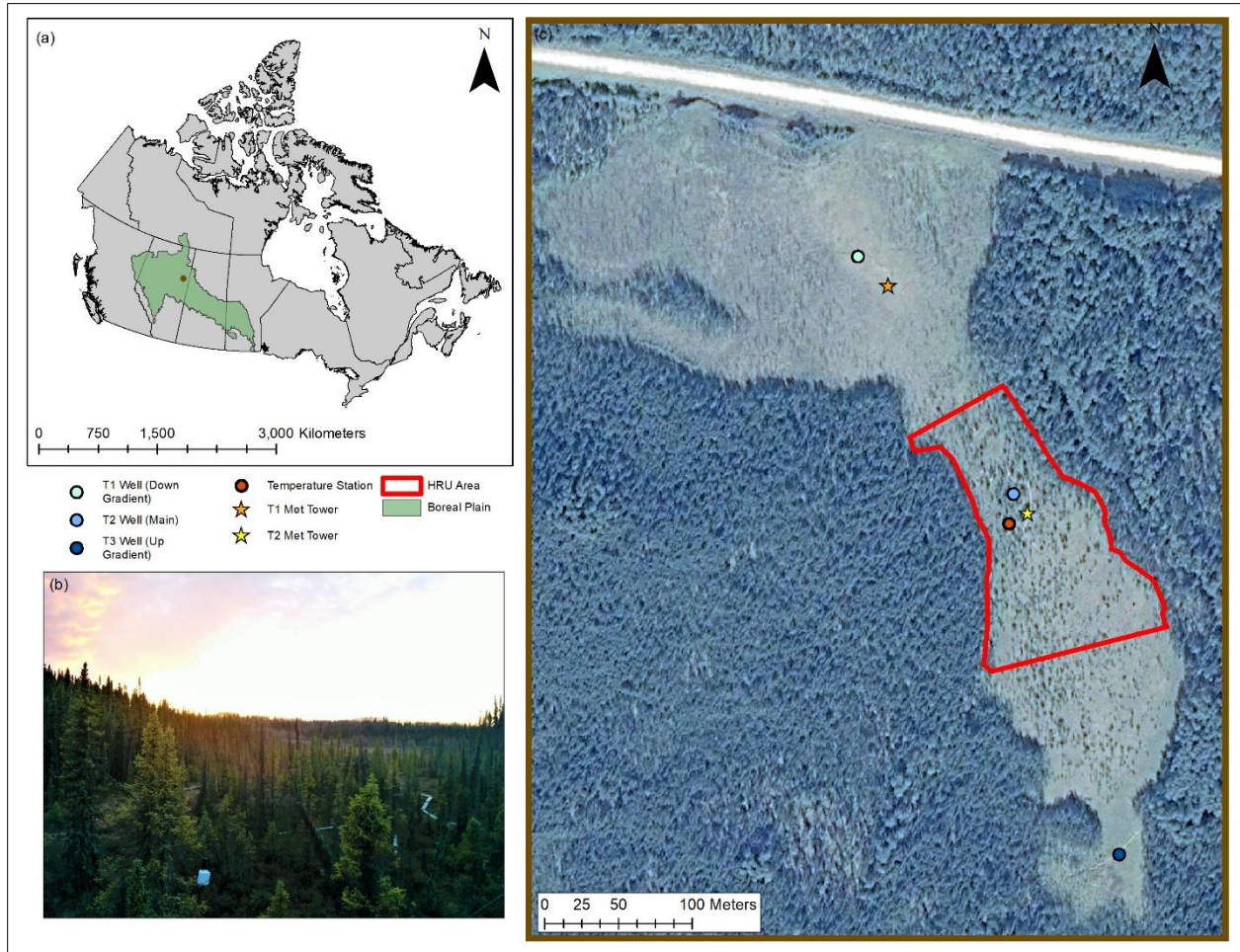
Figure 5-1a) Location of site within Boreal Plain and Canada. (b) Image of location of thermocouple profile. (c) Map of relative location of both met towers, thermocouple profile, and area for model parameterization.

The peat depth at the site varies from 2m to 10 m moving from South to North. Site surface vegetation is comprised of an extensive cover of *Sphagnum* mosses, including *S. angustifolium*, *S. capillifolium* and *S. magellanicum*. It also includes a sparse understory of shrubs including *Ledum groenlandicum*, *Champadaphne calyculata*, *Rhododendron groenlandicum*, *Carex Aquatilis*, and *Eriophorum* spp. Tree cover at the site varied spatially and is comprised of stunted *Picea Mariana* and *Larix Laricina*.

81

5.2.2 Field Observations

Field observations (2012-2019) to drive and validate the model were measured in a 1.3 ha area of the central part of the fen (Figure 5-1b). This area corresponds approximately to the "neck" part of the North fen in Wells et al., (2017). Microtopographic variation between Hummocks, Hollows and Lawns each comprised approximately 1/3 of the surface area.

All meterological variables were measured at a central tower (Figure 5-1c) and included Net Radiation (W/m^2)(CNR4 Net Radiometers, Kipp & Zonen, Delft, Netherlands) (Q^*) and wind speed (*ws*) (m/s)(RM Young 05103, Campbell Scientific, Logan, Utah) measured at 6 m above the peatland surface. Air temperature (*Temp$_{air}$*) (°C) and relative humidity (*RH)* (%) (HMP35C, Vaisala, Helsinki, Finland) were measured 2 m above the peatland surface. All variables were measured at 60 s intervals using a CR1000 data logger (Campbell Scientific Ltd., Logan, Utah). Gaps in the data were filled using several different methods, depending on the size of the gap. When possible, onsite data from another tower was used (Figure 5-1c) by building a linear regression between the two towers. When data from this tower were not available, half hour gaps that spanned more than 3 hours (6 time steps) were filled using linear interpolation between the first measurement before and after the gap. Gaps larger then 3 hours were filled by averaging the data at each timestep across the entire record (2012-2019) and then filled with the average value for each missing timestep.

An eddy covariance (EC) system located on the same meterological tower was used to measure AET continuously and recorded at half hour intervals, 4 m above the peatland surface, following similar approaches used in boreal peatlands (Brown et al., 2010; Volik et al., 2020; Warren et al., 2018). The EC system consisted of a 3D sonic anemometer (Gill Windmaster Pro, Gill Instruments, Lymington, UK) and a closed-path infrared gas ($CO2/H2O$) analyser (LI-7200, LICOR Inc., Lincoln, Nebraska) sampled at 20Hz. EC data were processed in EddyPro soft- ware (LI-COR Inc., Lincoln, Nebraska, USA), in which corrections were made for time lag and sensor separation (Song-Miao Fan et al., 1990), coordinate rotation (Kaimal & Finnigan, 1994), periods of low turbulence and energy balance closure (R. M. Petrone et al., 2015), and density effects (Burba et al., 2012). A footprint analysis (Kiljun et al., 2004) was completed to remove fluxes that originated from outside the fen, (i.e. the surrounding forested hillslopes). This resulted in a mean flux footprint (2014-2018) area of 0.32 ha, extending ≈41 m north, ≈37 m south, ≈26 m west, and ≈22 m east from the meteorological tower. Gaps in the final ET values were filled using PET as

82

calculated by the Penman Monteith Equation (still accounting for aerodynamic resistance) and Priestley Taylor, with an onsite calibrated alpha value.

A ground temperature monitoring station was installed ≈15 m away from the tower (Figure 5-1b,c). Subsurface temperatures were recorded at 2, 5, 10, 20, 50, 75, 100 and 150 cm below the peatland surface, in a hollow. Measurements were taken using a Type-T thermocouple (Omega Engineering, Norwalk, Connecticut, USA) every 60 s and averaged at 60 min intervals and then at daily intervals. Gaps that exceed 3 days were filled using the similar approach to the meteorological data, where each day was averaged across the entire record, and then filled with the average value for the corresponding year. Gaps smaller then 3 days were filled using linear interpolation.

5.2.3 CRHM Description

CRHM is modular modelling platform(Pomeroy et al., 2007) that discretizes the modelling domain into a series of hydrological response units (HRU) where each HRU can have its own distinct physiographic, meteorological, and ecohydrological characteristics, depending on the spatial scale the modeller is using. Different modules are available that have routines which model individual ecohydrological processes, that can be linked together to form a cohesive ecohydrological model. For this study, only one HRU was used, and corresponds to the area shown in Figure 5-1a, which was chosen to simplify the model and allow better control of the hydrological inputs and outputs (modules used are listed in Table 5-1). All parameters for the module were either quantified based on the physiographic, meteorological, and ecohydrological characteristics of this area, or literature values.

Table 5-1 List of the modules used in CRHM, and their associated purposes and supporting studies.

Modules (module name and variation number)	Description
1. Observations (obs):	Handles the driving model inputs of windspeed, precipitation, temperature, *relative* humidity, and actual vapour pressure.
2. Albedo (albedo):	Estimates snow albedo using net radiation, max and min air temperatures, snowfall and SWE. (Gray & Landine, 1987)
3. Global	Calculates direct and diffuse shortwave radiation and the number of sunshine hours.
4. Shortwave Radiation (Annandale#1)	Calculates incoming shortwave radiation. (Annandale et al., 2001)
5. Longwave Radiation (longvt#2)	Calculates incoming longwave radiation based on incoming shortwave radiation. (Sicart et al., 2010)
6. Net Radiation (netall)	Uses the observed net radiation as measured *insitu*
7. Canopy Clearing (CanopyClearing#4):	Models net all wave radiation at the snow surface under a needleleaf forest canopy based on incoming shortwave radiation
8. No blowing snow (NO_pbsm):	Calculates snow water equivalent for areas where there is no blowing snow.
9. Energy Budget Snowmelt (ebsm#1)	Calculates the snowmelt from the snowpack using net radiation, sensible & latent heat, and advection from rain. (Gray & Landine, 1988)
10. Evapotranspiration (peat surface resistance)	A customized version of evap_resist that incorporates moss resistance into the calculation of surface resistance for use in the Penman-Monteith Equation (Monteith, 1965)
11. Priestley Taylor (Alpha):	A customized version of evap_resist that allows for user defined alpha values for calculating Priestley Taylor evapotranspiration (Priestley & Taylor, 1972)
12. Ground Surface Temperature (tsurface#1):	Used to calculate the ground surface temperature. In this model, it was parameterized with observed temperatures measured at 2 cm below the ground surface.
13. Infiltration (frozenAyers):	Handles snowmelt and rainfall infiltration into frozen, partially frozen and unfrozen soils (Zhao & Gray, 1997).
14. Soil Moisture Balance (SoilX):	Estimates the groundwater flow, soil moisture, and exchanges of water between the surface and subsurface.
15. Soil Freeze/Thaw (XG):	Calculates the depth of freezing and thawing in one direction using a modified form(Xie & Gough, 2013).

5.2.4 Input Data and Model Validation

The model was driven by meteorological data listed in Table 5-1-Observations as measured on site, running from October 29, 2012-September 26, 2019. Model validation was completed by comparing modelled ET using the Penman-Monteith and Priestley Taylor Equations to EC ET. Specifically, the metrics of r^2, Mean Average Error (MAE), and Root Mean Square Error (RMSE) were used. All statistical tests were run using R statistical software (R Core Team, 2020) and the R Stats Package (Team & Contributors, 2020). To evaluate the effectiveness of Priestley-Taylor versus Penman-Monteith in estimating site AET, multiple forms of Model ET were run. They included Priestley Taylor with a site-specific alpha (0.75) (*PT-PET$_{0.75}$*), and Priestley Taylor at Equilibrium (*PT-PET$_{eq}$*) where alpha is set to 1. The site-specific alpha was determined by taking the yearly growing season average of alpha, which calculated as,

$$Alpha = \frac{AET}{PET}$$

(5-1)

where *AET* is the half hourly actual evapotranspiration as measured by the EC tower, and *PET* is the potential evapotranspiration as measured using Penman-Monteith equation where surface resistance is ignored. The average value is based on data only from when the EC tower was on, which varied from year to year (see Table 5-2). When running the model, for times that existed outside of these timeframes, alpha was set to 1.

Table 5-2 EC system operation dates at Pauciflora fen, Fort McMurray, Alberta Canada, 2012-2019.

Start Date	End Date	Number of days
May 18, 2013	August 2, 2013	76
May 3, 2014	October 2, 2014	152
March 17, 2015	September 29, 2015	196
June 6, 2016	October 10, 2016	126
May 17, 2017	September 21, 2017	127
April 1, 2018	September 14, 2017	166
April 27, 2019	September 23, 2019	149

5.2.5 Implementation of a Water Table Metric, Moss Resistance Scheme, & Peat Specific

Parameterizations

CRHM also supports customization using macros and coding in C++ language. The relative position of the water table is not calculated in CRHM, so an empirical relationship was developed between observed water table and observed equivalent depth (mm) (see Appendix C, Figure C-1).

This was then implemented into the code to calculate hydraulic conductivities. The current form of resistance used was developed for vascular plants, and so a new resistance module was developed for this study. To estimate moss surface resistance (Ω_{moss}), bulk site scale resistance ($\Omega_{Bulk\ Surface}$) was calculated by following the approach used by

$$E = \frac{(\rho_{vs}^* - \rho_{va})}{r_s + r_a} \quad (5\text{-}2)$$

Where E is the evaporation rate in kg H_2O/30 min, which was taken using the on-site EC ET measurements, where ρ_{vs}^* is the saturation vapour pressure density (kg/m³) of the peat surface, ρ_{va} is the vapour density of the air (kg/m³), r_s is the average surface resistance during the 30 min intervals (sec/m) and r_a is the average aerodynamic resistance (sec/m). The rs was assumed to equal the $\Omega_{Bulk\ Surface}$. The ρ_{vs}^* and ρ_{va} were calculated using equation 5-3 and 5-4

$$\rho^* vs = \frac{es}{\left(\left(T_{soilSurf} + 237.15\right)\Big/2.17\right)}$$

$$(5\text{-}3)$$

$$\rho v = \frac{ea}{\left(\left(T_{Air} + 237.15\right)\Big/2.17\right)}$$

$$(5\text{-}4)$$

where es and ea are the saturated actual vapor pressures (kPa), and $T_{soilSurf}$, T_{Air}, are the soil surface temperature (°C) and the air temperature (°C).

Vascular resistance ($\Omega_{Vascular}$) was then calculated using the approach by Jarvis (1976), and subtracted from $\Omega_{Bulk\ Surface}$. The difference was assumed to be equal to Ω_{moss}. These values were then filtered to exclude any negative values (due to nighttime measurements, or erroneous values, and set to max out at 5000 sec/m, an arbitrarily high value that would result in no evapotranspiration. A relationship was developed between Ω_{moss} and the ratio (Kratio) of unsaturated hydraulic conductivity (K_{unsat}) to saturated hydraulic conductivity (K_{sat}) shown (Figure 5-2). K_{sat} was based on Goetz & Price (2015) who conducted retention experiments on soil cores at Pauciflora. K_{unsat} was calculated using the van Genuchten-Mualem parameters (Mualem, 1976; van Genuchten 1980), and optimizing them for the a and n parameters (Elliott & Price, 2020). See Appendix C for more details. K_{unsat} was calculated for the 0-1cm layer of the peat soil, using

equation C-2. The Ω_{moss} was then averaged according to the Kratio. Kratios were rounded to the nearest 1000th, and then the associated Ω_{moss} values were averaged accordingly (see Table 5-3).

Table 5-3 Binned Kratios and the associated average Ω_{moss}, and confidence intervals. The values in the brackets denote the number of values used to calculate the average Ω_{moss}.

Kratio	Average Ω_{moss}	Confidence Intervals
0.001	39	16.3 (n=7)
0.0011	45.7	28.2 (n=11)
0.0012	45.7	30.8 n=(21)
0.0013	39.3	20.0 (n=16)
0.0014	23.8	8.4 (n=13)
0.0015	15.9	10.6 (n=6)
0.0016	15	10.8 (n=5)
0.0017	35.7	42.4 (n=2)
0.0022	16.3	0.8 (n=2)
0.0026	35.2	N/A (n=1)
0.0032	6.2	5.2 (n=2)
0.0076	7.9	N/A (n=1)

An exponential equation was then fit to the dataset (Figure 5-2) that could be implemented into CRHM,

$$Resistance_{model} = a * Kratio^b$$

(5-5)

where *a* and *b* are fitting parameters that correspond to the intercept and exponential increase in resistance, and the Kratio is the ratio of K_{unsat} to K_{sat}. In this case *a* and *b* were optimized by minimizing the RMSE and MAE, which is shown in Table 5-3.

Table 54 Fitting Parameters for an exponential relationship between the Kratio and Ωmoss. The values in brackets are the parameters and model fit metrics after the adjustment of a and b parameters.

Parameter		RMSE (sec/m)	MAE (sec/m)
a	3.625×10^{-3} (3.7×10^{-18})	9.9 (30.5)	8.2 (27.1)
b	-1.37 (-4.9)		

This initial curve (shown in blue in Figure 5-2) would initiate resistance values at Kratios $<10^{-3}$. The water table position that corresponded with Kratios of that magnitude though were quite shallow (see inset Figure in 5-2), and not as deep as the reported water table threshold for evaporative decline in peatlands(Romanov, 1968). Therefore, the parameters for *a* and *b* were further adjusted so that initiation of $Ω_{moss}$ would occur at approximately 35 cm below the peat surface (see Calibrated Model in Figure 5-2).
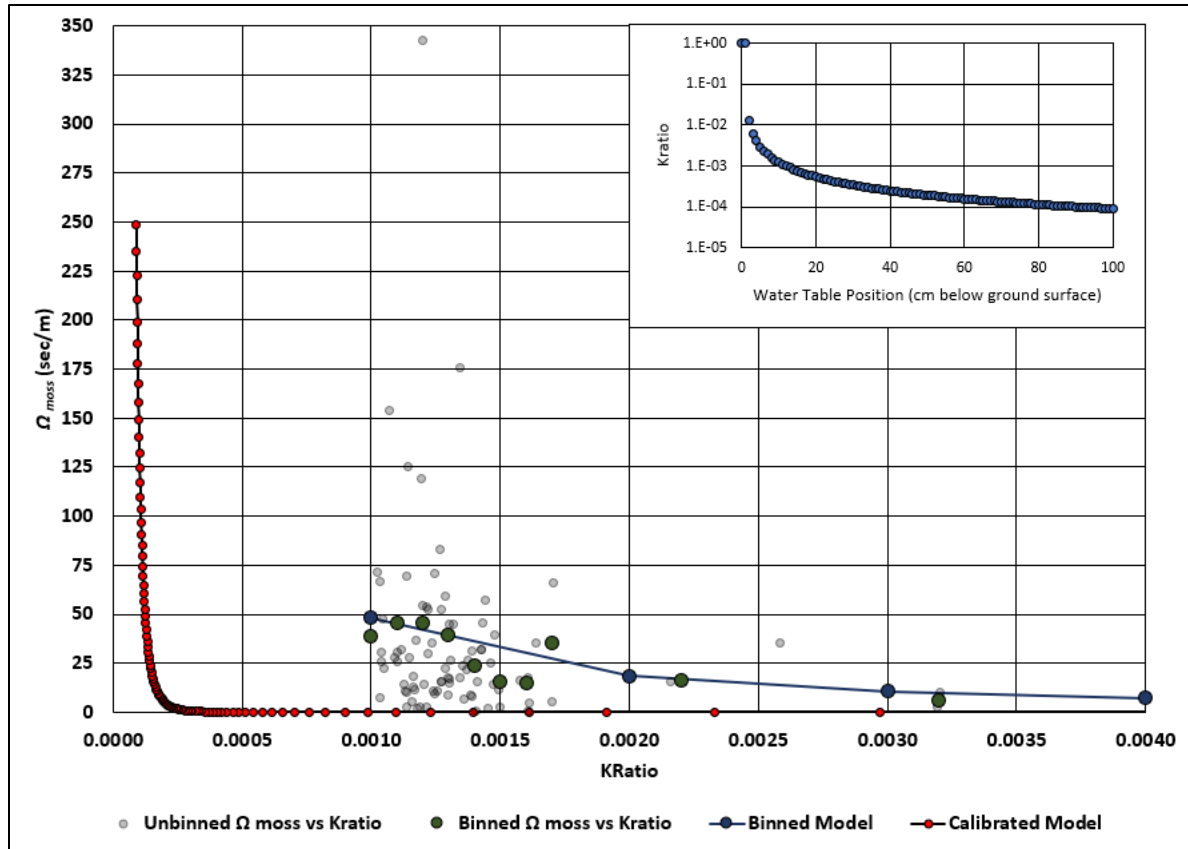
Figure 52 Relationship between Ω_{moss} from inverting Equation 2 and the Kratio for the 0-1cm layer. The grey line represents the initial model fit, while the red line represents the final modeled curve after adjusting for water table position. Inset figure is the relationship between water table position and the Kratio.

The equation parameters of *a* and *b* were calibrated so that Ω_{moss} would not initiate until the water table position exceeded ≈ 35 cm below the peat surface, in line with some field observations (Kettridge et al., 2021; Romanov, 1968). Due to the sparse tree cover throughout the site, $\Omega_{vascular}$ was weighted by the number of trees (521) and the average LAI of 0.55 as reported by (Gabrielli, 2016). The final model bulk resistance was then calculated as the sum of Ω_{moss} and $\Omega_{vascular}$.

By using a single HRU for our model domain, a custom ground water input and output was needed to maintain adequate water table positions and prevent the modelled wetland from drying out. A variable head approach was used (Appendix C), using an additional monitoring well up gradient and down gradient from the main monitoring well (Figure 5-1c). Relationships were developed between the main monitoring well and these other two wells (Appendix C). Using Darcy's Law, the horizontal input and output of groundwater from the HRU could then be calculated.

5.2.6 Incorporation of Melting Seasonal Ground Ice Impacts on the energy balance

To properly account for the reduction in available energy due to melting SGI (see Figure 2-8), the daily ground heat flux (as calculated in Chapter 2) was converted to a percentage of daily net radiation. Each daily value was then subdivided evenly over the daylight periods for each model run at an hourly time step. Model runs for AET with and without the incorporation of the ground heat flux were run and compared to each other, to assess the cumulative impact over the course of each growing season.

5.3 Results

5.3.1 Priestley Taylor vs Penman-Monteith

The CRHM output of evapotranspiration values were summed to the daily timestep before filtering for only when the EC tower was running. The linear regressions are shown in Figure 5-3.
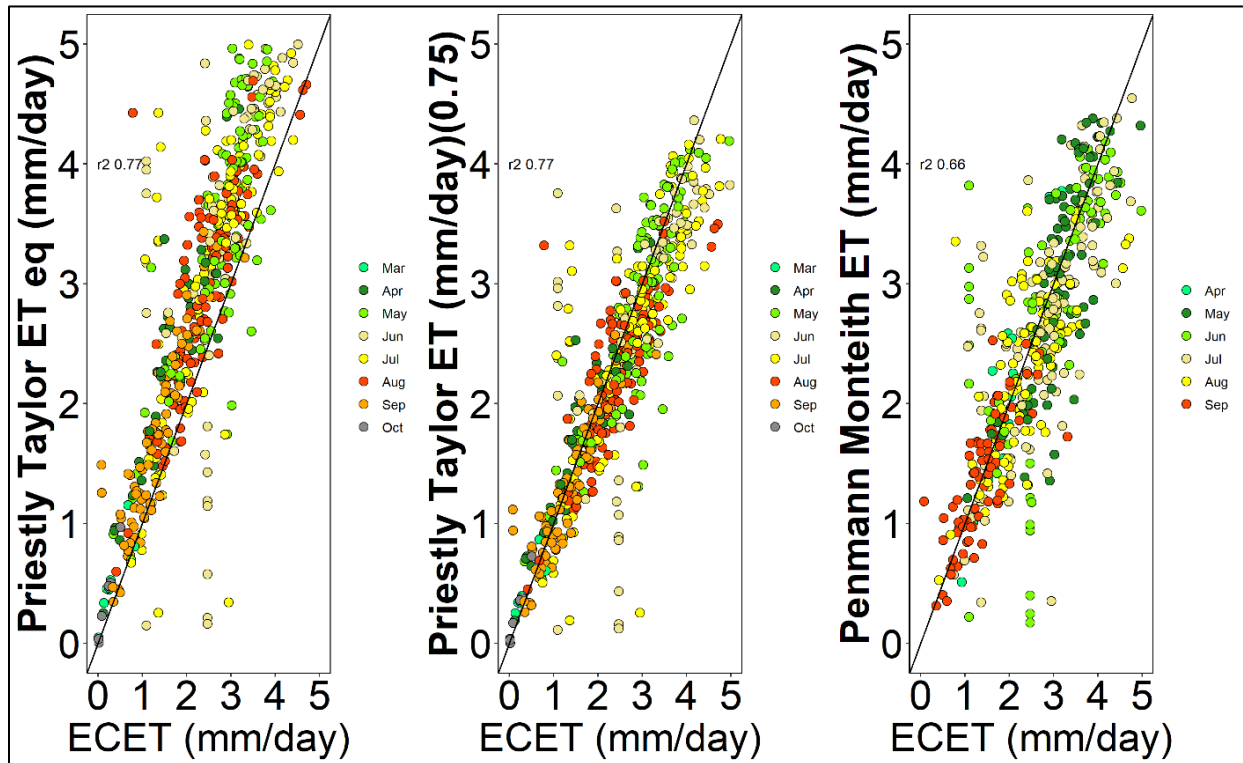
Figure 53 Linear Regressions of Daily EC-AET vs (left panel) PT-PET$_{eq}$, (center panel) PT-AET$_{0.75}$, and PM-AET (right panel). Both Priestley Taylor approaches show positive. The line represents the 1:1 line. Values above the line represent an overestimation, values below the line represent an underestimation.

All three approaches showed generally good fit along the 1:1 line, where *PT-PET$_{eq}$* , *PT-AET$_{0.75}$* and *PM-AET* had r^2 values of 0.76, 0.77, and 0.66, respectively. Table 5-5 shows the main metrics used to assess model fit, including RMSE, MAE and Average Bias.

Table 55 Model Metrics used to validate the different evapotranspiration approaches. Root Mean Square Error (RMSE) and Mean Average Error (MAE) indicate model fit. The lower the value, the better the fit. Model Bias indicates whether the model is underestimating or overestimating. A value of 0 indicates perfect fit.

Model Run	RMSE (mm/day)	MAE (mm/day)	Average Bias (%)
PT-PET$_{eq}$	0.89	0.70	25
PT-AET$_{0.75}$	0.55	0.38	-6.2
PM-AET	0.61	0.44	-4.0

The highest RMSE, MAE, and Bias were associated with *PT-PET$_{eq}$* while *PT-AET$_{0.75}$* had lower RMSE (0.55) and MAE (0.38) compared to *PM-AET*, 0.66 and 0.44, respectively. However, *PM-AET* had the lowest model bias at -4%, compared to the -6.2% of *PT-AET$_{0.75}$* and *PT-PET$_{eq}$* 25%. Of note, is a larger deviation from the 1:1 line for *PT-PET$_{eq}$* that occurs at EC ET values ≈ >3 mm/day. ET model outputs were also summed to the yearly value and are shown in Figure 5-4. Like the daily results, *PM-AET* and *PT-AET$_{0.75}$* performed similarly to each other across all years, whereas the *PT-PET$_{eq}$* exhibited higher differences from the observed values.
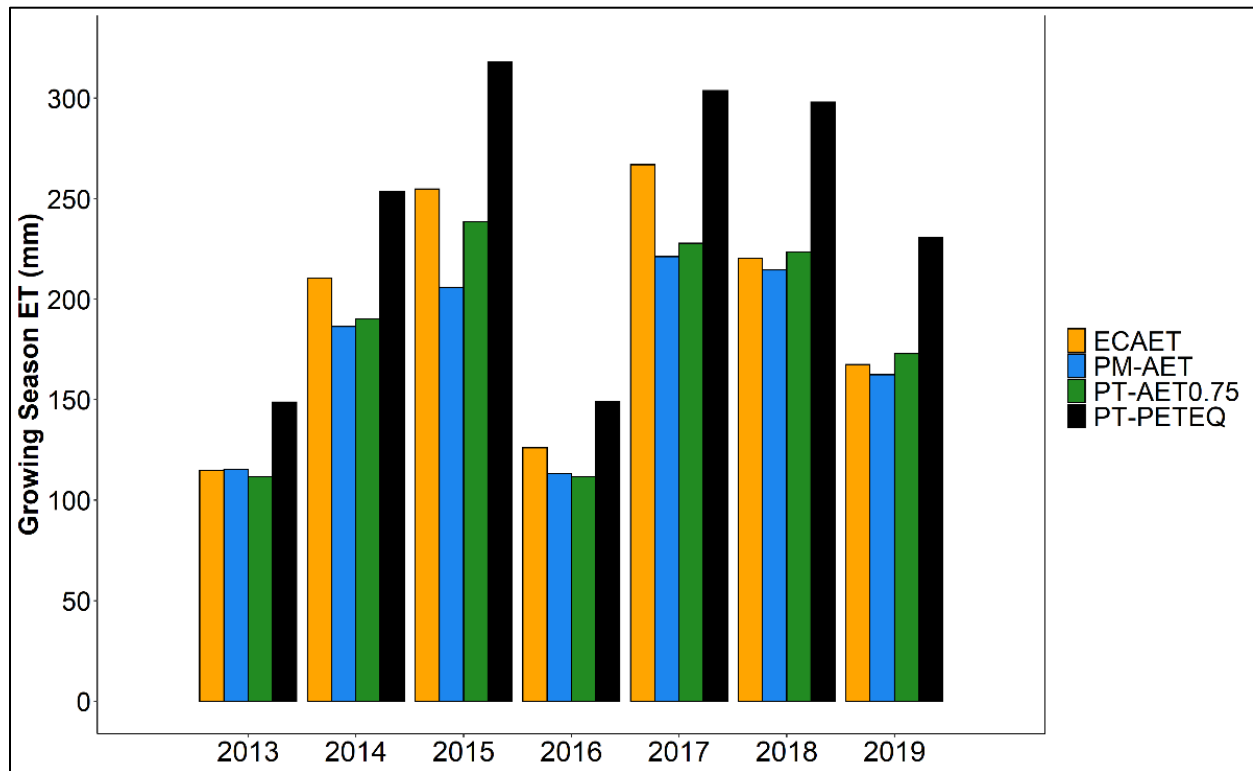
Figure 54 Yearly ET Totals for each CRHM model run and the observed EC data, Pauciflora Fen, Fort McMurray, Alberta, Canada, 2013 – 2019.

Percentage differences between the observed and modeled values were similar for both *PM-AET* and *PT-AET$_{0.75}$* across all years as well (-9.0 % (±7.6%) & -5.7 % (±6.8%), respectively, where ± are the standard deviations). Conversely, *PT-PET$_{eq}$* had an average percentage difference of 25.7% (±9.0%).

5.3.2 Modelling Moss Resistance

Modelled moss resistance and modelled *PM-AET* were compared to assess the relationship between the two variables and are shown in Figure 5-5.
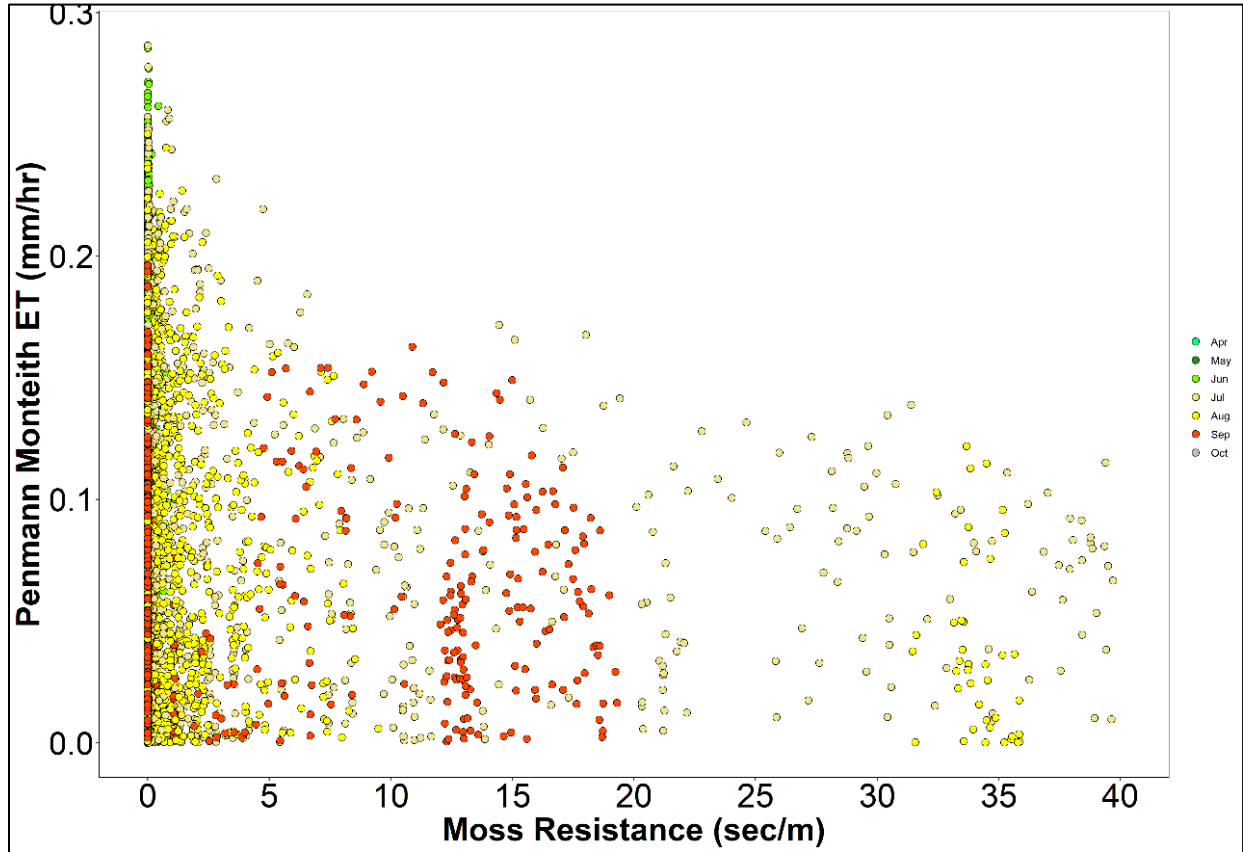
Figure 55 Modelled Moss Resistance vs Modelled PM-AET. In order to compare to the observed data which was at 30 minute intervals, the modelled evapotranspiration was divided by 2.

Although PM-AET varied considerably for a given moss resistance, there was a general decline in the range of PM-AET with moss resistance. Between 0-5 sec/m, AET ranged from 0-0.3 mm/30 min. This range shrank when moss resistance was between 6-20 sec/m (0-0.2 mm/30 min) and then again when resistance was between 21-45sec/m (0-0.1 mm/sec). A decline was also found when binning the EC ET and Ω_{moss} data; between 0-5sec/m AET ranged from 0-0.04 mm/hour, then between 6-30 sec/m, it ranged from 0-0.03 mm/30 min. However, while model AET declined by 0.3 mm/hr, observed data showed a much smaller decline 0.01 mm/hr over similar resistance values (0-35 sec/m). Modelled and observed Ω_{moss} were averaged to the daily timestep and are shown in Figure 5-6.

92
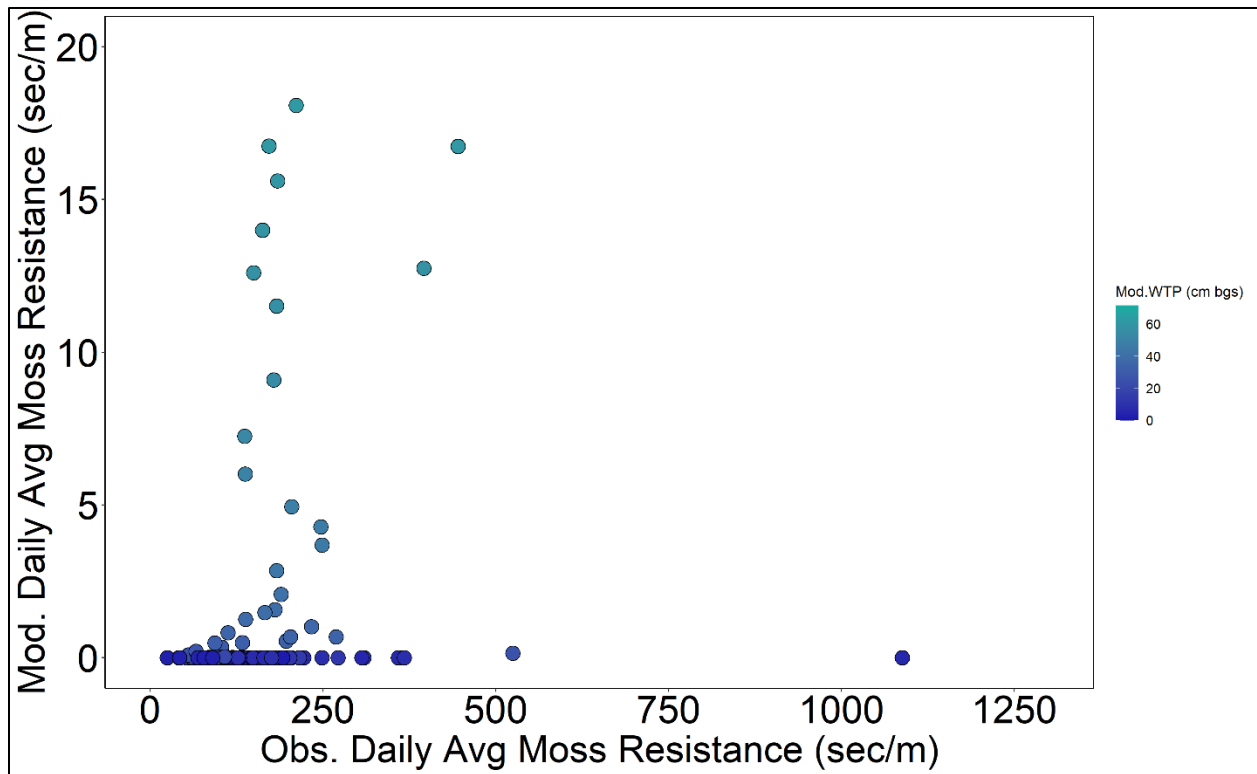
Figure 56 Observed Moss Resistance vs CRHM Modelled Resistance, Pauciflora Fen, Fort McMurray, Alberta, Canada, 2013 – 2019. Colour grade represents the modelled water table position in cm below ground surface.

There was poor fit between modelled and observed moss resistances. While observed values ranged from 45-1271 sec/m, modelled moss resistance had a much smaller range, 0- ≈20 sec/m. Modelled resistance only began to increase after the water table reached ≈40cm below the peat surface while the observed data showed variable resistance, ranging from 0-1250 sec/m. It should be noted here that these water table values were rarely reached in the observed data, where the maximum depth to water table was 40 cm bgs.

5.3.3 Ground Heat Flux and Actual Evapotranspiration

Table 56 The results from the two contrasting model runs; with and without the incorporation of the ground heat flux into the calculation of evapotranspiration.

Year	AET (with QG) (mm)	AET (no QG) (mm)	Difference. (mm)	% Difference
2013	290	282	7	3
2014	262	257	6	2
2015	285	281	4	2
2016	297	291	6	2
2017	352	343	9	3
2018	330	324	7	2
2019	321	316	6	2

The results in Table 5-6 indicate that reductions are larger during the portion of the spring melt when SGI is actively melting. While on an annual growing season basis (April-September) the impact of the ground heat flux on the available energy for evapotranspiration is quite small (<10 mm). This amounts to an average percentage difference of 2 (±0.4) % between the AET estimations when incorporating Q_G and when excluding it.

5.4 Discussion

5.4.1 Penman-Monteith or Priestley Taylor?

When assessing the results for the modelling of the Penman-Monteith and Priestley Taylor approaches, it is important to keep in mind the requirements for parameterization. While Priestley Taylor requires fewer parameters than does Penman-Monteith, it does require an alpha value, which can either be set to 1.26, the standard, or a site-specific value that is calibrated from observations. While all three approaches reported here achieved good estimations, with low RMSE & MAE and high r^2, the model bias values indicate that the *PM-AET* approach may be the most suitable. It had the lowest bias (-4%) compared to *PT-AET$_{0.75}$* and *PT-PET$_{eq}$* (-6.2%, 25%). Furthermore, the *PM-AET* does not require an onsite EC tower to calculate a site-specific alpha. EC towers are expensive and require substantial expertise and data processing to operate and so are rare. For long term monitoring sites, the *PM-AET* can achieve reasonable results in AET estimations without EC towers.

Furthermore, these results indicate that the assumption of wetland AET=PET, often used in site scale eco-hydrological models (e.g. Krogh et al., 2017; Quinton & Baltzer, 2013; Stone et al., 2019), is not valid. AET was routinely less then PET, and when modelled assuming potential conditions at equilibrium, site scale ET was vastly overestimated (Figure 5-4), by as much as 78 mm on an annual growing season basis, with a mean % difference of 26% (±9%), while *PT-AET$_{0.75}$* was-6% (± 7%) and *PM-AET* was -9% (± 8%). If an alpha value of 1.26 was used, it would lead to even larger model bias. While Priestley-Taylor can capture the overall trend in AET, it can lead to overestimation. Similar results were reported by Stone et al. (2020), where Priestley-Taylor was used for a bog. While the authors do not report an alpha value for their work, if they used the CRHM default, then a value of 1.26 would have been used, which may explain the large overestimations in wetland ET reported there as well. By including a site-specific alpha value, Priestley Taylor outperformed *PM-AET*. However, the ability to develop one is not always

feasible, and in such instances when modelling or monitoring wetland ET, Penman-Monteith should be considered.

5.4.2 Challenges in Determining Moss Resistance

Implementation of a surface resistance scheme for moss into a SVAT model such as CRHM is an important step towards better representing peatland ecohydrological processes in these models. Applying a vascular approach, such as Jarvis, (1976) or Stewart, (1988) to a non-vascular plant would likely lead to errors, as the basic physical process behind resistance differs between vascular and non-vascular species. To date, there have been several different ways that moss resistance has been handled. The first, is to assume that there is no moss resistance, and that evapotranspiration is occurring at potential rates within a peatland until surface, sub-surface and intercepted moisture are limited (e.g. Krogh et al., 2017; Stone et al., 2019). Yet, it is clear that there are other times when moisture can be limiting for peatlands (Elmes & Price, 2019; Kellner, 2001; Wells et al., 2017; Wells & Price, 2015). Connon et al., (2014) reported an alpha value of 0.69 for a permafrost peatland in the Northwest Territories, Canada, while Gong et al. (2012) reported a range of alpha values (0.51-0.97) from peatlands in Finland, and in the WBP, Petrone et al., (2007) reported an alpha value of 0.69 for a peatland surface, and Price (1991) reported an alpha value of 0.87. The alpha value used in this study falls within these ranges; 0.75 (±0.25) and suggests that moisture is at times limiting. In other modelling approaches such as in Hydrus-1D, (Kettridge et al., 2016; McCarter & Price, 2014) a critical threshold can be set, around 400 mb, which falls between the reported thresholds of *Sphagnum* moss, ≈ 100-600 mb (Hayward & Clymo, 1982; Lewis, 1988). While not explicitly modelling resistance, as it is a model parameter that limits evaporation, it functionally acts as a resistance threshold. However, this approach assumes that peatland resistance does not initiate before this threshold (McCarter & Price, 2014). Once modelled pressures in the *Sphagnum* capitulum reach this threshold, evaporation is reduced. Raddatz et al. (2007) employed a similar approach to that used in our study, where resistance was determined as a residual value of evapotranspiration equations. Our study has adapted the theory of both the McCarter & Price (2014) and Raddatz et al., (2007) approaches, where Ω_{moss} was determined as a residual, but then its association with the *Kratio* was linearized to achieve a threshold response. As shown in Figure 5-5, moss resistance was seldom initiated, in part due to higher water tables at Pauciflora, making it difficult to validate the modelled resistance values.

Another possible explanation in the discrepancy between modelled and observed values could be due to how each Ω_{moss} value were calculated. The initial calculated values ranged between 0-5000 sec/m, after filtering out erroneous values, and resistance values that coincided with nocturnal hours (Appendix C, Figure C3). Despite the potential for apparent observed peat resistance values to reach >1000 sec/m, this level was seldom reached, and was between 2 and 3 standard deviations of the mean observed Ω_{moss} value 130 sec/m (±404).

While values of resistance over 1000 sec/m coincide with half-hourly AET values <0.05 mm/30 min, which is low and to be expected, there were many instances where the observed moss resistance was near the mean value of 130 sec/m, yet the corresponding half-hourly AET values were occurring near the maximum for half-hourly rates (≈0.1 mm/30 min). This is likely due to the range in energy inputs, such as net radiation, which has a positive, approximately linear relationship with AET. Net radiation sets the upper limit for the AET rate, which is then reduced by the resistance value. However, this is contrasted by the modelled results, where modelled moss resistance values of ≈40 sec/m were associated with ET<≈0.1 mm/30 min, and a general decline in AET is evident (Figure 5-5). If modelled resistance values reached into the hundreds, modelled AET would be consistently shut off in CRHM, as it follows equation 1. This discrepancy is because while observed Ω_{moss} is calculated in part as a function of net radiation (through inverting the Penman-Monteith equation), the modelled Ω_{moss} values are not, they are a function of the soil moisture dynamics only, and can only begin to increase once the water table position approaches 40 cm. These results suggest that PM-AET may be more sensitive to modelled Ω_{moss} then what is suggested by the observed values.

Further complicating this analysis is that observed resistance values fall in line with other reports, which would suggest that moss resistance does indeed occur. Raddatz et al. (2007) reported peat resistance values ranging from 0-1200 sec/m, with the majority being <400 sec/m. However, they report resistance values beginning with water tables as low as 8 cm below the hollow surface, which are relatively shallow for peatlands. Such shallow water tables initiating a resistance response may be due to the differences in vegetation. Brown mosses were the dominant moss at the site used by Raddatz et al. (2007), which have lower capillarity compared to *Sphagnum* moss, making them more susceptible to water stress with shallower water tables (Goetz & Price, 2015). In a controlled peat core experiment, Kettridge & Waddington (2014) report a combined surface resistance and aerodynamic resistance values ranging from 0-1000 sec/m. Although not

specifically a peat resistance, as the cores were taken from *Sphagnum*-based peatlands, it is reasonable to assume that variation in their reported total resistance values were dominated by moss resistance. Kettridge et al., (2021) go on to report *insitu* observed peat resistance values approaching 10000 sec/m, which, although like our observed data, such values represent the maximum values that are seldom reached, and the authors attribute them to low AET values used to calculate resistance. Such a scenario may explain the high resistance values seen in the observed data at Pauciflora as well, as they often coincide with low net radiation, which is likely a dominant control on peatland evapotranspiration at Pauciflora (Chapter three). Yet despite these observed resistance values, ET is still clearly occurring in these sites. This complicates the modelling approach used in this study, as even relatively low resistance values ranging between 100-800 sec/m would have a corresponding ET range of 0.2-0.03 mm/30 min.

Kellner (2001) reported daily mean bulk surface resistances between 100-300 sec/m. The author highlights a similar challenge seen in our observed data for Pauciflora, where with moss evaporation making up a large proportion of the site AET, with resistance values still high, especially when the mosses would be near saturated levels. They suggest that this is due to small scale advective effects, where as the moss dries out, it provides sensible heat to the canopy layer, increasing transpiration (Kim & Verma, 1996). While the increase in transpiration would be captured by the EC tower at our site, the sub-canopy sensible heat would not. The modelled approach used here suggests that only low resistances are needed to decrease ET for moss. Another reason for this discrepancy may be that our approach does not account for the reduction in soil water pressure via evaporative losses. If we conceptualize the capitulum as a control volume for water, where inputs and outputs of water control the volume's soil water pressure, then inputs of water would be water supplied via capillarity, and precipitation. The main output would be evaporation and gravity drainage. Our approach does not account for the effect on pressure that the added loss of water via evaporation would provide. This is how pressures of -100-800 cm can occur, despite, water tables in peatlands rarely dropping to 100cm (Kettridge & Waddington, 2014). The mismatch in magnitude of our resistance values between modelled and observed, may be caused by this, where the water table position corresponds to a much higher resistance value. A third potential reason for the discrepancy between the concurrence of relatively high resistance values and evapotranspiration rates is that our approach is not capturing vapour flow. While it is assumed that evaporation is occurring at the surface, it is possible that vapour flow within the pore

moss pore network is occurring at a lower depth. So despite there being higher resistance values due to lower water tables and soil moisture, there can still be upwards vapour flow towards the surface (Price & Whittington, 2010). However, the authors concluded that this amount of evaporation represented only ≈ 1% of the entire mass flux of water moving through the peat. If this amount is the typical for peatlands, then it is likely that it does not solely explain the discrepancy between observed peatland resistance values and high ET rates. Clearly, more work is needed to parameterize the various feedbacks between moss resistance and evaporation.

5.4.3 Melting SGI Impact on Actual Evapotranspiration Rates

In chapter 2, the impact of melting SGI on evapotranspiration rates was explored, however it was limited to analyzing the impacts on potential evapotranspiration. By incorporating a moss resistance, the impacts on actual evapotranspiration could be evaluated. Table 5-6 shows that the overall impact is relatively small for this particular peatland, where the average growing season difference in estimating actual evapotranspiration was ≈ 2%. This is because on an annual basis, SGI at Pauciflora is generally completely melted away by June. Any reduction in available energy is during the lower evaporative months of April and May, which further reduces its impact on an annual basis. For Pauciflora, this means that the presence of SGI is likely not an important factor for peatland maintenance in the sub-humid climate of the WBP. However more research is needed in other peatlands, to see if this is the case for peatlands across the WBP.

5.5 Conclusion

The purpose of this study was to evaluate the use of the Penman-Monteith, and Priestley-Taylor equations for use in a boreal peatland, and to incorporate a moss resistance into those calculations. While AET models performed well, and Priestley-Taylor had slightly better metrics than Penman-Monteith, its use of a site-specific Alpha value to achieve such results limits its transferability to other peatland locations, without the use of intensive field measurements. Furthermore, the assumption that peatlands evaporate at potential rates when incorporating them into models will likely lead to overestimation and model error. However, the use of the PM methods is complicated by the parameterization of the surface resistance term. The approach outlined here, where resistance is related to the ratio of Kunsat/Ksat was used. However, full validation of this approach was made difficult by the generally wet conditions at the site, and the method in determining observed surface resistance. It is possible that for wet fens, a relationship between the *Kratio* and moss resistance may not be as prevalent. Future studies should look at employing it at a drier site

such as a bog, where the chances of drier conditions can persist longer. Furthermore, extensive studies are needed to better quantify the interactions between moss resistance, water table position and near surface soil moisture dynamics, to account for the range in moss species specific hydrophysical properties. Finally, for this particular peatland, the reduction of available energy and subsequently actual evapotranspiration, brought on by melting SGI, is relatively small on an annual basis, and is likely not an important peatland ecohydrological feedback that contributes to peatland maintenance in the sub-humid WBP. This can form a baseline for future peatland modelling work that continues to incorporate the relationships outlined in this paper, to better incorporate peatlands ecohydrological processes into model developments.

Chapter 6 : Conclusion

The impetus for this study was driven by a need to better understand and represent peatland processes in ecohydrological models such as CRHM. To date, from an evaporation standpoint in SVAT models, peatlands had been essentially treated as open bodies of water, where evaporation can occur at potential rates. However, as the roles of peatlands in the carbon cycle have become more defined with climate change continuing to increase temperatures, it was imperative that a better understanding of all the different peatland processes be understood. The role of persistent SGI and its melting was one such parameter.

As the first chapter highlighted, the role of SGI in boreal peatlands is complex. As SGI melts, it lowers the upper limit of PET in the springtime due to a reduction in available energy, reducing evaporative losses. At the same time, its melting releases substantial water at the surface, maintaining near saturated conditions. This has important implications for the role of peatlands, particularly in the boreal plains. The peatland studied was in a head water catchment, and the presence of SGI may well control spring runoff for downstream systems. As the climate continues to warm, it raises questions about how the SGI role may change. What is clear though, is that SGI can play an important role in both vertical and lateral water fluxes within a peatland. The challenge then becomes, how do these processes get incorporated into our models, and what is the best way to represent them.

The second chapter addressed some of these questions by looking at the controls on the spatial variability of melting SGI. The results from this study show that while spatially variable melting certainly can occur, the timing of ice-free conditions is impacted more so by how much ice forms, i.e. SGI thickness. Furthermore, the spatially variable melting did not have an impact on site scale evapotranspiration, as the biggest control for that was the energy inputs. This helps simplify the approach when it comes to modelling SGI. Multiple model domains are not needed to account for SGI heterogeneity but can be represented in the model by a single site average, although caution is still suggested, as not all peatlands may behave this way.

While chapter 2 showed that ice thickness appeared to be the main control on the timing of when an area becomes ice free, the impacts of bi-directional melt were also explored. As SGI melts, unfrozen ground water beneath the SGI layer can also contribute energy, enhancing melting, and the timing of ice-free conditions. Using a bi-directional melt approach with the Stefan's equation,

it was shown, that incorporating bi-directional melt improves model timing of ice-free conditions. This suggests that the inclusion of bi-directional melt in future boreal peatland models be encouraged. A climate sensitivity was also completed to answer a question posed in chapter 2; how climate change impact might the role of SGI. The findings here suggest that as the climate warms, there will be a thinning of SGI, more frequent freeze/thaw periods where SGI completely melts. If we apply this scenario to the original conceptual role of SGI, it suggests that their role as water sources within the landscape may become less reliable. With less SGI present in the spring, the spring freshet may become more temporally variable. Such a scenario could lead to drier peatlands in the spring, making them more vulnerable to wildfire and carbon losses.

The final chapter worked to evaluate how best to model peatland evaporation, and SGI. This particular CRHM model incorporated the energy reducing effects of melting SGI on available energy and tested out both Priestley Taylor and Penman-Monteith methods of estimating site scale evapotranspiration. In addition, a first attempt at incorporating moss resistance into the Penman-Monteith equation was proposed. This study found that if a peatland is assumed to evaporate at potential rates, there will likely be overestimations in the model, as both moss and vascular species will experience periods where resistance to evaporation is higher. However, when modelling this resistance, there is a large degree of uncertainty around moss resistance. While the theory behind how to conceptualize moss resistance is sound, more work is needed to better understand its role in peatland AET, and how best to incorporate it into future modelling studies.

Based on this work, there are several recommendations that can be made. First, SGI should be incorporated into future models that include peatlands, to better represent these systems in larger scale models. Second, more research is needed into how to represent moss evaporation. The large uncertainties around estimating moss resistance remain and are further complicated by the differing *Sphagnum* species that can be found along with microtopographic forms in peatlands. While this study provides a solid baseline understanding of the ecohydrological role of SGI in peatlands, there is clearly more work to be done. This work can be built upon by future peatland ecohydrological researchers as we work towards better modelling approaches, and ultimately a more wholistic understanding of peatland ecohydrology.

References

Adams, & Barr. (1974). Techniques and equipment for measurement of snowcover, including stratigraphy. *Trent University Department of Geography Occasional Papers*, *3*, 11–26.

Alves, I., & Santos Pereira, L. (2000). Modelling surface resistance from climatic variables? *Agricultural Water Management*, *42*(3), 371–385. https://doi.org/10.1016/S0378-3774(99)00041-4

Anselin, L. (1995). Local Indicators of Spatial Association-LISA. *Geographical Analysis*, *27*(2).

Appels, W. M., Coles, A. E., & McDonnell, J. J. (2018). Infiltration into frozen soil: From core-scale dynamics to hillslope-scale connectivity. *Hydrological Processes*, *32*(1), 66–79. https://doi.org/10.1002/hyp.11399

Baird, A. J., Belyea, L. R., & Morris, P. J. (2013). Upscaling of Peatland-Atmosphere Fluxes of Methane: Small-Scale Heterogeneity in Process Rates and the Pitfalls of "Bucket-and-Slab" Models. In A.J. Baird, L. R. Belyea, X. Comas, A. S. Reeve, & L. D. Slater (Eds.), *Carbon Cycling in Northern Peatlands* (pp. 37–53). American Geophysical Union. https://doi.org/10.1029/2008GM000826

Baird, Andy J., Milner, A. M., Blundell, A., Swindles, G. T., & Morris, P. J. (2016). Microform-scale variations in peatland permeability and their ecohydrological implications. *Journal of Ecology*, *104*(2), 531–544. https://doi.org/10.1111/1365-2745.12530

Balliston, N. E., & Price, J. S. (2020). Heterogeneity of the peat profile and its role in unsaturated sodium chloride rise at field and laboratory scales. *Vadose Zone Journal*, *19*(1), 1–15. https://doi.org/10.1002/vzj2.20015

Barbour, S. L., & Krahn, J. (2004). Numerical Modelling – Prediction or Process? *Geotechnical News*, *22*(4), 44–52.

Becker, T., Kutzbach, L., Forbrich, I., Schneider, J., Jager, D., Thees, B., & Wilmking, M. (2008). Do we miss the hot spots? - The use of very high resolution aerial photographs to quantify carbon fluxes in peatlands. *Biogeosciences*, *5*(5), 1387–1393. https://doi.org/10.5194/bg-5-1387-2008

Berglund, E. R., & Mace, A. C. (1972). Seasonal Albedo Variation of Black Spruce and Sphagnum-Sedge Bog Cover Types. *Journal of Applied Meteorology*, *11*(5), 806–812. https://doi.org/10.1175/1520-0450(1972)011<0806:savobs>2.0.co;2

Bocking, E., Cooper, D. J., & Price, J. (2017). Using tree ring analysis to determine impacts of a road on a boreal peatland. *Forest Ecology and Management*, *404*(April), 24–30. https://doi.org/10.1016/j.foreco.2017.08.007

Boelter, D. H. (1969). Physical Properties of Peats as Related to Degree of Decomposition. *Proceedings of American Soil Science Society*, *33*, 606–609.

Bond-lamberty, B., Gower, S. T., Amiro, B., & Ewers, B. E. (2010). Measurement and modelling of bryophyte evaporation in a boreal forest chronosequence. *Ecohydrology*. https://doi.org/10.1002/eco.118

Bowling, L. C., Kane, D. L., Gieck, R. E., Hinzman, L. D., & Lettenmaier, D. P. (2003). The role of surface storage in a low-gradient Arctic watershed. *Water Resources Research*, *39*(4), 1–13. https://doi.org/10.1029/2002WR001466

Brown, S. M., Petrone, R. M., Chasmer, L., Mendoza, C., Lazerjan, M. S., Landh??usser, S. M., Silins, U., Leach, J., & Devito, K. J. (2014). Atmospheric and soil moisture controls on evapotranspiration from above and within a Western Boreal Plain aspen forest. *Hydrological Processes*, *28*(15), 4449–4462. https://doi.org/10.1002/hyp.9879

Brown, S. M., Petrone, R. M., Mendoza, C., & Devito, K. J. (2010). Surface vegetation controls on evapotranspiration from a sub-humid Western Boreal Plain wetland. *Hydrological Processes*, *24*(8), 1072–1085. https://doi.org/10.1002/hyp.7569

Brown, Scott M. (2010). *Controls on Terrestrial Evapotranspiration from a Forest-Wetland Complex in the Western Boreal Plain, Alberta, Canada*. Wilfrid Laurier University.

Buermann, W., Bikash, P. R., Jung, M., Burn, D. H., & Reichstein, M. (2013). Earlier springs decrease peak summer productivity in North American boreal forests. *Environmental Research Letters*, *8*(2). https://doi.org/10.1088/1748-9326/8/2/024027

Burba, G., Schmidt, A., Scott, R. L., Nakai, T., Kathilankal, J., Fratini, G., Hanson, C., Law, B., Mcdermitt, D. K., Eckles, R., Furtaw, M., & Velgersdyk, M. (2012). Calculating CO 2 and H 2O eddy covariance fluxes from an enclosed gas analyzer using an instantaneous mixing ratio. *Global Change Biology*, *18*(1), 385–399. https://doi.org/10.1111/j.1365-2486.2011.02536.x

Bush, E., & Lemmen, D. S. (2019). *Canada's Changing Climate Report*. http://www.changingclimate.ca/CCCR2019

Carey, S. K., & Woo, M. (2000). Within-slope variability of ground heat flux, subarctic Yukon. *Physical Geography*, *21*(5), 407–417. https://doi.org/10.1080/02723646.2000.10642717

Cheng, G., & Chamberlain, E. J. (1988). Observations of moisture migration in frozen soils during thawing. *Canadian Geotechnical Journal*, *17*, 54–60. https://doi.org/10.1139/t80-005

Clymo, R. S. (1973). The Growth of Sphagnum : Some Effects of Environment THE GROWTH OF SPHAGNUM : SOME EFFECTS OF ENVIRONMENT. *Journal of Ecology*, *61*(3), 849–869.

Connon, R., Devoie, E., Hayashi, M., Veness, T., & Quinton, W. (2018). The Influence of Shallow Taliks on Permafrost Thaw and Active Layer Dynamics in Subarctic Canada. *Journal of Geophysical Research : Earth Surface*, *123*(2), 281–297. https://doi.org/10.1002/2017JF004469

Connon, R. F., Quinton, W. L., Craig, J. R., Hanisch, J., & Sonnentag, O. (2015). The hydrology of interconnected bog complexes in discontinuous permafrost terrains. *Hydrological Processes*, *29*(18), 3831–3847. https://doi.org/10.1002/hyp.10604

Connon, Ryan F., Quinton, W. L., Craig, J. R., & Hayashi, M. (2014). Changing hydrologic connectivity due to permafrost thaw in the lower Liard River valley, NWT, Canada. *Hydrological Processes*, *28*(14), 4163–4178. https://doi.org/10.1002/hyp.10206

Davidson, S. J., Elmes, M. C., Rogers, H., van Beest, C., Petrone, R., Price, J. S., & Strack, M. (2019). Hydrogeologic setting overrides any influence of wildfire on pore water dissolved organic carbon concentration and quality at a boreal fen. *Ecohydrology*, *12*(7), 1–11. https://doi.org/10.1002/eco.2141

Davidson, S. J., Santos, M. J., Sloan, V. L., Reuss-Schmidt, K., Phoenix, G. K., Oechel, W. C., & Zona, D. (2017). Upscaling CH4 fluxes using high-resolution imagery in Arctic Tundra ecosystems. *Remote Sensing*, *9*(12), 1–21. https://doi.org/10.3390/rs9121227

Davidson, S. J., Santos, M. J., Sloan, V. L., Watts, J. D., Phoenix, G. K., Oechel, W. C., & Zona, D. (2016). Mapping arctic tundra vegetation communities using field spectroscopy and multispectral satellite data in North Alaska, USA. *Remote Sensing*, *8*(12). https://doi.org/10.3390/rs8120978

DeBeer, C., Wheater, H., Pomeroy, J., Barr, A., Baltzer, J., Johnstone, J., Turetsky, M., Stewart, R., Hayashi, M., van der Kamp, G., Marshall, S., Campbell, E., Marsh, P., Carey, S.,

Quinton, W., Li, Y., Razavi, S., Berg, A., McDonnell, J., … Pietroniro, A. (2020). Summary and synthesis of Changing Cold Regions Network (CCRN) research in the interior of western Canada – Part 2: Future change in cryosphere, vegetation, and hydrology. *Hydrology and Earth System Sciences Discussions*, *September 2020*, 1–48. https://doi.org/10.5194/hess-2020-491

Depante, M., Morison, M. Q., Petrone, R. M., Devito, K. J., Kettridge, N., & Waddington, J. M. (2019). Hydraulic redistribution and hydrological controls on aspen transpiration and establishment in peatlands following wildfire. *Hydrological Processes*, *33*(21), 2714–2728. https://doi.org/10.1002/hyp.13522

Devito, K. J., Creed, I. F., & Fraser, C. J. D. (2005). Controls on runoff from a partially harvested aspen-forested headwater catchment, Boreal Plain, Canada. *Hydrological Processes*, *19*(1), 3–25. https://doi.org/10.1002/hyp.5776

Devoie, É. G., & Connon, R. F. (2019). *Taliks : A Tipping Point in Discontinuous Permafrost Degradation in Peatlands*. *2002*, 9838–9857. https://doi.org/10.1029/2018WR024488

Drever, C. R., Cook-Patton, S. C., Akhter, F., Badiou, P. H., Chmura, G. L., Davidson, S. J., Desjardins, R. L., Dyk, A., Fargione, J. E., Fellows, M., Filewod, B., Hessing-Lewis, M., Jayasundara, S., Keeton, W. S., Kroeger, T., Lark, T. J., Le, E., Leavitt, S. M., LeClerc, M.-E., … Kurz, W. A. (2020). Natural Climate Solutions for Canada. *In Review*, *June*, 1–14.

Drexler, J. Z., Snyder, R. L., Spano, D., & Paw U, K. T. (2004). A review of models and micrometeorological methods used to estimate wetland evapotranspiration. *Hydrological Processes*, *18*(11), 2071–2101. https://doi.org/10.1002/hyp.1462

Dyson, K. E., Billett, M. F., Dinsmore, K. J., Harvey, F., Thomson, A. M., Piirainen, S., & Kortelainen, P. (2011). Release of aquatic carbon from two peatland catchments in E. Finland during the spring snowmelt period. *Biogeochemistry*, *103*(1), 125–142. https://doi.org/10.1007/s10533-010-9452-3

Elliott, J., & Price, J. (2020). Comparison of soil hydraulic properties estimated from steady-state experiments and transient field observations through simulating soil moisture in regenerated Sphagnum moss. *Journal of Hydrology*, *582*(July 2019), 124489. https://doi.org/10.1016/j.jhydrol.2019.124489

Elmes, M. C., & Price, J. S. (2019). Hydrologic function of a moderate-rich fen watershed in the Athabasca Oil Sands Region of the Western Boreal Plain , northern Alberta. *Journal of Hydrology*, *570*(October 2018), 692–704. https://doi.org/10.1016/j.jhydrol.2018.12.043

Elmes, M. C., Thompson, D. K., Sherwood, J. H., & Price, J. S. (2017). Hydrometeorological conditions preceding wildfire , and the subsequent burning of a fen watershed in Fort McMurray , Alberta , Canada. *Natural Hazards and Earth System Sciences*, *September*, 1–37. https://doi.org/https://doi.org/10.5194/nhess-2017-312

Elmes, M., Thompson, D., Sherwood, J., & Price, J. (2018). Hydrometeorological conditions preceding wildfire , and the subsequent burning of a fen watershed in Fort McMurray, Alberta, Canada. *Natural Hazards and Earth System Sciences*, *18*, 157–170.

ESRI. (2016). *Points Solar Radiation*. https://desktop.arcgis.com/en/arcmap/10.3/tools/spatial-analyst-toolbox/points-solar-radiation.htm

Famiglietti, J. S., & Wood, E. F. (1995). Effects of Spatial Variability and Scale on Areally Averaged Evapotranspiration. *Water Resources Research*, *31*(3), 699–712. https://doi.org/10.1029/94WR02820

Farouki, O. T. (1981). Thermal properties of soils. In *Physics of Plant Environment, 2nd Ed.* United States Army Corps of Engineers. https://doi.org/10.4236/ojss.2011.13011

FitzGibbon, J. E. (1981). Thawing of seasonally frozen ground in organic terrain in central Saskatchewan. *Canadian Journal of Earth Sciences*, *18*(9), 1492–1496. http://www.nrcresearchpress.com/doi/pdf/10.1139/e81-139

Flerchinger, G. N., & Saxton, K. E. (1989). Simultaneous Heat and Water Model of a Freezing Snow-Residue-Soil System I. Theory and Development. *American Society of Agricultural and Biological Engineers*, *32*(2), 0565–0571. https://doi.org/10.13031/2013.31040

Foken, T. (2009). *Micro-meterology* (C. J. Nappo (ed.)). Springer.

Friesen, H. C., Slesak, R. A., Karwan, D. L., & Kolka, R. K. (2021). Effects of snow cover manipulation and climate factors on the development of soil frost in forested boreal peatlands in Minnesota, USA. *Geoderma*, *394*(February), 115015. https://doi.org/10.1016/j.geoderma.2021.115015

Fu, P., & Rich, P. M. (2002). A geometric solar radiation model with applications in agriculture and forestry. *Computer and Electronics in Agriculture*, *37*.

Gabrielli, E. C. (2016). *Partitioning Evapotranspiration in Forested Peatlands within the Western Boreal Plain , Fort McMurray, Alberta, Canada*. Wilfird Laurier University.

Getis, A., & Ord, J. K. (1992). The Analysis of Spatial Association by Use of Distance Statistics. *Geographical Analysis*, *24*(3), 186–206.

Goetz, J. D., & Price, J. S. (2015). Role of morphological structure and layering of *Sphagnum* and *Tomenthypnum* mosses on moss productivity and evaporation rates. *Canadian Journal of Soil Science*, *95*(2), 109–124. https://doi.org/10.4141/cjss-2014-092

Goetz, J. D., & Price, J. S. (2016). Ecohydrological controls on water distribution and productivity of moss communities in western boreal peatlands, Canada. *Ecohydrology*, *9*(1), 138–152. https://doi.org/10.1002/eco.1620

Gong, J., Wang, K., Kellomäki, S., Zhang, C., Martikainen, P. J., & Shurpali, N. (2012a). Modeling water table changes in boreal peatlands of Finland under changing climate conditions. *Ecological Modelling*, *244*, 65–78. https://doi.org/10.1016/j.ecolmodel.2012.06.031

Gong, J., Wang, K., Kellomäki, S., Zhang, C., Martikainen, P. J., & Shurpali, N. (2012b). Modeling water table changes in boreal peatlands of Finland under changing climate conditions. *Ecological Modelling*, *244*, 65–78. https://doi.org/10.1016/j.ecolmodel.2012.06.031

Goodbrand, A., Westbrook, C. J., & van der Kamp, G. (2018). Hydrological Functions of a Peatland in a Boreal Plains Catchment. *Hydrological Processes*. https://doi.org/10.1002/hyp.13343

Gorham, E. (1991). Northern peatlands: Role in the carbon cycle and probably responses to climate warming. *Ecological Applications*, *1*(2), 182–195. https://doi.org/10.2307/1941811

Granger, R. J. (1989). An Examination of the Concept of potential evaporation. *Journal of Hydrology*, *111*(1–4), 9–19. https://doi.org/https://doi.org/10.1016/0022-1694(89)90248-5

Granger, R. J., & Gray, D. M. (1989). Evaporation from Natural Nonsaturated Surfaces. *Journal of Hydrology*, *111*, 21–29.

Granger, R. J., Gray, D. M., & Dyck, G. E. (1984). Snowmelt infiltration to frozen Prairie soils. *Canadian Journal of Earth Sciences*, *21*(6), 669–677. https://doi.org/10.1139/e84-073

Gray, D. M., & Landine, P. G. (1987). Albedo model for shallow prairie snow covers. *Canadian Journal of Earth Sciences*, *24*(9), 1760–1768. https://doi.org/10.1139/e87-168

Gray, D. M., & Landine, P. G. (1988). An energy-budget snowmelt model for the Canadian Prairies. *Canadian Journal of Earth Sciences*, *25*(8), 1292–1303.

https://doi.org/10.1139/e88-124

Gray, D. M., Toth, B., Zhao, L., Pomeroy, J. W., & Granger, R. J. (2001). Estimating areal snowmelt infiltration into frozen soils. *Hydrological Processes*, *3111*(July 2000), 3095–3111. https://doi.org/10.1002/hyp.320

Halliwell, D. H., & Rouse, W. R. (1987). Soil Heat Flux in Permafrost: Characteristics and Accuracy of Measurement. *Journal of Climatology*, *7*(6), 571–584. https://doi.org/10.1002/joc.3370070605

Halsey, L. A., Vitt, D. H., & Gignac, L. D. (2000). Sphagnum-Dominated Peatlands in North America since the Last Glacial Maximum : Their Occurrence and Extent Sphagnum-dominated Peatlands in North America Since the Last Glacial Maximum : Their Occurrence and Extent. *The Bryologist*, *103*(2), 334–352.

Hayashi, M. (2013). The Cold Vadose Zone: Hydrological and Ecological Significance of Frozen-Soil Processes. *Vadose Zone Journal*, *12*(4). https://doi.org/10.2136/vzj2013.03.0064

Hayashi, M., Goeller, N., Quinton, W., & Wright, N. (2007). A simple heat conduction method for simulating the frost-table depth in hydrological models. *Hydrological Processes*, *21*(19), 2610–2622. https://doi.org/10.1002/hyp

Hayward, P. M., & Clymo, R. S. (1982). Profiles of Water Content and Pore Size in Sphagnum and Peat, and their Relation to Peat Bog Ecology. *Proceedings of the Royal Society B: Biological Sciences*, *215*(1200), 299–325. https://doi.org/10.1098/rspb.1982.0044

Hedstrom, N. R., & Pomeroy, J. W. (1998). Measurements and modelling of snow interception in the boreal forest. *Hydrological Processes*, *12*(10–11), 1611–1625. https://doi.org/10.1002/(SICI)1099-1085(199808/09)12:10/11<1611::AID-HYP684>3.0.CO;2-4

Helbig, M., Waddington, J. M., Alekseychik, P., Amiro, B. D., Aurela, M., Barr, A. G., Black, T. A., Blanken, P. D., Carey, S. K., Chen, J., Chi, J., Desai, A. R., Dunn, A., Euskirchen, E. S., Flanagan, L. B., Forbrich, I., Friborg, T., Grelle, A., Iwata, H., … Strachan, I. B. (2020). Increasing contribution of peatlands to boreal evapotranspiration in a warming climate. *Nature Climate Change*. https://doi.org/10.1038/s41558-020-0763-7

Hugelius, G., Loisel, J., Chadburn, S., Jackson, R. B., Jones, M., MacDonald, G., Marushchak, M., Olefeldt, D., Packalen, M., Siewert, M. B., Treat, C., Turetsky, M., Voigt, C., & Yu, Z. (2020). Large stocks of peatland carbon and nitrogen are vulnerable to permafrost thaw. *Proceedings of the National Academy of Sciences of the United States of America*, *117*(34), 20438–20446. https://doi.org/10.1073/pnas.1916387117

Hwang, H. T., Park, Y. J., Sudicky, E. A., Berg, S. J., McLaughlin, R., & Jones, J. P. (2018). Understanding the water balance paradox in the Athabasca River Basin, Canada. *Hydrological Processes*, *32*(6), 729–746. https://doi.org/10.1002/hyp.11449

Ireson, A. M., Barr, A. G., Johnstone, J. F., Mamet, S. D., van der Kamp, G., Whitfield, C. J., Michel, N. L., North, R. L., Westbrook, C. J., DeBeer, C., Chun, K. P., Nazemi, A., & Sagin, J. (2015). The changing water cycle: the Boreal Plains ecozone of Western Canada. *Wiley Interdisciplinary Reviews: Water*, *2*(5), 505–521. https://doi.org/10.1002/wat2.1098

Ireson, A. M., van der Kamp, G., Ferguson, G., Nachshon, U., & Wheater, H. S. (2013). Hydrogeological processes in seasonally frozen northern latitudes: understanding, gaps and challenges. *Hydrogeology Journal*, *21*(1), 53–66. https://doi.org/10.1007/s10040-012-0916-5

Iwata, Y., Hayashi, M., Suzuki, S., Hirota, T., & Hasegawa, S. (2010). Effects of snow cover on

soil freezing, water movement, and snowmelt infiltration: A paired plot experiment. *Water Resources Research*, *46*(9), 1–11. https://doi.org/10.1029/2009WR008070

Jansson, P. E., & Moon, D. S. (2001). A coupled model of water, heat and mass transfer using object orientation to improve flexibility and functionality. *Environmental Modelling and Software*, *16*(1), 37–46. https://doi.org/10.1016/S1364-8152(00)00062-1

Jarvis, P. G. (1976). The interpretation of the variations in leaf water potential and stomatal conductance found in canopies in the field. *Philosophical Transactions of the Royal Society of London. B, Biological Sciences*, *273*(927), 593–610. https://doi.org/10.1098/rstb.1976.0035

Jarvis, P., Massheder, J. M., Hale, S. E., Moncrieff, J. B., Rayment, M., & Scott, S. L. (1997). Seasonal variation of carbon dioxide, water vapor, and energy exchanges of a boreal black spruce forest. *Journal of Geophysical Research*, *102*(97), 28,953-28,966. https://doi.org/10.1029/97JD01176

Jiang, R., Gan, T. Y., Xie, J., Wang, N., & Kuo, C. (2017). Historical and potential changes of precipitation and temperature of Alberta subjected to climate change impact : 1900 – 2100. *Theoretical and Applied Climatology*, *127*, 725–739. https://doi.org/10.1007/s00704-015-1664-y

Jones, M., Castonguay, M., Nasr, M., Ogilvie, J., & Arp, P. A. (2014). Modeling hydrothermal regimes and potential impacts of climate change on permafrost within the South Mackenzie Plain, Northwest Territories, Canada. *Ecoscience*, *21*(1), 21–33. https://doi.org/10.2980/21-1-3663

Jumikis, A. R. (1977). Thermal Geotechnics. In *Thermal Geotechnics* (p. 131). Rutgers.

Kaimal, J. C., & Finnigan, J. J. (1994). *Atmospheric Boundary Layer Flows: Their Structure and Measurement*. Oxford University Press.

Kellner, E. (2001). Surface energy fluxes and control of evapotranspiratoin from a Swedish Sphagnum mire. *Agricultural and Forest Meteorology*, *110*, 101–123. https://doi.org/10.1016/S0168-1923(01)00283-0

Kennedy, G. W., & Price, J. S. (2005). A conceptual model of volume-change controls on the hydrology of cutover peats. *Journal of Hydrology*, *302*(1–4), 13–27. https://doi.org/10.1016/j.jhydrol.2004.06.024

Kettridge, N., Thompson, D. K., Bombonato, L., Turetsky, M. R., Benscoter, B. W., & Waddington, J. M. (2013). The ecohydrology of forested peatlands: Simulating the effects of tree shading on moss evaporation and species composition. *Journal of Geophysical Research: Biogeosciences*, *118*(2), 422–435. https://doi.org/10.1002/jgrg.20043

Kettridge, N., Tilak, A. S., Devito, K. J., Petrone, R. M., Mendoza, C. A., & Waddington, J. M. (2016). Moss and peat hydraulic properties are optimized to maximize peatland water use efficiency. *Ecohydrology*, *9*(6), 1039–1051. https://doi.org/10.1002/eco.1708

Kettridge, Nicholas, Lukenbach, M. C., Hokanson, K. J., Devito, K. J., Petrone, R. M., Mendoza, C. A., & Waddington, J. M. (2021). Regulation of peatland evaporation following wildfire; the complex control of soil tension under dynamic evaporation demand. *Hydrological Processes*, *35*(4), 1–15. https://doi.org/10.1002/hyp.14132

Kettridge, Nicholas, & Waddington, J. M. (2014). Towards quantifying the negative feedback regulation of peatland evaporation to drought. *Hydrological Processes*, *28*(11), 3728–3740. https://doi.org/10.1002/hyp.9898

Kim, J., & Verma, S. B. (1996). Surface exchange of water vapour between an open sphagnum fen and the atmosphere. *Boundary-Layer Meteorology*, *79*(3), 243–264.

https://doi.org/10.1007/BF00119440

Kingsbury, C. M., & Moore, T. R. (1987). The freeze-thaw cycle of a subarctic fen, northern Quebec, Canada. *Arctic and Alpine Research*, *19*(3), 289–295.

Kleinen, T., Brovkin, V., & Schuldt, R. J. (2012). A dynamic model of wetland extent and peat accumulation: Results for the Holocene. *Biogeosciences*, *9*(1), 235–248. https://doi.org/10.5194/bg-9-235-2012

Kljun, N., Calanca, P., Rotach, M. W., & Schmid, H. P. (2004). A Simple Parameterisation for Flux Footprint Predictions. *Boundary-Layer Meterology*, *112*(3), 503–523. https://doi.org/10.1023/B

Korrensalo, A., Männistö, E., Alekseychik, P., Mammarella, I., Rinne, J., Vesala, T., & Tuittila, E.-S. (2017). Small spatial but large sporadic variability in methane emission measured from a patterned boreal bog. *Biogeosciences Discussions*, 1–35. https://doi.org/10.5194/bg-2017-443

Krogh, S. A., Pomeroy, J. W., & Marsh, P. (2017). Diagnosis of the hydrology of a small Arctic basin at the tundra-taiga transition using a physically based hydrological model. *Journal of Hydrology*, *550*, 685–703. https://doi.org/10.1016/j.jhydrol.2017.05.042

Kujala, K., Seppälä, M., & Holappa, T. (2008). Physical properties of peat and palsa formation. *Cold Regions Science and Technology*, *52*(3), 408–414. https://doi.org/10.1016/j.coldregions.2007.08.002

Kurylyk, B. L. (2015). Discussion of "A Simple Thaw-Freeze Algorithm for a Multi-Layered Soil using the Stefan Equation" by Xie and Gough (2013). *Permafrost and Periglacial Processes*, *26*(2), 200–206. https://doi.org/10.1002/ppp.1834

Kurylyk, B. L., & Hayashi, M. (2016). Improved Stefan Equation Correction Factors to Accommodate Sensible Heat Storage during Soil Freezing or Thawing. *Permafrost and Periglacial Processes*, *27*(2), 189–203. https://doi.org/10.1002/ppp.1865

Kurylyk, B. L., Hayashi, M., Quinton, W., McKenzie, J. M., & Voss, C. I. (2016). Influence of vertical and lateral heat transfer on permafrost thaw, peatland landscape transition, and groundwater flow. *Journal of the American Water Resources Association*, *52*, 1286–1305. https://doi.org/10.1111/j.1752-1688.1969.tb04897.x

Kurylyk, B. L., & Watanabe, K. (2013). The mathematical representation of freezing and thawing processes in variably-saturated, non-deformable soils. *Advances in Water Resources*, *60*, 160–177. https://doi.org/10.1016/j.advwatres.2013.07.016

Lafleur, P. M., Hember, R. A., Admiral, S. W., & Roulet, N. T. (2005). Annual and seasonal variability in evapotranspiration and water table at a shrub-covered bog in southern Ontario, Canada. *Hydrological Processes*, *19*(18), 3533–3550. https://doi.org/10.1002/hyp.5842

Lafleur, P. M., McCaughey, J. H., Joiner, D. W., Bartlett, P. A., & Jelinski, D. E. (1997). Seasonal trends in energy, water, and carbon dioxide fluxes at a northern boreal wetland. *Journal of Geophysical Research: Atmospheres*, *102*(24), 29009–29020. https://doi.org/10.1029/96JD03326

Lamontagne-Hallé, P., McKenzie, J. M., Kurylyk, B. L., Molson, J., & Lyon, L. N. (2020). Guidelines for cold-regions groundwater numerical modeling. *Wiley Interdisciplinary Reviews: Water*, *7*(6), 1–26. https://doi.org/10.1002/wat2.1467

Lawton, J. H., & Brown, V. K. (1994). Redundancy in Ecosystems. In E.-D. Schulze & H. A. Mooney (Eds.), *Biodiversity and Ecosystem Function* (pp. 238-). Elsevier.

Lewis, A. N. N. M. (1988). A Test of the Air-Seeding Hypothesis Using Sphagnum Hyalocysts. *Plant Physiology*, *87*(3), 577–582. https://www-jstor-

org.proxy.lib.uwaterloo.ca/action/doBasicSearch?Query=%22A+test+of+the+air-seeding+hypothesis+using+sphagnum+hyalocysts.%22

Lunardini, V. J. (1981). *Heat Transfer in Cold Climates*. Van Nostrand Reinhold Ltd.

Marshall, I., Schut, P., & Ballard, M. (1999). *Canadian ecodistrict climate normals for Canada 1961-1990*. Environment Canada.

Mbogga, M. S., Wang, T., & Hamann, A. (2010). A comprehensive set of interpolated climate data for Alberta. In *Government of Alberta. Department of Renewable Resources EFM Research Note 01/2010.* https://doi.org/ISBN No. 978-0-7785-9183-2

McCarter, C. P. R., & Price, J. S. (2014). Ecohydrology of Sphagnum moss hummocks: Mechanisms of capitula water supply and simulated effects of evaporation. *Ecohydrology*, *7*(1), 33–44. https://doi.org/10.1002/eco.1313

McClymont, A. F., Hayashi, M., Bentley, L. R., & Christensen, B. S. (2013). Geophysical imaging and thermal modeling of subsurface morphology and thaw evolution of discontinuous permafrost. *Journal of Geophysical Research: Earth Surface*, *118*(3), 1826–1837. https://doi.org/10.1002/jgrf.20114

McKenzie, J. M., Siegel, D. I., Rosenberry, D. O., Glaser, P. H., & Voss, C. I. (2007). Heat transport in the Red Lake Bog, Glacial Lake Agassiz Peatlands. *Hydrological Processes*, *21*, 369–378. https://doi.org/10.1002/hyp.6239

McKenzie, J. M., Voss, C. I., & Siegel, D. I. (2007). Groundwater flow with energy transport and water-ice phase change: Numerical simulations, benchmarks, and application to freezing in peat bogs. *Advances in Water Resources*, *30*(4), 966–983. https://doi.org/10.1016/j.advwatres.2006.08.008

Mohammed, A. A., Kurylyk, B. L., Cey, E. E., & Hayashi, M. (2018). Snowmelt Infiltration and Macropore Flow in Frozen Soils: Overview, Knowledge Gaps, and a Conceptual Framework. *Vadose Zone Journal*, *17*(1), 0. https://doi.org/10.2136/vzj2018.04.0084

Monteith, J. L. (1965). Evaporation and Environment. *Symposia of the Society for Experimental Biology*, 205–234.

Moore, T. R. (1987). Thermal regime of peatlands in subarctic eastern Canada. *Canadian Journal of Earth Sciences*, *24*(7), 1352–1359. https://doi.org/10.1139/e87-129

Moore, Tim R., Lafleur, P. M., Poon, D. M. I., Heumann, B. W., Seaquist, J. W., & Roulet, N. T. (2006). Spring photosynthesis in a cool temperate bog. *Global Change Biology*, *12*(12), 2323–2335. https://doi.org/10.1111/j.1365-2486.2006.01247.x

Mualem, Y. (1976). A New Model for Predicting the Hydraulic Conductivity of Unsaturated Porous Media. *Water Resources Research*, *12*(3).

Murray, K. R., Barlow, N., & Strack, M. (2017). Methane emissions dynamics from a constructed fen and reference sites in the Athabasca Oil Sands Region, Alberta. *Science of The Total Environment*, *583*, 369–381. https://doi.org/10.1016/j.scitotenv.2017.01.076

Nagare, R. M., Schincariol, R. A., Quinton, W. L., & Hayashi, M. (2012). Effects of freezing on soil temperature , freezing front propagation and moisture redistribution in peat : laboratory investigations. *Hydrology and Earth System Sciences*, *16*, 501–515. https://doi.org/10.5194/hess-16-501-2012

National Wetlands Working Group. (1997). The Canadian wetland classification system. In B. G. Warner & C. D. . Rubec (Eds.), *National Wetlands Working Group* (2nd ed.). https://doi.org/10.1002/1521-3773(20010316)40:6<9823::AID-ANIE9823>3.3.CO;2-C

Nijp, J. J., Metselaar, K., Limpens, J., Bartholomeus, H. M., Nilsson, M. B., Berendse, F., & van der Zee, S. E. A. T. M. (2019). High-resolution peat volume change in a northern peatland:

Spatial variability, main drivers, and impact on ecohydrology. *Ecohydrology*, *12*(6), 1–17. https://doi.org/10.1002/eco.2114

Nijp, J. J., Metselaar, K., Limpens, J., Teutschbein, C., Peichl, M., Nilsson, M. B., Berendse, F., & van der Zee, S. E. A. T. M. (2017). Including hydrological self-regulating processes in peatland models: Effects on peatmoss drought projections. *Science of the Total Environment*, *580*, 1389–1400. https://doi.org/10.1016/j.scitotenv.2016.12.104

O'Donnell, J. A., Romanovsky, V. E., Harden, J. W., & McGuire, A. D. (2009). The effect of moisture content on the thermal conductivity of moss and organic soil horizons from black spruce ecosystems in interior alaska. *Soil Science*, *174*(12), 646–651. https://doi.org/10.1097/SS.0b013e3181c4a7f8

Oke, T. R. (1987). *Boundary Layer Climates* (2nd ed.). Taylor & Francis.

Outcalt, S. I., Arbor, A., Nelson, F. E., & Hinkel, K. M. (1990). The Zero-Curtain Effect: Heat and Mass Transfer Across an Isothermal Region in Freezing Soil. *Water Resources Research*, *26*(7), 1509–1516.

Patankar, R., Quinton, W. L., Hayashi, M., & Baltzer, J. L. (2015). Sap flow responses to seasonal thaw and permafrost degradation in a subarctic boreal peatland. *Trees - Structure and Function*, *29*(1), 129–142. https://doi.org/10.1007/s00468-014-1097-8

Penman, H. L. (1948). Natural evaporation from open water, bare soil, and grass. *Royal Society of London Proceedings, Series A*, 120–145.

Petrone, R., Devito, K., Silins, U., Mendoza, C., Kaufman, S. C., & Price, J. S. (2008). Importance of seasonal frost to peat water storage: Western Boreal Plains, Canada. *Groundwater-Surface Water Interaction: Process Understanding, Conceptualization and Modelling (Proceedings of Symposium HS1002 at IUGG2007, Perugia, July 2007)*, *320*(July 2007), 61–66. http://www.cabdirect.org/abstracts/20093172603.html

Petrone, R. M., Chasmer, L., Hopkinson, C., Silins, U., Landhäusser, S. M., Kljun, N., & Devito, K. J. (2015). Effects of harvesting and drought on CO_2 and H_2O fluxes in an aspen-dominated western boreal plain forest: Early chronosequence recovery. *Canadian Journal of Forest Research*, *45*(1), 87–100. https://doi.org/10.1139/cjfr-2014-0253

Petrone, R. M., Devito, K. J., Silins, U., Mendoza, C., Brown, S. C., Kaufman, S. C., & Price, J. S. (2008). Transient peat properties in two pond-peatland complexes in the sub-humid Western Boreal Plain , Canada. *Mires and Peat*, *3*, 1–13.

Petrone, R. M., Silins, U., & Devito, K. J. (2007). Dynamics of evapotranspiration from a riparian pond complex in the Western Boreal Forest, Alberta, Canada. *Hydrological Processes*, *21*, 1391–1401. https://doi.org/10.1002/hyp.6298

Philip, J. R. (1957). Evaporation, and Moisture, and Heat Fields in the Soil. *Journal of Meteorology*, *14*, 354–366. https://doi.org/https://doi.org/10.1175/1520-0469(1957)014<0354:EAMAHF>2.0.CO;2

Phillips, T., Petrone, R. M., Wells, C. M., & Price, J. S. (2016). Characterizing dominant controls governing evapotranspiration within a natural saline fen in the Athabasca Oil Sands of Alberta, Canada. *Ecohydrology*, *9*(5), 817–829. https://doi.org/10.1002/eco.1685

Pomeroy, J. W., Gray, D. M., Brown, T., Hedstrom, N. R., Quinton, W. L., Granger, R. J., & Carey, S. K. (2007). The cold regions hydrological model: a platform for basing process representation and model structure on physical evidence. *Hydrological Processes*, *21*, 2650–2667. https://doi.org/10.1002/hyp.6787

Pomeroy, J. W., Toth, B., Granger, R. J., Hedstrom, N. R., Essery, R. L. H., Sciences, E., Kingdom, U., & Canada, E. (2003). Variation in Surface Energetics during Snowmelt in a

Subarctic Mountain Catchment. *Journal of Hydrometeorology*, *4*(4), 702–719. https://doi.org/10.1175/1525-7541(2003)004<0702:VISEDS>2.0.CO;2

Price, D. T., Alfaro, R. I., Brown, K. J., Flannigan, M. D., Fleming, R. A., Hogg, E. H., Girardin, M. P., Lakusta, T., Johnston, M., Mckenney, D. W., Pedlar, J. H., Stratton, T., Sturrock, R. N., Thompson, I. D., Trofymow, J. A., & Venier, L. A. (2013). *Anticipating the consequences of climate change for Canada 's boreal forest ecosystems 1*. *365*(December), 322–365. https://doi.org/dx.doi.org/10.1139/er-2013-0042

Price, J., & FitzGibbon, J. E. (1987). Groundwater storage - streamflow relations during winter in a subarctic wetland, Saskatchewan. *Canadian Journal of Earth Sciences*, *24*, 2074–2081.

Price, J. S. (1987). The Influence of weiland and Mineral rerrain Types on Snowmelt Runoff in the Subarctic. *Canadian Water Resources Journal*, *12*(2), 37–41. https://doi.org/10.4296/cwrj1202043

Price, J. S., & Whittington, P. N. (2010). Water flow in Sphagnum hummocks: Mesocosm measurements and modelling. *Journal of Hydrology*, *381*(3–4), 333–340. https://doi.org/10.1016/j.jhydrol.2009.12.006

Priestley, C. H. B., & Taylor, R. J. (1972). On the Assessment of Surface Heat Flux and Evaporation Using Large-Scale Parameters. *Monthly Weather Review*, *100*(2), 81–92. https://doi.org/10.1175/1520-0493(1972)100<0081:OTAOSH>2.3.CO;2

Quinton, W. L., & Baltzer, J. L. (2013). The active-layer hydrology of a peat plateau with thawing permafrost (Scotty Creek, Canada). *Hydrogeology Journal*, *21*(1), 201–220. https://doi.org/10.1007/s10040-012-0935-2

Quinton, W. L., Carey, S. K., & Goeller, N. T. (2004). Snowmelt runoff from northern alpine tundra hillslopes: major processes and methods of simulation. *Hydrology and Earth System Sciences*, *8*(5), 877–890. https://doi.org/10.5194/hess-8-877-2004

Quinton, W. L., Hayashi, M., & Pietroniro, A. (2003). Connectivity and storage functions of channel fens and flat bogs in northern basins. *Hydrological Processes*, *17*(18), 3665–3684. https://doi.org/10.1002/hyp.1369

Quinton, William L., & Baltzer, J. L. (2013). Changing surface water systems in the discontinuous permafrost zone: Implications for streamflow. *IAHS-AISH Proceedings and Reports*, *360*(July), 85–92.

R Core Team. (2020). *R: A language and environment for statistical computing.* R Foundation for Statistical Computing.

Raddatz, R. L., Papakyriakou, T. N., Swystun, K. A., & Tenuta, M. (2009). Evapotranspiration from a wetland tundra sedge fen: Surface resistance of peat for land-surface schemes. *Agricultural and Forest Meteorology*, *149*(5), 851–861. https://doi.org/10.1016/j.agrformet.2008.11.003

Redding, T., & Devito, K. (2011). Aspect and soil textural controls on snowmelt runoff on forested Boreal Plain hillslopes. *Hydrology Research*, *42*(4), 250. https://doi.org/10.2166/nh.2011.162

Redding, T. E., & Devito, K. J. (2005). Particle densities of wetland soils in northern Alberta, Canada. *Canadian Journal of Soil Science*, *1*(86), 57–60. https://doi.org/10.4141/S05-061

Riutta, T., Laine, J., Aurela, M., Rinne, J., Vesala, T., Laurila, T., Haapanala, S., Pihlatie, M., & Tuittila, E. S. (2007). Spatial variation in plant community functions regulates carbon gas dynamics in a boreal fen ecosystem. *Tellus, Series B: Chemical and Physical Meteorology*, *59*(5), 838–852. https://doi.org/10.1111/j.1600-0889.2007.00302.x

Romanov, V. V. (1968). *Hydrophysics of bogs*. Israel Programme for Scientific Translations.

Rooney, R. C., Bayley, S. E., & Schindler, D. W. (2012). Oil sands mining and reclamation cause massive loss of peatland and stored carbon. *Proceedings of the National Academy of Sciences of the United States of America*, *109*(13), 4933–4937. https://doi.org/10.1073/pnas.1

Roulet, N. T., Lafleur, P. M., Richard, P. J. H., Moore, T. R., Humphreys, E. R., & Bubier, J. (2007). Contemporary carbon balance and late Holocene carbon accumulation in a northern peatland. *Global Change Biology*, *13*(2), 397–411. https://doi.org/10.1111/j.1365-2486.2006.01292.x

Rouse, W. R. (1984). Microclimate of Arctic Tree Line 2. Microclimate of Tundra and Forest. *Water Resources Research*, *20*(1), 67–73. https://doi.org/https://doi.org/10.1029/WR020i001p00067

Rouse, W. R. (2000). The energy and water balance of high latitude wetlands: controls and extrapolation. *Global Change Biology*, *6*(S1), 59–68. https://doi.org/10.1046/j.1365-2486.2000.06013.x

Runkle, B. R. K., Wille, C., Gazovic, M., Wilmking, M., & Kutzbach, L. (2014). The surface energy balance and its drivers in a boreal peatland fen of northwestern Russia. *Journal of Hydrology*, *511*, 359–373. https://doi.org/10.1016/j.jhydrol.2014.01.056

Santeford, H. . (1978). Snow Soil Interactions in Interior Alaska. In S. C. Colbeck & M. Ray (Eds.), *Modeling of Snow Cover Runoff* (pp. 311–318). U.S. Army CRREL.

Scarlett, S. J., Petrone, R. M., & Price, J. S. (2017). Controls on plot-scale evapotranspiration from a constructed fen in the Athabasca Oil Sands Region, Alberta. *Ecological Engineering*, *100*, 199–210. https://doi.org/http://dx.doi.org/10.1016/j.ecoleng.2016.12.020

Schipperges, B., & Rydin, H. (1998). Response of photosynthesis of Sphagnum species from contrasting microhabitats to tissue water content and repeated desiccation. *New Phytologist*, *140*(4), 677–684. https://doi.org/10.1046/j.1469-8137.1998.00311.x

Shetler, G., Turetsky, M. R., Kane, E., & Kasischke, E. (2008). Sphagnum mosses limit total carbon consumption during fire in Alaskan black spruce forests. *Canadian Journal of Forest Research*, *38*(8), 2328–2336. https://doi.org/10.1139/X08-057

Sicart, J. E., Pomeroy, J. W., Essery, R. L. H., & Bewley, D. (2010). Incoming longwave radiation to melting snow: observations, sensitivity and estimation in northern environments. *Hydrological Processes*, *20*(17), 3697–3708. https://doi.org/10.1002/hyp

Smerdon, B. D., Mendoza, C. A., & Devito, K. J. (2008). Influence of subhumid climate and water table depth on groundwater recharge in shallow outwash aquifers. *Water Resources Research*, *44*(8), 1–15. https://doi.org/10.1029/2007WR005950

Smerdon, Brian D., & Mendoza, C. A. (2010). Hysteretic freezing characteristics of riparian peatlands in the Western Boreal forest of Canada. *Hydrological Processes*, *24*(8), 1027–1038. https://doi.org/10.1002/hyp.7544

Song-Miao Fan, Wofsy, S. C., Bakwin, P. S., Jacob, D. J., & Fitzjarrald, D. R. (1990). Atmosphere-biosphere exchange of CO2 and O3 in the central Amazon forest. *Journal of Geophysical Research*, *95*(D10), 851–864.

Stewart, J. B. (1988). Modelling surface conductance of pine forest. *Agricultural and Forest Meteorology*, *43*(1), 19–35. https://doi.org/10.1016/0168-1923(88)90003-2

Stiegler, C., Johansson, M., Christensen, T. R., Mastepanov, M., & Lindroth, A. (2016). Tundra permafrost thaw causes significant shifts in energy partitioning Tundra permafrost thaw causes significant shifts in energy partitioning. *Tellus B : Chemical and Physical Meteorology*, *68*(1). https://doi.org/10.3402/tellusb.v68.30467

Stone, L. E., Fang, X., Haynes, K. M., Helbig, M., Pomeroy, J. W., Sonnentag, O., & Quinton, W. L. (2019). Modelling the effects of permafrost loss on discharge from a wetland-dominated, discontinuous permafrost basin. *Hydrological Processes*, *33*(20), 2607–2626. https://doi.org/10.1002/hyp.13546

Strack, M., Waddington, J. M., & Tuittila, E. S. (2004). Effect of water table drawdown on northern peatland methane dynamics: Implications for climate change. *Global Biogeochemical Cycles*, *18*(4), 1–7. https://doi.org/10.1029/2003GB002209

Strack, M., Waller, M. F., & Waddington, J. M. (2006). Sedge succession and peatland methane dynamics: A potential feedback to climate change. *Ecosystems*, *9*(2), 278–287. https://doi.org/10.1007/s10021-005-0070-1

Sturm, M. (1992). Snow Distribution and Heat Flow in the Taiga. *Arctic and Alpine Research*, *24*(2), 145–152.

Sutton, O. F., & Price, J. S. (2020). Soil moisture dynamics modelling of a reclaimed upland in the early post-construction period. *Science of the Total Environment*, *718*, 134628. https://doi.org/10.1016/j.scitotenv.2019.134628

Talamucci, F. (2003). Freezing processes in porous media: Formation of ice lenses, swelling of the soil. *Mathematical and Computer Modelling*, *37*(5), 595–602. https://doi.org/10.1016/S0895-7177(03)00053-0

Tarnocai, C. (2009). The Impact of Climate Change on Canadian Peatlands. *Canadian Water Resources Journal*, *34*(4), 453–466. https://doi.org/10.4296/cwrj3404453

Team, R. C., & Contributors. (2020). *The R Stats Package* (4.0.3). R Foundation for Statistical Computing.

Thiessen, A. H. (1911). Precipitation Averages for Large Areas. *Monthly Weather Review*, *39*, 1082–1084.

Thompson, C., Mendoza, C. A., & Devito, K. J. (2017a). Potential influence of climate change on ecosystems within the Boreal Plains of Alberta. *Hydrological Processes*, *31*(11), 2110–2124. https://doi.org/10.1002/hyp.11183

Thompson, C., Mendoza, C. A., & Devito, K. J. (2017b). Potential influence of climate change on ecosystems within the Boreal Plains of Alberta. *Hydrological Processes*, *31*(11), 2110–2124. https://doi.org/10.1002/hyp.11183

Thompson, C., Mendoza, C. a., Devito, K. J., & Petrone, R. M. (2015). Climatic controls on groundwater–surface water interactions within the Boreal Plains of Alberta: Field observations and numerical simulations. *Journal of Hydrology*, *527*, 734–746. https://doi.org/10.1016/j.jhydrol.2015.05.027

Thompson, D. K., Baisley, A. S., & Waddington, J. M. (2015). Seasonal variation in albedo and radiation exchange between a burned and unburned forested peatland: Implications for peatland evaporation. *Hydrological Processes*, *29*(14), 3227–3235. https://doi.org/10.1002/hyp.10436

Thompson, D. K., & Waddington, J. M. (2013). Wildfire effects on vadose zone hydrology in forested boreal peatland microforms. *Journal of Hydrology*, *486*, 48–56. https://doi.org/10.1016/j.jhydrol.2013.01.014

Thornthwaite, C. W. (1948). An Approach toward a Rational Classification of Climate. *Geographical Review*, *38*(1), 55. https://doi.org/10.2307/210739

Todd, G. W. (1909). *Thermal Conductivity o f Air and other Gases.*

Turetsky, M. R., Donahue, W. F., & Benscoter, B. W. (2011). Experimental drying intensifies burning and carbon losses in a northern peatland. *Nature Communications*, *2*(1).

https://doi.org/10.1038/ncomms1523

van Everdingen, R. . (1975). Geocryological terminology. *Canadian Journal of Earth Sciences*, *13*, 862–867.

Van Huizen, B, Petrone, R. M., Price, J. S., Quinton, W. L., & Pomeroy, J. W. (2019). Seasonal Ground Ice Impacts on Spring Ecohydrological Conditions in a Western Boreal Plains Peatland. *Hydrological Processes*. https://doi.org/10.1002/hyp.13626

Van Huizen, Brandon, & Petrone, R. M. (2020). Quantifying the spatial variability of melting seasonal ground ice and its influence on potential evapotranspiration spatial variability in a boreal peatland. *Hydrological Processes*, *34*(17), 3683–3701. https://doi.org/10.1002/hyp.13840

Vaughan, D. G., Comiso, J. C., Allison, I., Carrasco, J., Kaser, G., Kwok, R., Mote, P., Murray, T., Paul, F., Ren, J., Rignot, E., Solomina, O., Steffen, K., & Zhang, T. (2013). Observations: Cryosphere. *Climate Change 2013: The Physical Science Basis. Contribution of Working Group I to the Fifth Assessment Report of the Intergovernmental Panel on Climate Change*, 317–382. https://doi.org/10.1017/CBO9781107415324.012

Volik, O., Kessel, E., Green, A., Petrone, R., & Price, J. (2020). Growing season evapotranspiration in boreal fens in the Athabasca Oil Sands Region: Variability and environmental controls. *Hydrological Processes*, *November 2020*, 1–17. https://doi.org/10.1002/hyp.14020

Waddington, J. M., Kellner, E., Strack, M., & Price, J. S. (2010). Differential peat deformation, compressibility, and water storage between peatland microforms: Implications for ecosystem function and development. *Water Resources Research*, *46*(7), 1–12. https://doi.org/10.1029/2009WR008802

Waddington, J. M., Morris, P. J., Kettridge, N., Granath, G., Thompson, D. K., & Moore, P. A. (2015). Hydrological feedbacks in northern peatlands. *Ecohydrology*, *8*(1), 113–127. https://doi.org/10.1002/eco.1493

Wang, Y., Hogg, E. H., Price, D. T., Edwards, J., & Williamson, T. (2014). Past and projected future changes in moisture conditions in the Canadian boreal forest. *The Forestry Chronicle*, *90*(June), 678–691. https://doi.org/https://doi.org/10.5558/tfc2014-134

Wania, R., Ross, L., & Prentice, I. C. (2009). Integrating peatlands and permafrost into a dynamic global vegetation model: 1. Evaluation and sensitivity of physical land surface processes. *Global Biogeochemical Cycles*, *23*(3), 1–19. https://doi.org/10.1029/2008GB003412

Warren, R. K., Pappas, C., Helbig, M., Chasmer, L. E., Berg, A. A., Baltzer, J. L., Quinton, W. L., & Sonnentag, O. (2018). Minor contribution of overstorey transpiration to landscape evapotranspiration in boreal permafrost peatlands. *Ecohydrology*, *11*(5), 1–10. https://doi.org/10.1002/eco.1975

Watanabe, K., Kito, T., Dun, S., Wu, J. Q., Greer, R. C., & Flury, M. (2013). Water Infiltration into a Frozen Soil with Simultaneous Melting of the Frozen Layer. *Vadose Zone Journal*, *12*(1), 0. https://doi.org/10.2136/vzj2011.0188

Wells, C., Ketcheson, S., & Price, J. (2017). Hydrology of a wetland-dominated headwater basin in the Boreal Plain, Alberta, Canada. *Journal of Hydrology*, *547*, 168–183. https://doi.org/10.1016/j.jhydrol.2017.01.052

Wells, C. M., & Price, J. S. (2015). A hydrologic assessment of a saline-spring fen in the Athabasca oil sands region, Alberta, Canada - a potential analogue for oil sands reclamation. *Hydrological Processes*, *29*(20), 4533–4548.

https://doi.org/10.1002/hyp.10518

Whittington, P. N., & Price, J. S. (2006). The effects of water table draw-down (as a surrogate for climate change) on the hydrology of a fen peatland, Canada. *Hydrological Processes*, *2274*(November 2008), 2267–2274. https://doi.org/10.1002/hyp

Wieder, R. K., & Vitt, D. H. (2006). Boreal Peatland Ecosystems. In R. K. Wieder & D. H. Vitt (Eds.), *Ecological Studies* (Vol. 188). Springer. https://doi.org/10.1017/CBO9781107415324.004

Winkler, R. D., & Moore, R. D. (2007). Variability in snow accumulation patterns within forest stands on the interior plateau of British Columbia, Canada. *Hydrological Processes*, *2309*, 2300–2309. https://doi.org/10.1002/hyp

Woo, M. K., Arain, M. A., Mollinga, M., & Yi, S. (2004). A two-directional freeze and thaw algorithm for hydrologic and land surface modelling. *Geophysical Research Letters*, *31*(12), 1–4. https://doi.org/10.1029/2004GL019475

Woo, M. K., & Steer, P. (1986). Monte Carlo Simulation of Snow Depth in a Forest. *Water Resources Research*, *22*(6), 864–868.

Woo, Ming-ko. (1982). Upward Flux of Vapor From Frozen Materials in the High Arcitc. *Cold Regions Science and Tecnology*, *5*, 269–274.

Woo, Ming-ko. (2012). Permafrost Hydrology. In *Springer* (Vol. 53, Issue 9). Springer. https://doi.org/10.1007/978-3-642-23462-0

Woo, Ming-ko, & Xia, Z. (1996). Effects of Hydrology on the Thermal Conditions of the Active Layer. *Nordic Hydrology*, *27*, 129–142. https://doi.org/10.2166/nh.1996.009

Woo, Ming Ko, & Winter, T. C. (1993). The role of permafrost and seasonal frost in the hydrology of northern wetlands in North America. *Journal of Hydrology*, *141*(1–4), 5–31. https://doi.org/10.1016/0022-1694(93)90043-9

Woo, Mink-ko, & Heron, R. (1981). Occurence of Ice Layers at the Base of High Arctic Snowpacks. *Arctic and Alpine Research*, *13*(2), 225–230.

Wright, N., Hayashi, M., & Quinton, W. L. (2009). Spatial and temporal variations in active layer thawing and their implication on runoff generation in peat-covered permafrost terrain. *Water Resources Research*, *45*(5), 1–13. https://doi.org/10.1029/2008WR006880

Wu, Y., Verseghy, D. L., & Melton, J. R. (2016). Integrating peatlands into the coupled Canadian Land Surface Scheme (CLASS) v3.6 and the Canadian Terrestrial Ecosystem Model (CTEM) v2.0. *Geoscientific Model Development*, *9*(8), 2639–2663. https://doi.org/10.5194/gmd-9-2639-2016

Xie, C., & Gough, W. A. (2013). A simple thaw-freeze algorithm for a multi-layered soil using the stefan equation. *Permafrost and Periglacial Processes*, *24*(3), 252–260. https://doi.org/10.1002/ppp.1770

Xu, J., Morris, P. J., Liu, J., & Holden, J. (2018). *Catena PEATMAP : Refining estimates of global peatland distribution based on a meta-analysis*. *160*(September 2017), 134–140. https://doi.org/10.1016/j.catena.2017.09.010

Young-Robertson, J. M., Ogle, K., & Welker, J. M. (2017). Thawing seasonal ground ice: An important water source for boreal forest plants in Interior Alaska. *Ecohydrology*, *10*(3), 1–16. https://doi.org/10.1002/eco.1796

Zhang, T. (2005). Influence of seasonal snow cover on the ground thermal regime: an overview. *Reviews in Geophysics*, *43*(2004). https://doi.org/10.1029/2004RG000157.1.INTRODUCTION

Zhang, X., Flato, G., Kirchmeier-Young, M., Vincent, L., Wan, H., Wang, X., Rong, R., Fyfe, J.,

Li, G., & Kharin, V. . (2019). Temperature and Precipitation Across Canada. In E. Bush & D. . Lemmen (Eds.), *Canada's Changing Climate Report* (pp. 112–193). Government of Canada.

Zhang, Y., Carey, S. K., & Quinton, W. L. (2008). Evaluation of the algorithms and parameterizations for ground thawing and freezing simulation in permafrost regions. *Journal of Geophysical Research Atmospheres*, *113*(17), D17116. https://doi.org/10.1029/2007JD009343

Zhao, L., & Gray, D. M. (1997). A parametric expression for estimating infiltration into frozen soils. *Hydrological Processes*, *11*(13), 1761–1775. https://doi.org/10.1002/(SICI)1099-1085(19971030)11:13<1761::AID-HYP604>3.0.CO;2-O

Zoltai, S. . C. ., & Vitt, D. . H. . (1995). Environmental Gradients and Classification. *Canadian Wetlands*, *118*(1), 131–137.
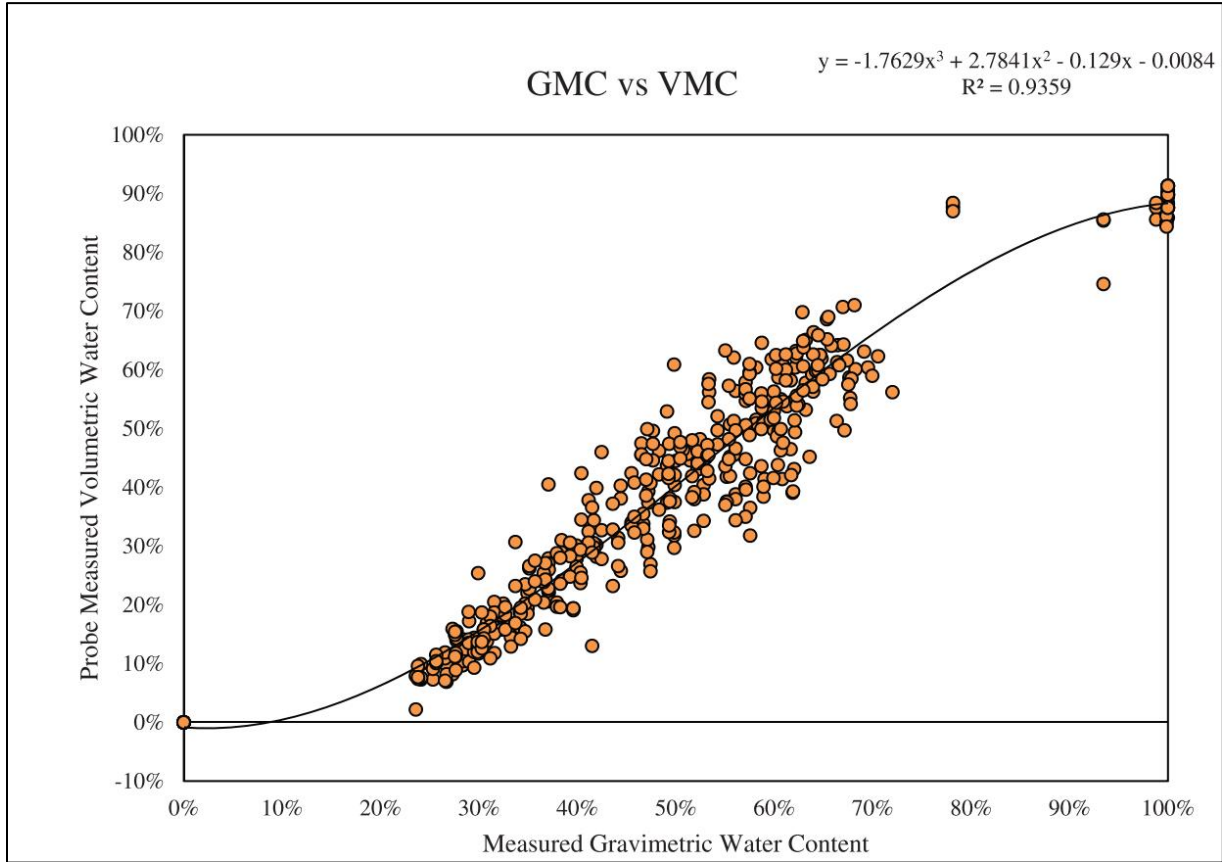
Appendices

Appendix A

Figure A-1 Calibration curve for WET-2 sensor calibration. The curve is a 3rd order polynomial. Gravimetric water content vs volumetric water content. Uncorrected values <10% would be below 0% when corrected and so were automatically set to 0%.

Table A-1 Diffuse proportion and transmissivity values used for the incoming shortwave radiation tool in ArcMap 10.1. Note: Transmissivity values were determined using suggestions from the manual, and then adjusted to see which provided the best estimate of incoming shortwave radiation as measured at the met station. The diffuse proportion is simply the inverse of the transmissivity value.

| Date	Diffuse Proportion	Transmissivity	Sky Conditions	ArcInput
01-May-17	0.3	0.7	Generally Clear	UNIFORM SKY
02-May-17	0.8	0.2	Cloudy	STANDARD OVERCAST SKY
03-May-17	0.8	0.2	Cloudy	STANDARD OVERCAST SKY
04-May-17	0.2	0.8	Clear	UNIFORM SKY
05-May-17	0.3	0.7	Generally Clear	UNIFORM SKY
06-May-17	0.2	0.8	Clear	UNIFORM SKY
07-May-17	0.8	0.2	Cloudy	STANDARD OVERCAST SKY
08-May-17	0.3	0.7	Generally Clear	UNIFORM SKY
09-May-17	0.8	0.2	Cloudy	STANDARD OVERCAST SKY
10-May-17	0.2	0.8	Clear	UNIFORM SKY
11-May-17	0.2	0.8	Clear	UNIFORM SKY
12-May-17	0.8	0.2	Cloudy	STANDARD OVERCAST SKY
13-May-17	0.8	0.2	Cloudy	STANDARD OVERCAST SKY
14-May-17	0.8	0.2	Cloudy	STANDARD OVERCAST SKY
15-May-17	0.8	0.2	Cloudy	STANDARD OVERCAST SKY
16-May-17	0.8	0.2	Cloudy	STANDARD OVERCAST SKY
17-May-17	0.3	0.7	Cloudy	UNIFORM SKY
18-May-17	0.3	0.7	Generally Clear	UNIFORM SKY
19-May-17	0.3	0.7	Generally Clear	UNIFORM SKY
20-May-17	0.3	0.7	Generally Clear	UNIFORM SKY
21-May-17	0.2	0.8	Clear	UNIFORM SKY
22-May-17	0.8	0.2	Cloudy	STANDARD OVERCAST SKY
23-May-17	0.3	0.7	Generally Clear	UNIFORM SKY
24-May-17	0.8	0.2	Cloudy	STANDARD OVERCAST SKY
25-May-17	0.2	0.8	Generally Clear	UNIFORM SKY
26-May-17	0.2	0.8	Generally Clear	UNIFORM SKY
27-May-17	0.2	0.8	Generally Clear	UNIFORM SKY
28-May-17	0.2	0.8	Generally Clear	UNIFORM SKY
29-May-17	0.2	0.8	Generally Clear	UNIFORM SKY
30-May-17	0.2	0.8	Generally Clear	UNIFORM SKY
31-May-17	0.2	0.8	Clear	UNIFORM SKY
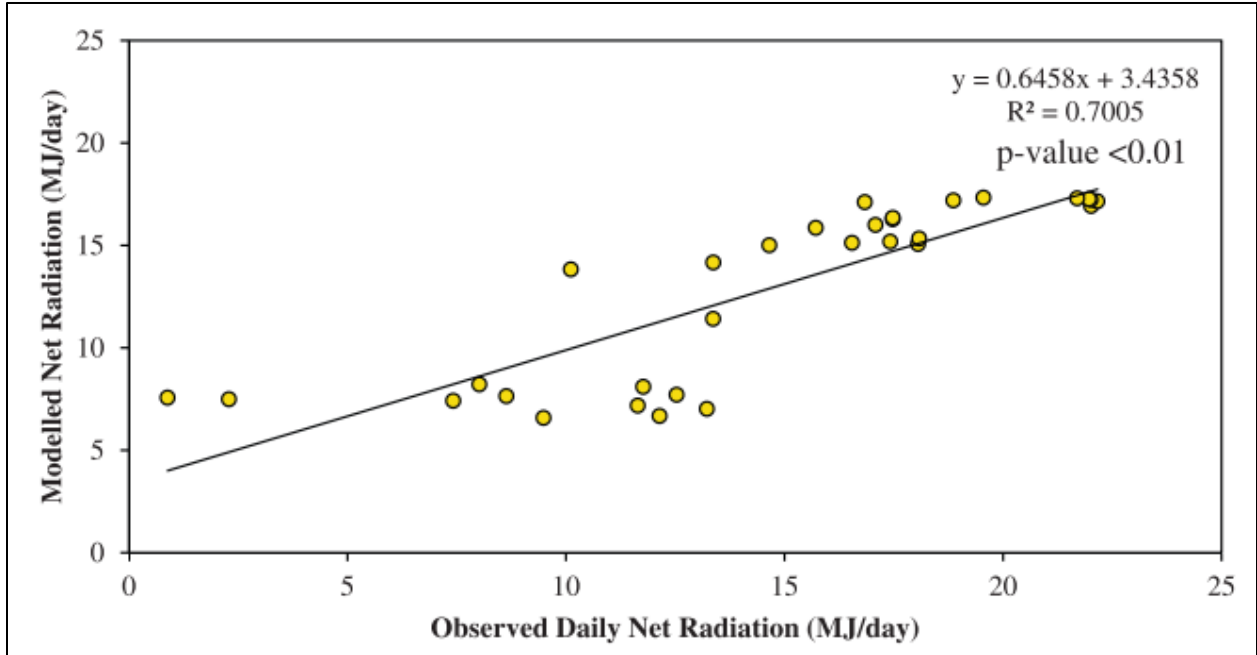
Figure A-2 Observed Cumulative net radiation vs. modelled net radiation. The daily sum is based off of positive half-hour values only. pvalue indicates a significant relationship.
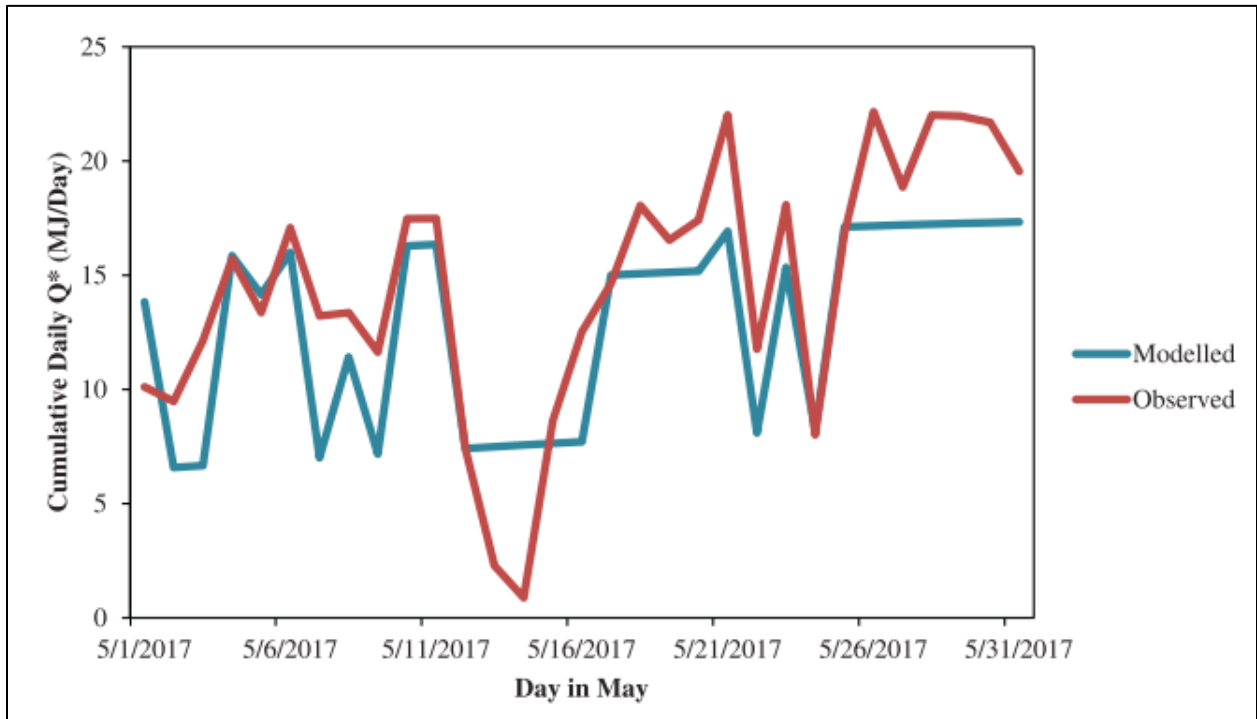

Figure A-3 Observed daily Q* vs modelled Q* for the month of May 2017. The daily sum is based off of positive half-hour values only.

Table A-2 Results from the Global Moran's I. Note: The distance column refers to the maximum distance where spatial autocorrelation was considered to be the strongest. The Morans Index indicates whether the data are clustered, dispersed or random. The expected index is what the value would be if the data were randomly distributed. Variance expla- nation. The Z-score and p value indicate whether the pattern that is evident is statistically significant.

Variable	Distance (m)	Moran's index	Expected index	Variance	Z-Score	p-value
2017 Ice Thickness	30	0.01564	-0.00418	0.000137	1.694254	0.090217
2017 Avg Melt Rate	60	0.018223	-0.00503	0.000035	3.925058	0.000087
2018 Avg Melt Rate SBS3	3.25	0.004612	-0.02564	0.000155	2.432895	0.014979
2018 Avg Melt Rate SBS1	3.25	0.011338	-0.02778	0.000221	2.633148	0.00846
2018 Avg Melt Rate NBS1	1	0.362593	-0.02778	0.008342	4.274119	0.000019
2018 Avg Melt Rate NBS2	1.25	0.140595	-0.02778	0.006139	2.149005	0.031634
2018 Ice Thickness SBS1	1.75	0.140154	-0.02941	0.001894	3.895903	0.000098
2018 Ice Thickness SBS3	1.25	0.385086	-0.02632	0.004474	6.160345	0

Table A-3 Summary statistics for small-scale ice thickness and Avg melt rate around each tree used in the 2018 ice survey.

Tree	Ice Thickness				
	Avg (cm)	Median (cm)	SD(cm)	Max (cm)	Min (cm)
NBS1	8.8	8.0	5.2	23.5	0
NBS2	9.8	8.5	6.7	28.9	0
SBS1	8.2	7.5	6.2	35	0
SBS2	7.6	6.6	5.5	28	1
SBS3	15	12.5	11.1	38	0
Tree	Melt Rate				
	Avg (cm/day)	Median (cm/day)	SD(cm/day)	Max (cm/day)	Min (cm/day)
NBS1	0.9	0.9	0.6	3.2	0
NBS2	1.2	1.0	0.7	4.0	0
SBS1	1.1	0.8	0.8	3.3	0
SBS2	0.8	0.7	0.5	3.1	0.2
SBS3	1.2	1.1	0.8	5.2	0

Table A-4 Ice thickness as determined by the mid fen thermocouple profile the day before spring ice melt occurred.

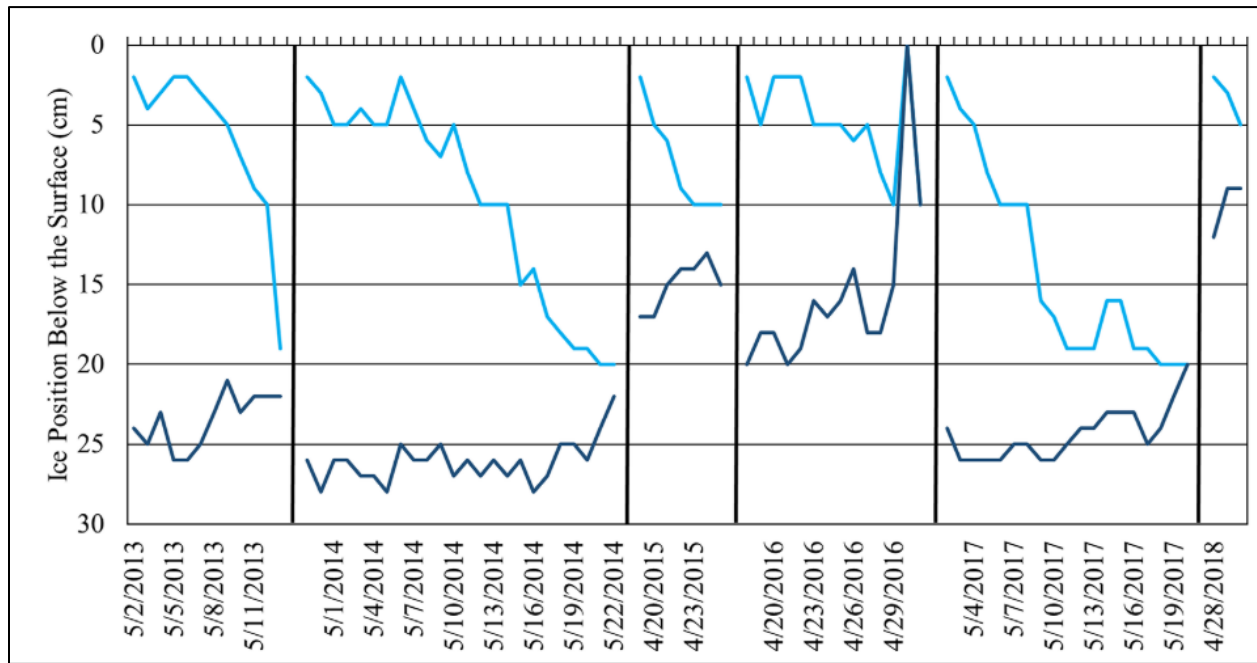| Year	Ice Thickness (cm)
2013	26
2014	25
2015	15
2016	19
2017	24
2018	12

Figure A-4 Bi-directional melt for seasonal ground ice at the Pauciflora fen. Over the six spring melt seasons, 72% (±13%) of the ice was melted from above, and 28% (±13%) from below. The upper line (light blue) represents the upper ice position of the seasonal ground ice. The lower line (dark blue) represents the lower position of the seasonal ground ice.

Appendix B

Method for estimating ground surface temperature under future climate change scenarios

The climate change projections for monthly mean air temperature were referenced from Figure 3a in Thompson et al., 2017. In this paper, the authors conducted a climate change analysis for the Utikima Research Study Area (URSA), located approximately 266 km WSW of Pauciflora, using thirteen climate change scenarios. These scenarios were chosen because they bookended the expected range in variability of future climate projections. For our study, the climate projections were averaged for each month and are shown below.
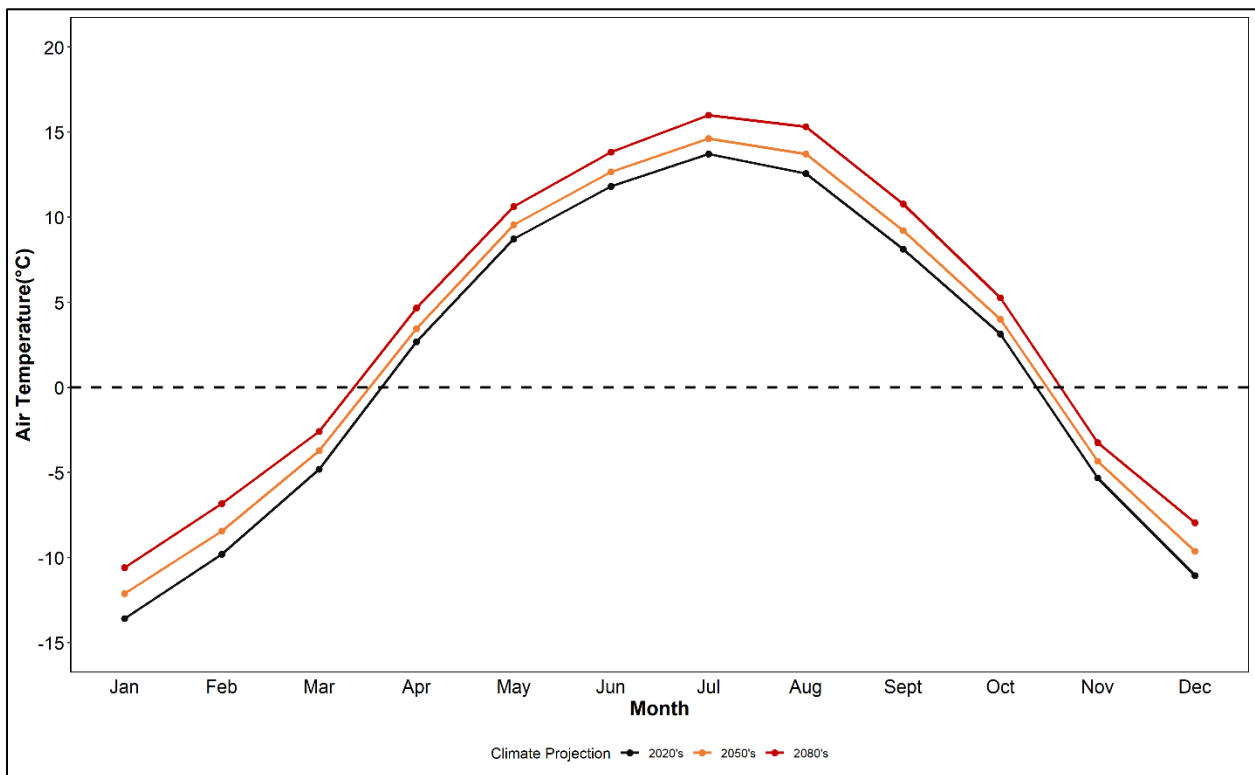

Figure B-1 Average Climate Change Projections for Air Temperature, based on Thompson et al., 2017.

A regression was built between air temperature measured at 2 m above the ground surface and the temperature measured by the 2 cm below ground surface thermocouple. The data and regression is shown below in Figure B-2.
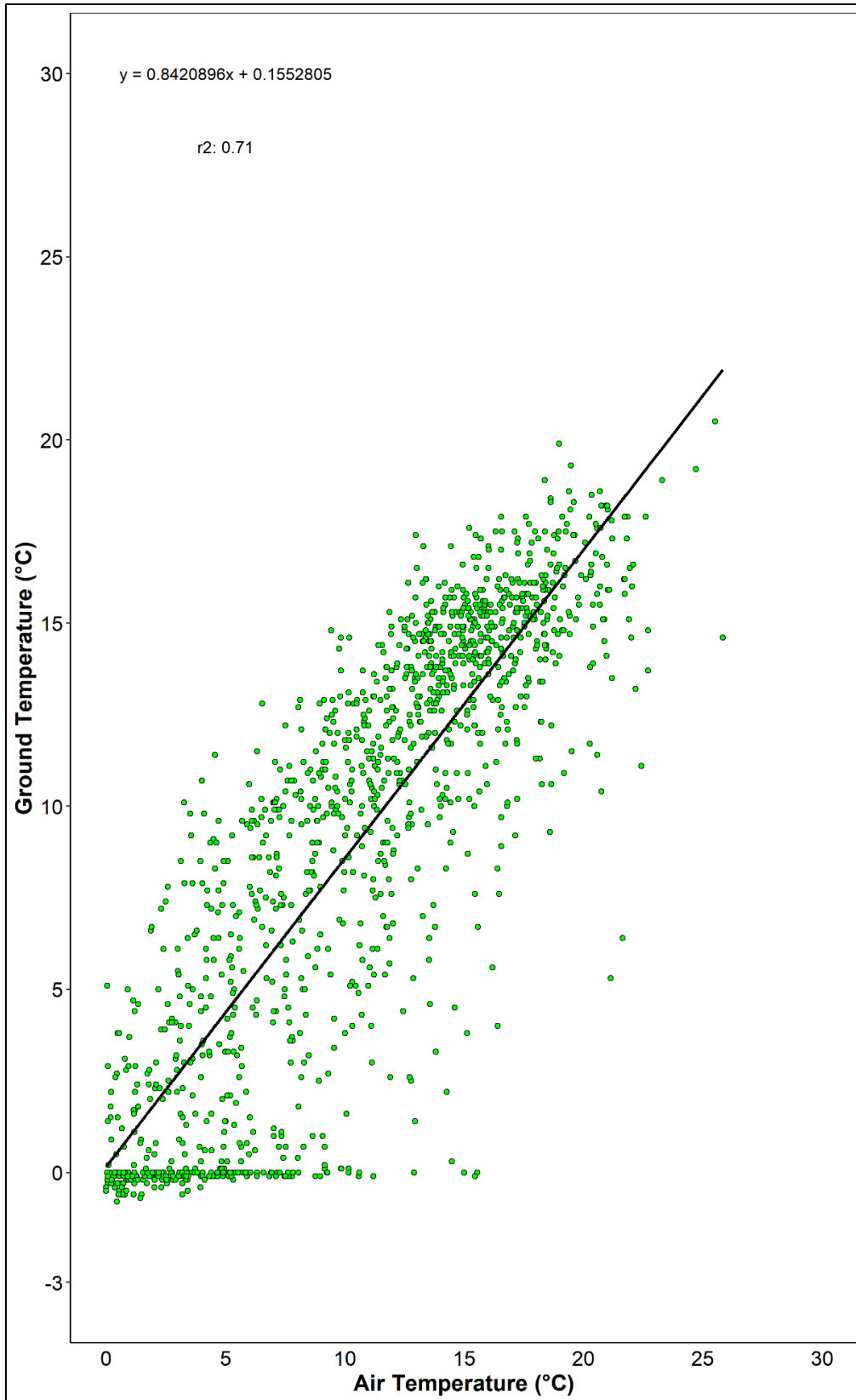
Figure B-2 Regression Equation used to convert air temperature to ground temperature.

The regression was only used for when air temperatures were > 0°C, as the development of a snowpack decoupled the ground temperature from the air temperature. Mean monthly projected ground temperatures were calculated using the mean monthly projected air temperatures (Figure B-1) and the mean monthly ground surface temperature from each sensitivity run using ground surface temperature. The results are shown below in Figure (B-3). The winter months (January-March, November, December) have a high degree of uncertainty.
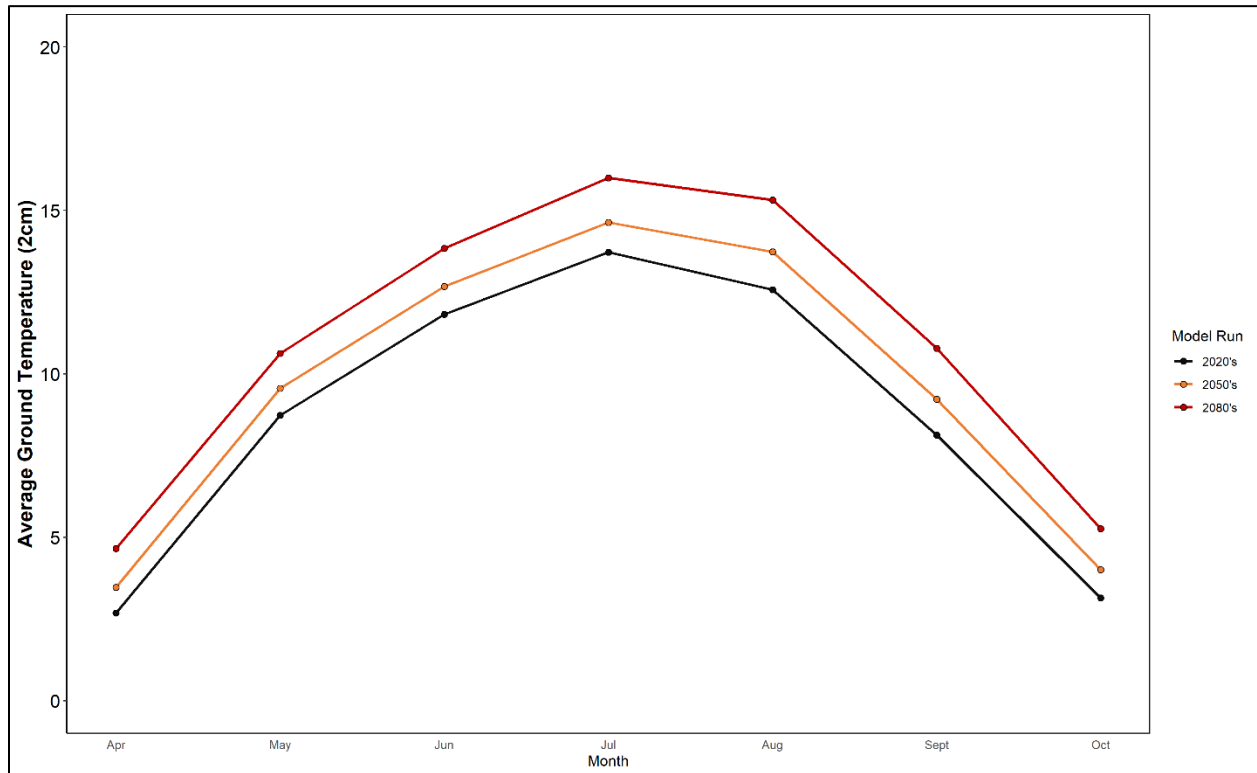

Figure B-3 Modelled Projected Mean Monthly Ground Temperature.
Table B-1 Results from the multiple linear regression showing that all three parameters were found to be statistically significant.

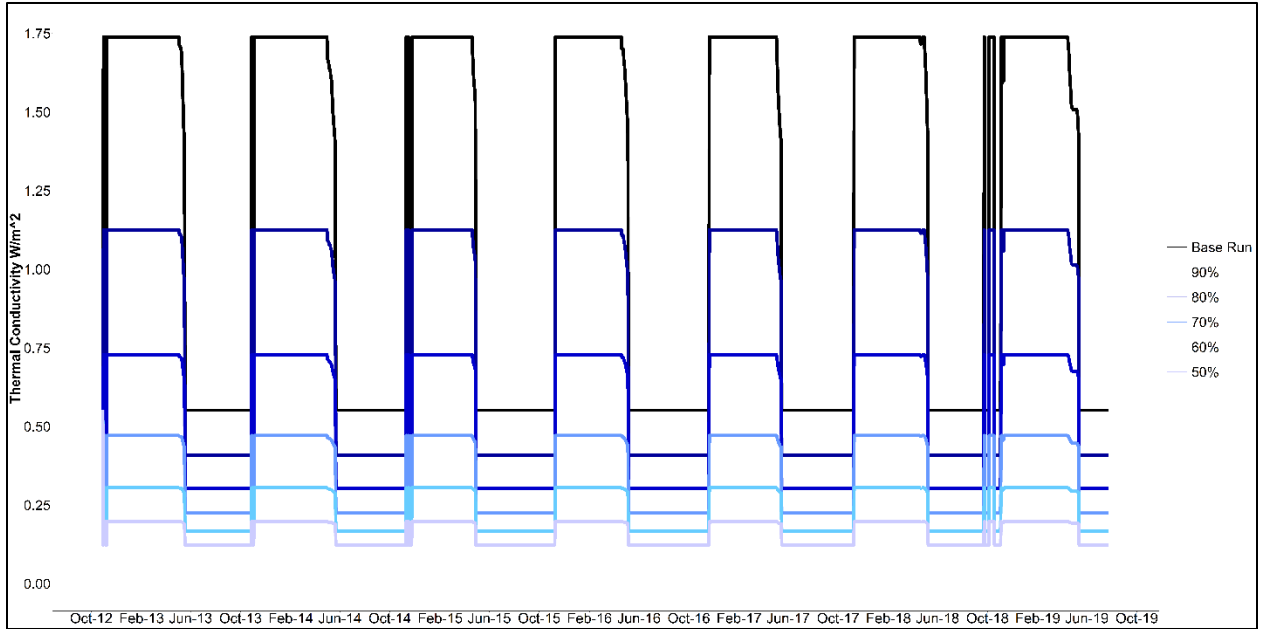| Coefficients	Estimate	Standard Error	T value	p-value
Intercept	-0.34284	0.10477	-3.272	0.00139
Δ Ground Surface Temperature	-0.11200	0.01981	-5.654	1.05×10^{-07}
VMC	0.39608	0.02942	13.465	$<2 \times 10^{-16}$
Porosity	0.23399	0.09903	2.363	0.01972
r^2	0.6075	Adjusted r^2	0.5979	
F-Statistic	62.94 on 3 and 122 Degrees of Freedom	p-value	$<2.2 \times 10^{-16}$	

Figure B-4 Thermal Conductivity with changing VMC. (Time series is from October 29, 2012-September 26, 2019.
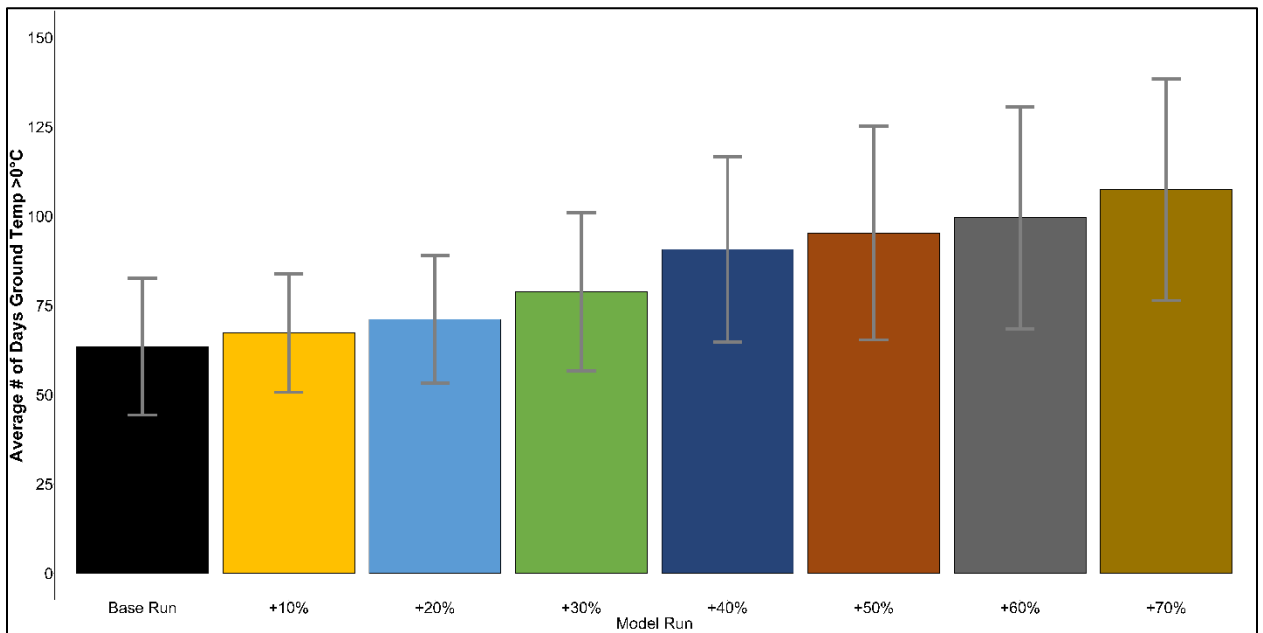

Figure B-5 Average Number of days where the daily average ground temperature is above 0°C for each climate run.
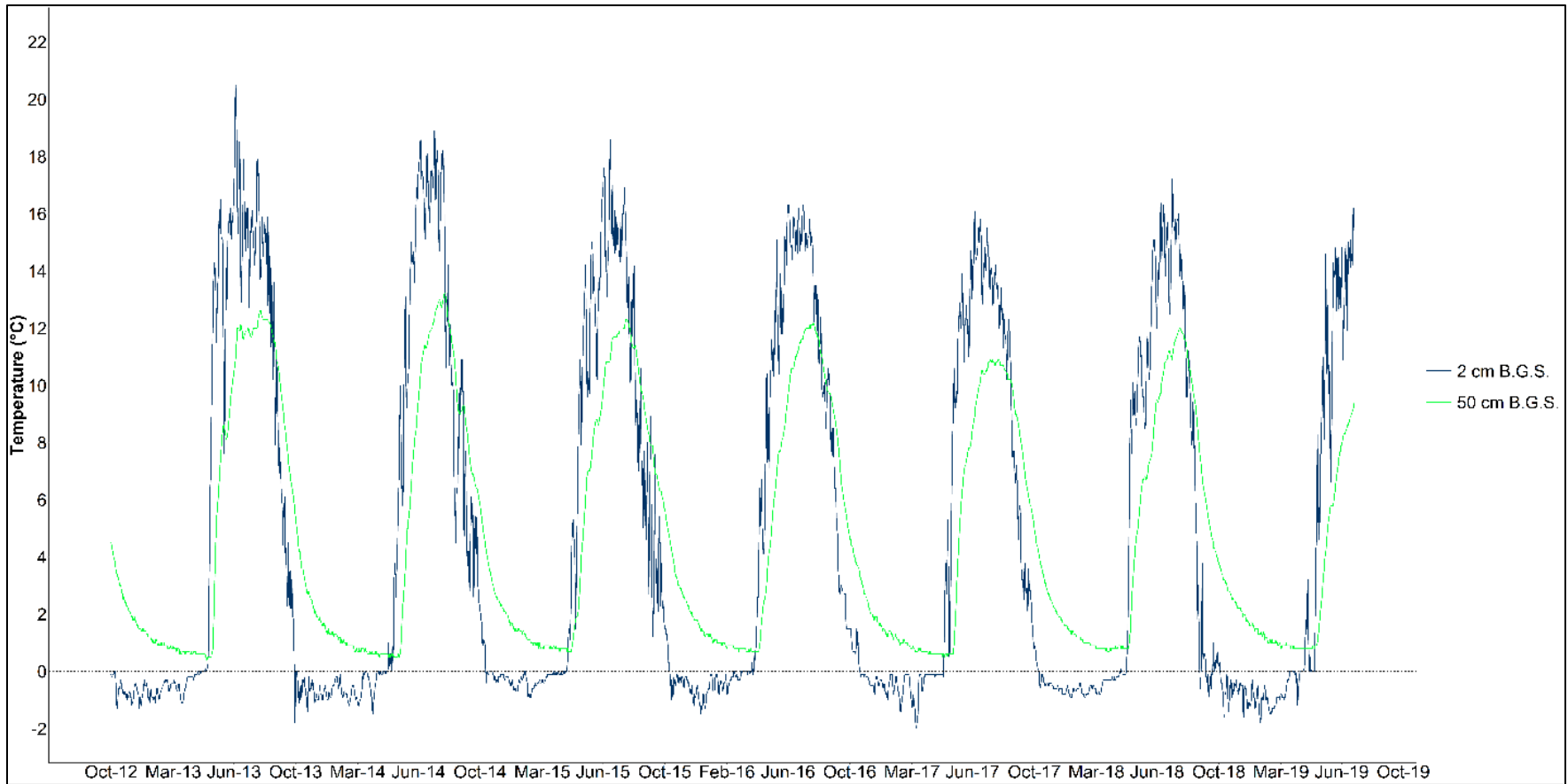
Figure B-6 Observed Ground temperatures measured at 2 and 50 cm below the ground surface (B.G.S.). These were used to drive the Stefans equation from the surface (2 cm) and from below (50 cm). (Time series is from October 29, 2012-September 26, 2019).

Appendix C

Calculation of unsaturated hydraulic conductivity (K_{unsat})

In order to calculate Kunsat, the water table first needed to be determined, however CRHM does not calculate a water table position, it calculates water as an equivalent depth. First, using the physical properties of the peat soil at Pauciflora (Table C-1), water table position, and soil retention data from Goetz & Price, (2015), the amount of water in equivalent depth was determined for each peat soil layer.

Table C-1 Physical Properties used to determine the maximum amount of water that could be held in each layer.

Depths (cm)	Maximum Equivalent Depth when Saturated (mm)	Average Porosity
0-5	49.2	0.984
5-10	48.8	0.975
10-15	47.8	0.957
15-20	47.0	0.939
20-25	47.4	0.948
25-30	47.4	0.948
30-35	47.4	0.948
35-40	47.4	0.948
40-45	46.7	0.913
45-50	46.7	0.913
50-60	91.3	0.913
60-360	2400	0.8

The equivalent depth was then calculated for each soil layer, based on the position of the water table, and the soil retention characteristics for each soil layer, using the equation below;

$$Equivalent\ Depth\ (mm) = \theta_r + \frac{(\theta_s - \theta_r)}{\left(1 + \left[n \times \frac{(WTP - 1)}{100}\right]^n\right)^{\left(1 - \left(\frac{1}{n}\right)\right)}}$$

(C-1)

Where θ_r and θ_s are the residual and saturated volumetric moisture contents, n a dimensionless VGM parameter, and WTP is the water table position (cm below peat surface). A relationship was developed between Equivalent depth and the observed water table position as shown below in Figure C-1.
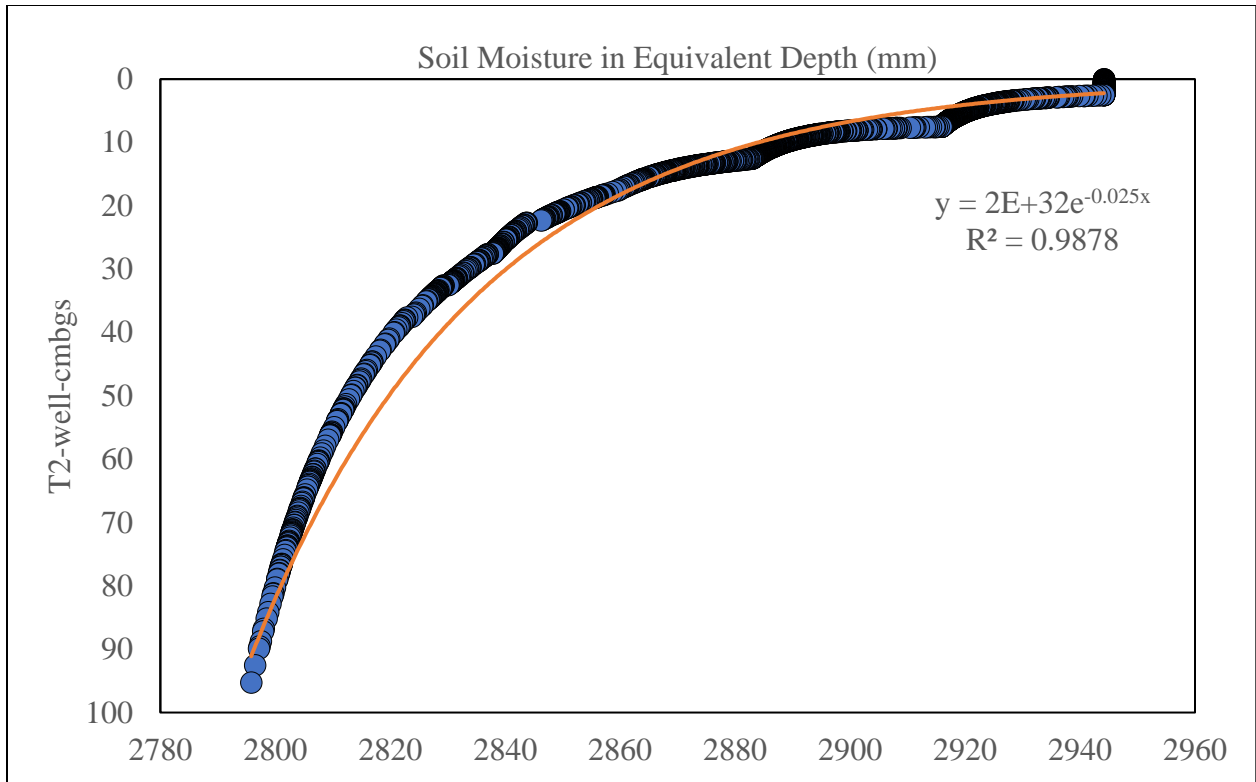
Figure C-1 The empirical relationship between observed water table position and equivalent depth. The displayed equation has been implemented into CRHM to provide a water table position variable.

The resulting equation was then implemented into CRHM to calculate a water table position value based on the modelled equivalent depth. For each timestep, this WTP was used to then calculate the unsaturated hydraulic conductivity for the 0-1 cm layer, based on optimized VGM parameters listed below in Table C-2. Optimization was completed using the online calculator https://seki.webmasters.gr.jp/swrc/.

Table C-2 VGM parameters, optimized using retention data from Goetz & Price (2014) and the website https://seki.webmasters.gr.jp/swrc/'

Parameters	Value
A (meters)	357.06
n	1.3
θr	4×10^{-6}
θ_s	0.9835
$K_{sat \, (m/sec)}$	2.94×10^{-6}
SE	$(VMC - \theta_r)/(\theta_s - \theta_r)$
τ	-5

These same parameters could then be used to determine the K_{unsat} using the following equation;

128

$$K_{unsat} = K_{sat} \times (SE^{\tau}) \times \left(1 - \left(1 - SE^{\left(\frac{1}{(1-(\frac{1}{n}))}\right)}\right)^{\left(1-\left(\frac{1}{n}\right)\right)^{2}}\right)$$

(C-2)

where τ is the tortuosity factor, and *SE* is the effective saturation. For each timestep, K_{unsat} was calculated and then divided by the K_{sat} to determine the Kratio used in the resistance scheme.
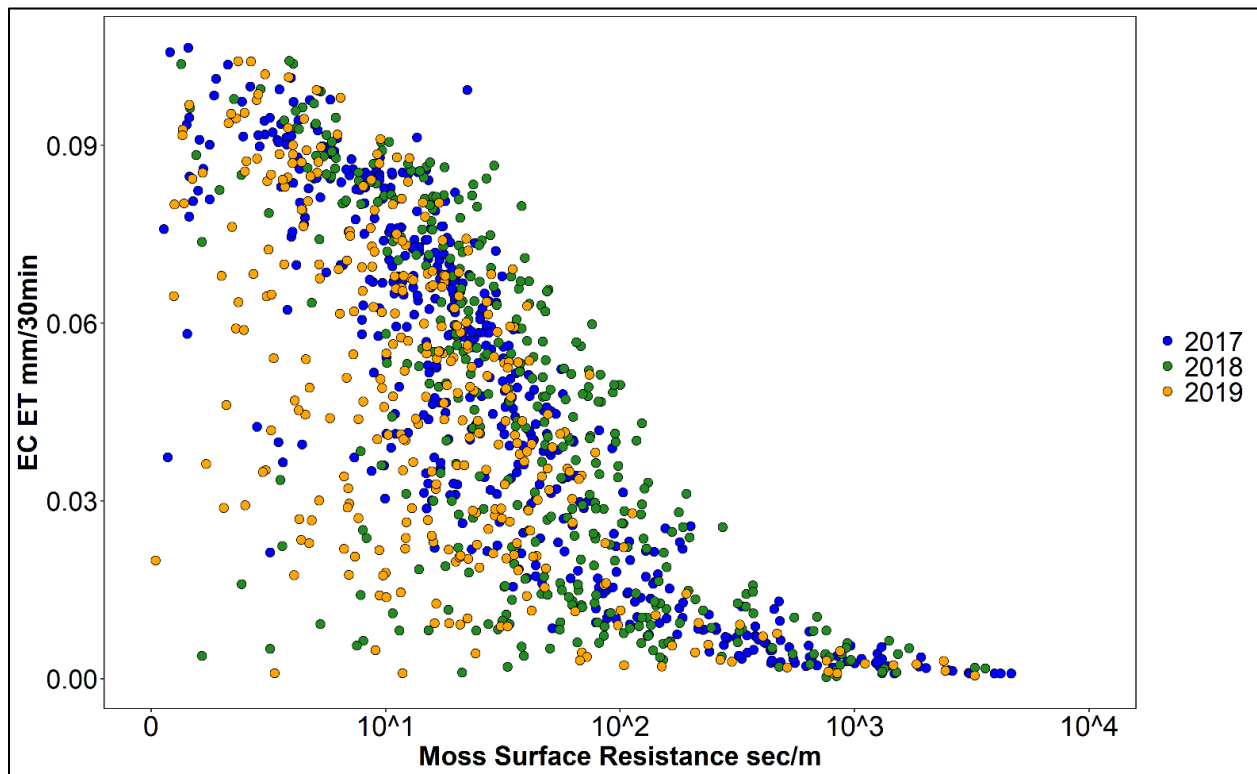
Resistance Scheme Figures

Figure C-2 Observed Peat Resistance vs EC AET. Resistance values have been filtered to exclude values when alpha>1, saturated conditions, rain present, negative energy inputs, & nighttime values. The x-axis has been log transformed, where 10^2 represents 100, 10^3 represents 1000.

Figure C-2 shows that most resistance values coincide with the full range of EC ET values, despite being in the 100's of sec/m. This is contrasted by the modelled results, where declines begin as low as resistance values of 40 sec/m.

Calculation of HRU ground water inputs

To calculate the ground water inputs into and out of the HRU, two additional monitoring wells, one up gradient and one down gradient (Figure 5-1c) were used to build a regression with main monitoring well within the HRU. These are shown below in Figure C-3.
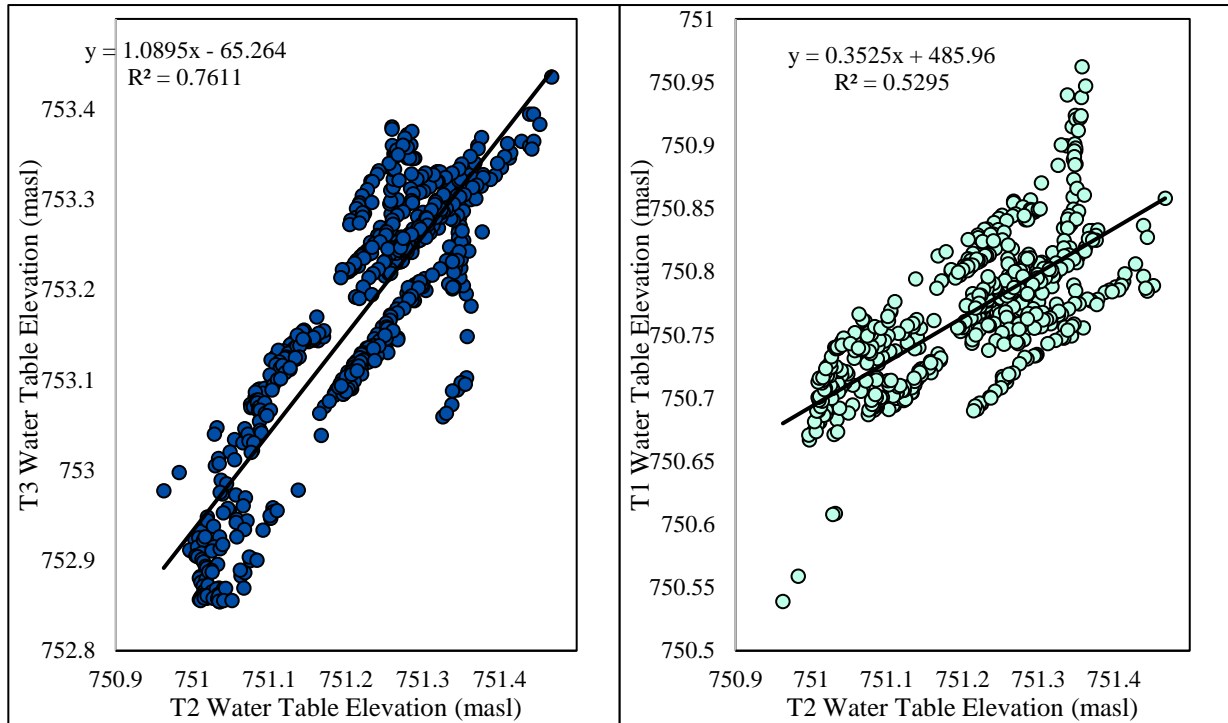

Figure C-3 Regression equations between the T2 Monitoring well in the HRU, and the upgradient (T3) and down gradient (T1) well. Each equation was used in CRHM to determine the absolute water table position up gradient and down gradient, to calculate the hydrological gradient.

Each regression equation was inputted into CRHM, then using the CRHM modelled water table position, the water table position (masl) was calculated for T1 and T3. The hydrological gradient was then calculated using equation C-3.

$$\Delta_{x-T2} = \frac{(zT_x - zT_2)}{\Delta Horizontal\ Distance}$$

(C-3)

where $\Delta_{x\text{-}T2}$ is the hydrological gradient, the subscript *x* denotes the well the gradient is being calculated for (T1 or T3), zT_x is the elevation (masl) of the water table for the monitoring well being used, zT_2 is the elevation (masl) of the monitoring well within the HRU, and ΔHorizontal Distance (m) is the straight-line distance between T2 well and the other monitoring well. Once the

gradient was calculated, Darcy's Law was used to calculate the input and output of ground water for each timestep.

$$q_x = \frac{Q_x}{A_x} = -K_{sat} \times \Delta_{x-T2}$$

where q_x is the specific discharge, which is equal to the volume rate of flow, Q_x divided by the cross sectional area of the flow face (m^2), and K_{sat} is the saturated hydraulic conductivity. K_{sat} used for this calculation differs for what was used when determining K_{unsat} as that only represented the top 5 cm. A new Ksat value was calculated by taking the geomean of the field K_{sat} reported by Wells et al., (2017), combined with laboratory measurements measured in the lab using the constant head method for determining K_{sat} (Taylor & Price, 2015). By rearranging and solving for Q_x then dividing by the HRU area, the input(output) was calculated and added(subtracted) from the HRU.